INFORMATION TO USERS

This manuscript has been reproduced from the microfilm master. UMI films the text directly from the original or copy submitted. Thus, some thesis and dissertation copies are in typewriter face, while others may be from any type of computer printer.

The quality of this reproduction is dependent upon the quality of the copy submitted. Broken or indistinct print, colored or poor quality illustrations and photographs, print bleedthrough, substandard margins, and improper alignment can adversely affect reproduction.

In the unlikely event that the author did not send UMI a complete manuscript and there are missing pages, these will be noted. Also, if unauthorized copyright material had to be removed, a note will indicate the deletion.

Oversize materials (e.g., maps, drawings, charts) are reproduced by sectioning the original, beginning at the upper left-hand corner and continuing from left to right in equal sections with small overlaps. Each original is also photographed in one exposure and is included in reduced form at the back of the book.

Photographs included in the original manuscript have been reproduced xerographically in this copy. Higher quality 6" x 9" black and white photographic prints are available for any photographs or illustrations appearing in this copy for an additional charge. Contact UMI directly to order.

UMI

A Bell & Howell Information Company
300 North Zeeb Road, Ann Arbor MI 48106-1346 USA
313/761-4700 800/521-0600

Numerical and Experimental Investigation of Heat Transfer and Pollutant Formation in Porous Direct-Fired Radiant Burners

by

Marc David Rumminger

B.S. (University of Illinois at Urbana-Champaign) 1991
M.S. (University of California, Berkeley) 1994

A dissertation submitted in partial satisfaction of the

requirements for the degree of

Doctor of Philosophy

in

Engineering - Mechanical Engineering

in the

GRADUATE DIVISION

of the

UNIVERSITY OF CALIFORNIA, BERKELEY

Committee in charge:

Professor Robert W. Dibble, Chair
Professor Jyh-Yuan Chen
Professor Robert A. Harley

1996

The dissertation of Marc David Rumminger is approved:

Robert W. Dibble 14 Nov 1996

Chair Date

[signature] 18 NO. 1996

Date

Robert Harley 18 Nov. 1996

Date

University of California, Berkeley

1996

Numerical and Experimental Investigation of Heat Transfer and Pollutant Formation in Porous Direct-Fired Radiant Burners

by

Marc David Rumminger

Contents

List of Figures

List of Tables

List of Symbols

Typical units are given in parentheses

Roman Symbols

A	Area (m^2)
b	Backward scattering fraction
$c_{p,k}$	Specific heat of k-th species (J/g-K)
d	Pore diameter (cm)
D	Tube diameter (mm)
E_i	Emissive power of object i (kW/m^2)
$EINO_x$	Emission index for nitrogen oxides (g-NO_x / kg-CH_4)
F_{ij}	Radiation view factor between object i and object j
f	Forward scattering fraction
f_h	Adjustment factor for convective heat transfer coefficient
h_k	Enthalpy of k-th species (J/g)
h_v	Volumetric convective heat transfer coefficient (W/m^3-K)
h_o	Convective heat transfer coefficient based on area (W/m^2-K)
J	Radiosity (kW/m^2)
$k_{g,e}$	Effective thermal conductivity of gas (W/m-K)
$k_{s,e}$	Effective thermal conductivity of porous solid (W/m-K)
k_s	Bulk solid thermal conductivity (W/m-K)
kk	Total number of gas-phase species
L	Length of porous medium (cm)
L	Characteristic length for convection for row of tubes = $D\pi/2$ (cm)
M_i	Molecular mass of i-th species (g/mol)
$\dot{m}''$	Mass flow rate per unit area (g/cm^2-s)
Nu	Nusselt number (volumetric = $h_v d^2/k_g$, area-based = $h\,d\,/\,k_g$)
Nu_L	Nusselt number for a row of tubes = $h\,L/k_g$
$Nu_{L,lam}$	Laminar Nusselt number for a row of tubes
$Nu_{L,turb}$	Turbulent Nusselt number for a row of tubes
Pr	Prandtl number ($\nu/\alpha = \mu\,c_p\,/\,k_g$)
q	Firing rate (kW/m^2)
$\dot{q}$	Chemical heat release (W/cm^3)
q^r	net radiant flux = q^+-q^- (W/m^2)
q^+	Forward radiation (W/m^2)
q^-	Backward radiation (W/m^2)
Q_+	Radiant flux from $+\infty$ (W/m^2)
Q_-	Radiant flux from $-\infty$ (W/m^2)

R_{ij} Radiative resistance between object i and object j (m^{-2})
R_i Radiative resistance of surface i (m^{-2})
Re Pore Reynolds number, $\dot{m}''d/\mu$
$Re_{\psi,L}$ Reynolds number for convection coefficient correlation for a single row of tubes, $\dot{m}''L/\psi\mu$
s Spacing between tube centerlines (mm)
T_g Gas temperature (K)
T_s Solid temperature (K)
u Gas velocity (cm/s)
V_k Diffusive velocity of the k-th species (cm/s)
W_k Molecular weight of k-th species (g/mol)
x Axial distance (cm)
x_s distance between downstream edge of burner and screen (cm)
x_{in} x value of inlet to computational domain (cm)
x_{out} x value of outlet from domain (cm)
[X] Molar concentration of species X (mol/cm^3)
X_k Mole fraction of k-th species
Y_k Mass fraction of k-th species

Greek Symbols

ε Emissivity
σ Stefan-Boltzmann constant ($5.67\ 10^{-8}\ W/m^2$)
σ_ε Extinction coefficient (m^{-1})
ε Porosity
ρ Density of gas (g/cm^3)
ρ_o Reflectivity (average) of porous medium
ω_o Single scattering albedo
$\dot{\omega}_k$ Reaction rate for k-th species (mol/cm^3-s)
ϕ Equivalence ratio
ψ Scaling factor for Nusselt number for a row of cylinders
α_{ki} Third-body efficiency of the k-th species in the i-th reaction
ν_{ki}'' coefficient for the k-th species in the i-th reaction of the products
ν_{ki}' coefficient for the k-th species in the i-th reaction of the reactants

Important conversions

$$\%\ \text{Excess Air} = \frac{1-\phi}{\phi} \cdot 100\%$$

$$\phi = \frac{1}{(\%\text{Excess Air}/100\%)+1}$$

100,000 Btu/hr-ft^2 = 315 kW/m^2

Acknowledgements

Many people have given me valuable assistance during my years at Berkeley. I thank my research advisor, Professor Dibble, for his guidance and encouragement. He gave me the freedom to follow my own path, but always kept me heading in the right direction. I also thank the other members of my dissertation committee, Professor Chen and Professor Harley.

For financial support, I am grateful to the Basic Research Group of the Gas Research Institute and the contract monitor Dr. Kevin Krist, whose probing questions always kept me thinking. Also associated with the project was Shyam Singh of SSEEI, Inc. who always reminded me about the operation of *real* burners in industrial settings. His practical knowledge was a great benefit to my research. The researchers from Purdue University that were part of the radiant burner project were extremely helpful to my modeling effort, especially Professor Raymond Viskanta, Professor Jayavant Gore and Rahul Mital.

My co-workers in Professor Dibble's laboratory have been crucial to my completion of this dissertation, but are too numerous to mention. I thank the Hesse Hall shop for help with burner construction, the Etcheverry Hall High-Performance Computing Facility and the Combustion Laboratory administrator MaryAnne Peters for keeping the laboratory running smoothly.

In my second year at Berkeley, I spent a summer working with Dr. Andrew Lutz at Sandia National Laboratory in Livermore, CA. I thank Dr. Lutz for acting as one of my mentors; he taught me a great deal about numerical modeling, technical writing and technical presentations.

The LIF and thermocouple experiments described in Chapter 6 were performed in the Molecular Physics Laboratory at SRI International in Menlo Park, CA. I thank Dr. Norbert Heberle for teaching me almost all I know about LIF and Dr. David Crosley for positive encouragement along the way.

I have been very lucky to live with a cohesive group of people during most of my graduate career. They were like a family to me. I thank Charlie Sullivan for helping me define my goals and teaching me about jazz, Anushka Drescher for her unbridled optimism, Cecilie Birner for inspiring my pun-making, and the other residents of the house on 62nd Street for keeping me sane, healthy and well-fed during my graduate work.

Finally, I thank my parents, brother and sister for making me what I was when I started graduate school. Their high expectations and relentless assistance have helped me enormously.

CHAPTER 1

Introduction

Fire has been controlled by humans for several hundred thousand years (Weinberg, 1974). Most controlled prehistoric fires burned plant matter, in which the primary mode of heat transfer to objects outside of the fire (such as humans) was radiation. In 18th century colonial America, Benjamin Franklin's famous "Franklin Stove" was an improvement over previous stoves and fireplaces in part because of higher radiant output (Lyons, 1985). Radiation has been an important mode of heat transfer from fires throughout the ages.

Many industrial processes, such as paint drying and food processing, require radiant heat. A major source of thermal radiation in industrial and domestic use has been electric radiant heaters, which offer precise control and high flexibility. However, the efficiency of electric power generation (60% loss) and transmission (5% loss) is low enough that one seeks a direct source of thermal radiation from a natural gas powered device. The gas-fired radiant heater (also called "radiant burner" in this dissertation), which generates

thermal radiation directly through combustion of natural gas, is a promising technology for efficient and economical generation of radiant heat with minimal pollutant emission.

Radiant burners are excellent choices for applications that require high radiant heat flux. Replacing electric radiant heaters with gas-fired burners can lead to lower energy consumption and lower operating costs. Even in processes that do not require high radiant flux, radiant heat transfer is effective because it is a uniformly distributed heat flux, is not affected by flowing gases, and can be focused or reflected as needed.

1.1 DEFINITIONS AND NOMENCLATURE

Before describing some commonly used gas-fired radiant heaters, a few important definitions and nomenclature notes are provided. In this dissertation, the terms *gas-fired radiant heater* and *radiant burner* are used interchangeably even though some radiant burners have been designed to use liquid fuels (e.g. Tseng and Howell, 1996). The only fuel considered in this dissertation is methane, which is a good approximation of natural gas (typically > 90% CH_4).

A *screen* is a porous medium that is placed a short distance (5-50 mm) downstream of a radiant burner. Alternative names such as "insert", "reverberator", or "reverberatory screen" are sometimes used to describe this

second porous medium. In this dissertation, the term *screen* will be used to refer to the second (downstream) porous medium.

Firing rate is an energy flow rate. It is defined as the product of fuel flow rate and the fuel heating value, that is,

$$\text{Firing Rate} = Y_f \cdot \dot{m}'' \cdot HHV \qquad [1\text{-}1]$$

where Y_f is the mass fraction of fuel, $\dot{m}''$ is the mass flow rate of fuel and air per unit area ($kg/m^2\text{-}s$), and HHV is the higher heating value of the fuel (55.6 $MJ/kg\text{-}CH_4$). The choice of higher heating value instead of lower heating value in the firing rate definition is arbitrary. There is no clear advantage or disadvantage for either heating value. The units of kW/m^2 are used for firing rate in this dissertation (note that $315\ kW/m^2 = 100{,}000\ Btu/hr\text{-}ft^2$).

The *radiant efficiency* is an important performance metric for radiant burners. It is defined as the fraction of input energy that is converted to radiant energy:

$$\text{Radiant Efficiency} = \frac{\text{Radiant Flux}}{\text{Firing Rate}} \qquad [1\text{-}2]$$

A similar radiant efficiency for electric radiant heaters can be defined as the ratio of radiant flux to the input electrical power per unit area.

1.2 DESCRIPTION OF RADIANT BURNERS

Radiant burners are divided into many classes and sub-classes. This section describes many of the important types of radiant burners, which are shown in a tree diagram in Figure 1-1. Only the burners with names in boxes are investigated in this dissertation. Several types of radiant burners are described to provide a context for the research in this dissertation. Reports by Tidball *et al.* (1989) and Harder *et al.* (1987) also contain descriptions of radiant burner designs.

The first division of radiant burners is into indirect-fired burners and direct-fired burners. Indirect-fired burners contain the flame and prevent combustion products from contacting the object being heated (the "load"). In contrast, the combustion products from a direct-fired burner can contact the load. The most common indirect-fired burners enclose a flame inside a tube. They are called radiant-tube burners. The flame—usually a non-premixed jet flame—heats the inside of the tube, which then radiates to the load. Figure 1-2a shows a schematic of a radiant-tube burner. Fuel and air enter on the bottom left and burn within the enclosure. The hot combustion products pass through the tube, heating it to incandescence. The inside of the tube is designed to facilitate a high heat transfer rate between the tube and the hot gas flowing through the tube.

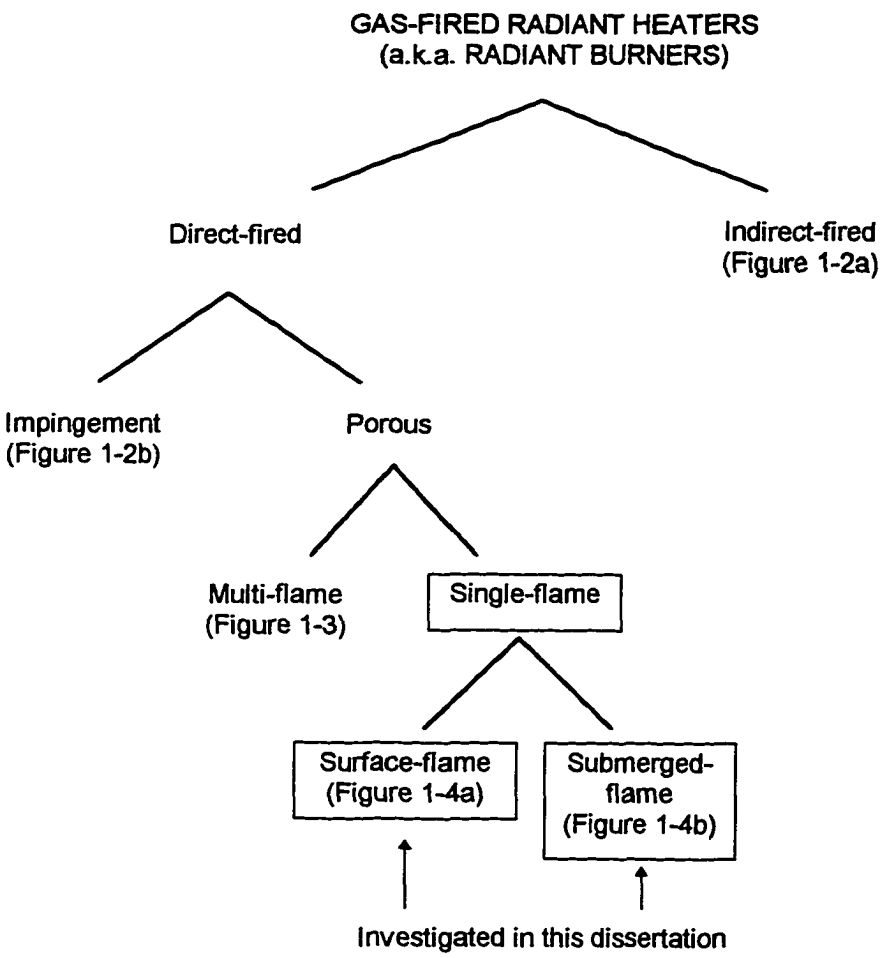

Figure 1-1: Classes of gas-fired radiant heaters. Only the burners in boxes are investigated in this dissertation.

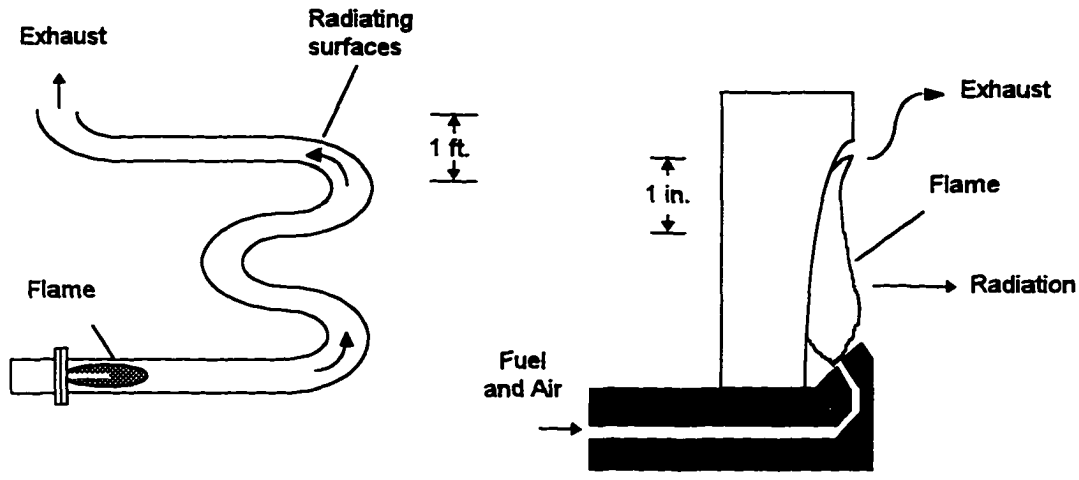

Figure 1-2: Two types of radiant burners. a.) Indirect-fired radiant burner. b.) Direct-fired impingement radiant burner. An approximate scale is noted for each device. Figures adapted from Tidball *et al.* (1989).

Radiant-tube burners have several disadvantages. Emissions of nitrogen oxides ($NO_x \equiv NO + NO_2$) can be quite high when a non-premixed flame is used because the non-premixed flame might have hot zones which can lead to elevated NO_x formation rates. Also, the limited contact between the flame and surface can lead to low radiant efficiency, which may require use of large tubes to achieve the required heat flux. Despite these short-comings, radiant-tube burners are frequently used in situations where contamination of the load is unacceptable, such as in metal treating. For more about radiant-tube burners, see Harder *et al.* (1987), Blevins *et al.* (1994), Ramamurthy *et al.* (1995), or Blevins and Gore (1996).

Direct-fired radiant burners can be divided into two classes, depending on the flow path of the gas and the position of the flame: impingement radiant burners and porous radiant burners. Figure 1-2b shows an impingement radiant burner in which a flame impinges on a refractory surface. The surface is heated by the flame and radiates to the load. Several features of this design limit its usefulness, such as the small contact area between solid and gas. The possibility of high refractory temperatures, though, makes these burners a popular choice for high temperature applications such as metal treating.

In porous direct-fired radiant burners the combustion gases pass through the radiating material. Porous direct-fired radiant burners can be further sub-divided into two classes: burners which consist of multiple flames ("multi-flame burner") and burners which consist of one continuous flame ("single-flame burner"). The ported-tile burner is a popular multi-flame porous direct-fired radiant burner (see Figure 1-3) . Ported-tile burners are made from a non-porous ceramic block that has been cast with an array of holes. Premixed air and fuel flow through each hole and a small premixed flame from each hole heats the ceramic block. The small contact area between the flame and the ceramic limits the efficiency of ported-tile burners.

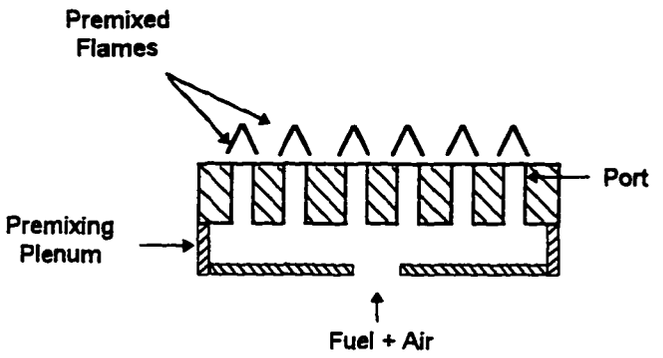

Figure 1-3: Cross section diagram of a ported-tile burner. A premixed flame stabilizes at the exit of each port in the tile.

Single-flame burners can be further subdivided into two sub-classes: burners in which a single flame is on the surface of the porous medium ("surface-flame burner") and burners in which a single flame is entirely within the porous medium ("submerged-flame burner"). Figure 1-4 shows schematic drawings of a surface-flame burner and a submerged-flame burner. The porous medium can take many forms, with porous media in current designs consisting of metal fibers, ceramic fibers, bonded hollow spheres, and ceramic foam, to name a few. In this dissertation, the term "surface-flame burner" will be used to refer to a "single-surface-flame porous direct-fired radiant burner". The term "submerged-flame burner" will be used to refer to a "single-submerged-flame porous direct-fired radiant burner".

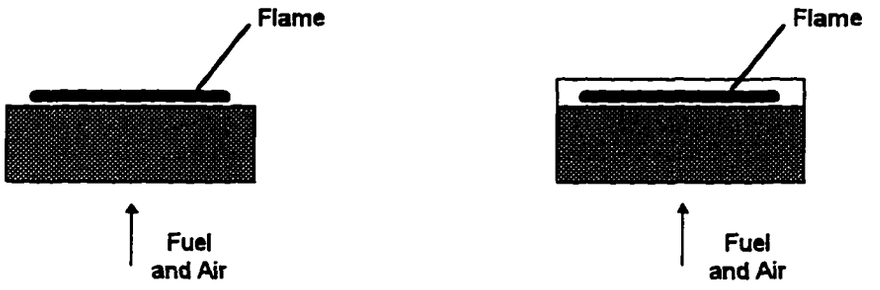

a.) Surface-flame burner b.) Submerged-flame burner

Figure 1-4: Two types of porous direct-fired radiant burners. a.) Surface-flame burner, in which the flame stabilizes on the surface of the burner. b.) Submerged-flame burner, in which the flame stabilizes in a portion of the porous medium. An approximate flame position is noted for each device. In each burner a continuous flame exists, in contrast to the multiple flames in the ported-tile burner.

1.3 APPLICATIONS OF DIRECT-FIRED RADIANT BURNERS

In the final report from a three year study of the "Radiant Burner Technology Base", Tidball *et al.* (1989) described three process heating markets that could benefit significantly from direct-fired radiant burners: metal processing, glass processing, and chemical processing. This section contains the descriptions of these three industries from Tidball *et al.* (1989) and descriptions of radiant burner applications from several other researchers.

1.3.1 Metal Processing

Metal heat treating and processing is a diverse field, with many requirements for source temperature, gaseous emissions, and heater durability. For applications that do not need a controlled atmosphere or high oxygen levels, direct-fired

radiant burners can be used. Tidball *et al.* (1989) stated that the high heat transfer rates from radiant burners could increase energy efficiency in forging and hot rolling processes. Normalizing, annealing or hardening typically takes place inside furnaces with heaters positioned above the load. Electric elements or radiant-tube burners are sometimes used to allow careful control of the furnace temperature. Some direct-fired radiant burners, such as burners with a porous medium made of metal fibers, can meet precise temperature control requirements while providing lower operating costs and shorter heat-up times. Most direct-fired radiant burners have a smaller thermal mass than electric elements or radiant tubes.

1.3.2 Glass Processing

Glass tempering and forming processes typically rely on electric heating elements. Although electric elements allow excellent control, the heat-up time can be significant, which may require that the elements be operating at all times—even when the furnace is empty. Direct-fired radiant burners, with their nearly instant on/off nature, can allow the furnace to be shut off between each operation, thus reducing energy costs (Tidball *et al.*, 1989).

1.3.3 Chemical Processing

Many synthesis processes in the chemical industries require careful application of heat to the chemicals. Heating of pipes with impinging flames can lead to

excessive temperatures in small areas of the pipes, which can cause fouling or result in a damaged product. A direct-fired radiant burner with a concave porous medium could be used to evenly heat a pipe or tank, thus preventing hot spots (Tidball *et al.*, 1989).

1.3.4 Paper Drying

In the paper industry, infrared heaters are commonly used to dry coatings and starches (Lee, 1994). About 3% of infrared heaters in paper drying processes are gas-fired radiant heaters (Kuang *et al.*, 1995). Goovaerts *et al.* (1991) installed direct-fired radiant burners into a paper plant to increase the speed of hot pressing, to incorporate preheating of the paper into the process, and to increase drying capacity. Based on their experimental results, they suggested four advantages of using a high temperature (> 1150°C) direct-fired radiant burner: 1.) the high radiant flux increases the drying rate of the paper, 2.) the burner emission spectrum closely matches the absorption spectrum of water , 3.) the burner system has a claimed drying efficiency of 60% (energy transferred to the paper sheet/input energy), which is higher than the drying efficiency of electric systems, 4.) the lifetime of the porous medium is significantly longer than that of an electric heating element. In full-scale tests in a pulp dryer Goovaerts *et al.* (1991) obtained an average speed-up of 5.2%. They also found that the gas-fired drying processes had no negative effects on paper quality.

Mattsson *et al.* (1990) examined heating for coated paper drying in pilot-scale tests. They analyzed radiant efficiency (radiant flux/input energy), operating costs, and product quality for gas-fired radiant heaters and electric radiant heaters. The spectral distribution of the gas-fired radiant heaters that were tested matched the absorption properties of uncoated printing paper better than the electric radiant heaters. They calculated that a gas-fired system would have energy costs that are approximately 30% of the energy costs of the electric system. However, they found that for their pilot-scale test, electric elements were superior in terms of space requirements and heat-up speed.

1.3.5 Coating and Paint Drying

Automakers, appliance manufacturers, and other industries that coat metal have long used solvent-based coatings because of the short cure time associated with solvents. However, as air quality regulations for volatile organic compounds become more stringent and the costs of storage, insurance, and disposal of solvents increase, many manufacturers are switching to powder- or water-based coatings (Anonymous, 1991), which require longer dry time than solvent-based coatings. Thus, drying ovens with wavelength-tuned infrared heaters are being developed. Gas-fired radiant heaters could prove useful in this field, especially because the emission of the radiating medium can be tuned with coatings or embedded materials (Tong and Li, 1996).

1.3.6 Food Processing

Food processing by far-infrared radiation can reduce processing time, energy cost, result in compact and automatic ovens, improve product quality, and decrease microorganism contamination (Sakai and Hanzawa, 1994). In this case, the far infrared is defined as radiation with wavelengths between 2.5 and 30 μm; the blackbody that will emit the largest fraction of radiation in that region has a temperature of under 500 K. The major components of foodstuffs—water, proteins, and starches—absorb infrared energy with wavelength longer than about 3 μm. Wavelengths shorter than 3 μm do not effectively cook the food. Thus, for efficient use of energy, a low temperature heat source is appropriate. Most current radiant burners do not efficiently operate with surface temperatures of under 500 K, but a new generation of catalytic radiant burners that could operate at low firing rates might better meet the needs of the food processing industry (Rumminger *et al.*, 1996).

1.4 LITERATURE REVIEW

Recent reviews by Viskanta (1995) and Howell *et al.* (1995) described the state of research on combustion in porous media. They discussed experiments, modeling, and properties of various kinds of radiant burners.

A recent Ph.D. thesis (Kulkarni, 1996) from Arizona State University discussed numerical modeling and experimental investigation of radiant

burners. There are several important differences between that work and this dissertation. The most important difference is perspective. Researchers at Arizona State (Kulkarni, Sathe, Peck and Tong) published some of the first papers about radiant burners and they treated the burners as a porous medium with a dispersed heat source, such as a flame that is fixed in one position. Their focus has been on heat transfer in the burners. While this is useful for understanding how burner properties affect heat transport from the (fixed) flame, it neglects the fact that a premixed flame is a dynamic object that stabilizes where the flame speed equals the unburned gas velocity. As burner properties, fuel-air flow rate, or the fuel-air mixture changes, the flame adjusts to a new equilibrium position. Modeling surface- and submerged-flame burners with a non-fixed flame is an example of the combustion-oriented perspective in this dissertation. Another example is the use of extensive chemical kinetics for radiant efficiency and pollutant formation modeling.

The next two sections review the literature related to the radiant burners investigated in this dissertation (i.e. porous direct-fired single-flame radiant burners). Section 1.4.1 discusses previous research on surface-flame burners. Section 1.4.2 describes previous research on submerged-flame burners.

1.4.1 Surface-Flame Burners

Surface-flame burners are versatile and can be used as a source of thermal radiation or as a stable premixed burner with low-NO_x emissions. At a firing rate under about 450 kW/m^2 (Singh, 1996), the burner surface glows uniformly and is in the "radiant mode". As the flow increases, the flame might lift off the surface in part of the burner, resulting in little radiation from the relatively cool porous medium, thus giving rise to the name "blue-flame mode". The cause of such partial lift-off has not been conclusively determined and could be related to spatial variation in the porous medium and/or the premixed gas flow field.

Models to date have varied significantly in the treatment of combustion reactions. Several attempts have been made to analytically model a radiant burner (Golombok *et al.*, 1991; Escobedo and Viljoen, 1994). These studies used a one-step irreversible chemical reaction to approximate the flame and used asymptotic analysis to solve the conservation equations. Andersen (1992) approximated the flame with an arbitrary heat release function (e.g., a delta function) and numerically solved the conservation equations. Other models have employed a one-step chemical mechanism (Chen *et al.*, 1987; Sathe *et al.*, 1991). Hsu and Matthews (1993) demonstrated important differences between models that use one-step chemistry and models that use multistep chemistry for radiant burner simulation. One-step chemistry concentrates all of the heat release in a flame zone that is much narrower than typical flames, whereas the

multistep chemical reactions in combustion expand the reaction zone. Incomplete combustion—which is not modeled by the one-step chemistry of the above papers—decreases the ultimate heat release. Hsu and Matthews (1993) reported that these differences caused single-step peak temperature predictions to be 5% to 20% higher than the multistep predictions for combustion of methane in a porous medium.

Although Hsu and Matthews (1993) cited many important differences between single-step and multistep chemistry, they neglected to mention two other benefits of multistep chemical modeling. First, the parameters in the one-step reaction rate expression are generally empirical parameters that are not independent of the experimental conditions at which they were formulated. In contrast, a reaction mechanism that consists of elementary reaction steps can be extrapolated to conditions beyond those of the experiments that determined the individual reaction rates in the chemical mechanism (Warnatz, 1992). Second, the use of multistep chemistry allows prediction of flame position, which is a critical part of radiant burner behavior. For a direct-fired radiant burner, the heat source is a premixed flame. Premixed flames have a characteristic burning velocity that depends only on mixture composition, pressure, heat losses, and initial temperature (Fristrom, 1995). The flame will adjust to the burner surface so that resulting heat loss leads to a burning velocity that is equal to the speed of the incoming unburned gas.

Other researchers have modeled surface-flame burners with a skeletal methane mechanism that does not contain nitrogen chemistry (Van der Drift *et al.*, 1994) or with a skeletal mechanism and post-processing for complex nitrogen chemistry (Bouma *et al.*, 1995). Researchers have utilized models with multistep chemistry, but specified the flame location by attaching the flame to the numerical mesh at one point (Kulkarni and Peck, 1993; Kulkarni, 1996), which could result in incorrect results for the reasons listed in the section immediately above.

Levinsky (1989) simulated a surface-flame burner with a burner-stabilized premixed flame code by assuming that the heat transferred from the flame to the burner emerged as radiant energy. However, the code was not suitable for analysis of burner properties. He analyzed the effect of flow conditions and exhaust gas recirculation on radiant efficiency and pollutant emission.

The work of researchers at Alzeta Corporation (Santa Clara, California) has revealed much about surface-flame burner operation (for example, Tidball *et al.*, 1991; Bartz *et al.*, 1992; Kendall *et al.*, 1992; Sullivan and Kendall, 1992) and has stimulated innovation in the radiant burner industry. Sullivan and Kendall (1992) modeled the gas downstream of surface-flame burner with multistep kinetics and analyzed NO_x formation. Variation of burner properties is not possible with their model because only the gas downstream of the burner

is simulated. The model calculated a surface boundary gas temperature and then solved conservation of species, energy and mass for the gas downstream of the burner surface. They reported NO_x predictions that were reasonable, but lower than their experimental measurements and attributed this to uncertainty in Fenimore-NO_x initiation reaction, $CH+N_2 \rightarrow HCN+N$.

Williams *et al.* (1992) made extensive measurements on a cylindrical-shaped ceramic-fiber surface-flame burner operating in radiant mode. They measured gas temperature, radiant efficiency, surface temperature, major species profiles and NO_x profiles. From their experimental measurements and kinetic calculations, they concluded that the Fenimore pathway was the most important NO_x formation route in radiant mode at firing rates of around 300 kW/m^2 (for $\phi < 1$).

1.4.2 Submerged-Flame Burners

Compared with surface-flame burners, submerged-flame burners offer the possibility of higher radiant efficiency and/or super-adiabatic flame speed. Some researchers have focused on increasing the flame speed, reducing the lean flammability limit, or enabling combustion of low heat-content fuels (Weinberg, 1974; Echigo, 1982; Echigo, 1985; Hsu *et al.*, 1993; Howell *et al.*, 1995). These burners are significantly different in geometry and operation than the ones studied in this dissertation. For example the porous medium in the burners

studied at the University of Texas at Austin (Hsu *et al.*, 1993; Howell *et al.*, 1995) was about 10-cm thick (see Figure 1-5a) and the flame speed was above the adiabatic laminar flame speed. Reasons given for the higher flame speed include heat recirculation (through radiation and conduction) and turbulent combustion (Hall and Hiatt, 1994). Additionally, mixtures below the lean limit were combusted in the burner. Liquid fuel combustion was also investigated (Kaplan and Hall, 1995; Tseng and Howell, 1996).

In contrast to the submerged-flame burners mentioned in the previous paragraph, the submerged-flame burners modeled in this dissertation are designed to operate below the adiabatic laminar flame speed; high radiant output and low pollutant emissions are the primary goals. Figure 1-5b shows an example of a submerged-flame burner. The burner studied in this dissertation is made from reticulated ceramic (definition of reticulated: "resembling a net; *esp*: having veins, fibers or lines crossing" (Merriam-Webster, 1987)). Hence, we call it a bilayer reticulated-ceramic burner (a short version of its complete name, porous bilayer reticulated-ceramic submerged-flame direct-fired radiant burner). It has an upper layer with large pores (the "downstream layer") and a lower layer with small pores (the "upstream layer"). Our modeling predictions are consistent with the observation that the flame stabilizes at or near the interface of the two layers.

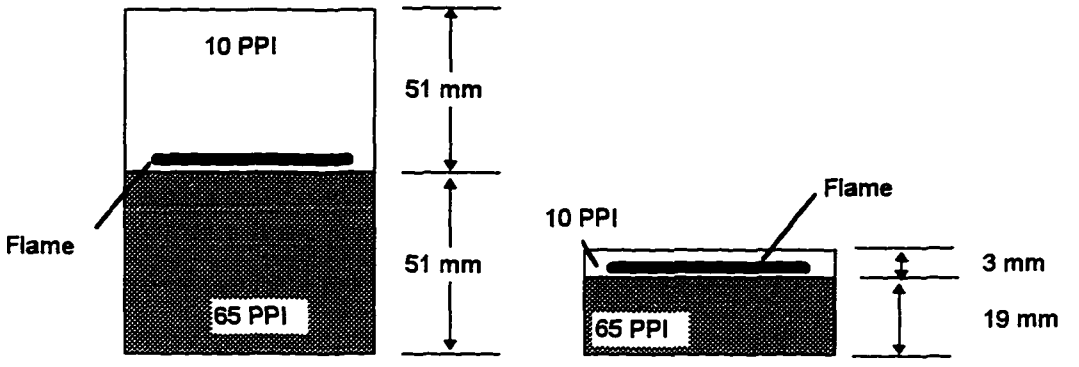

a.) UT Austin burner

b.) Burner investigated in this dissertation

Figure 1-5: Cross sections of two submerged-flame burners. a.) Porous-inert medium burner used by researchers at the University of Texas at Austin (e.g. Hsu *et al.*, 1993) b.) Submerged-flame burner studied in this dissertation. The approximate location of the flame is noted.

Although there are numerous commercial manufacturers and users of reticulated-ceramic burners, we know of only two reported studies of reticulated-ceramic burner performance (Mital *et al.*, 1995; Mital *et al.*, 1996). Mital *et al.* (1995) measured radiant efficiency and emissions for the same type of reticulated ceramic burners as those examined in this dissertation. Using micro-thermocouples and micro-probes, Mital *et al.* (1996) performed detailed measurements of gas temperature and species concentration above and within the upper layer. Data from their studies are compared with model predictions in Chapter 6.

1.5 MOTIVATION

Our research goal is to improve the radiant efficiency and expand the stable operating range of porous direct-fired radiant burners while keeping NO_x and CO emissions suitably low. To meet the goal, we are creating and using a comprehensive numerical model that simulates combustion in surface-flame burners and submerged-flame burners. A numerical model is a valuable tool because the number of possible variations of surface-flame burners and submerged-flame burners is staggering. Burners can be constructed with different pore sizes, fiber diameter, porosity, material, and thickness. Multiple layer structures can also be formed, thus adding to the number of possibilities. With so many parameters to vary, experimental parametric studies would be costly and time-consuming. A numerical model allows free variation of burner properties to investigate many different burner designs with minimal effort. Furthermore, a numerical model of a porous radiant burner allows unique insight to burner processes. For example, heat propagation in the porous medium and flame stabilization can be investigated with a numerical model.

1.6 SCOPE OF THE DISSERTATION

This dissertation analyzes heat transfer and chemical kinetics in three types of porous direct-fired radiant burners: 1.) surface-flame burners, 2.) surface-flame burners with a second porous medium (a "screen") downstream of the first

porous medium, and 3.) submerged-flame burners. One can look at the three types of burners as an evolution from surface-flame burner to surface-flame burner with a screen, to burner with a fully submerged flame. The submerged-flame burner is essentially a surface-flame burner with screen when the separation distance is zero.

Chapter 2 describes the radiant burner model in detail, discusses numerical methods, porous medium properties, and chemical kinetics. Chapter 3 investigates surface-flame burners operating in blue-flame and radiant mode. Experimental data are compared with model predictions. Simulations are performed to assess the effect of burner design on radiant efficiency for surface-flame burners with a single layer porous medium. A short investigation of a bilayer surface-flame burner is also presented. In Chapter 4 the formation of NO_x in surface-flame burners is thoroughly investigated, including analysis of NO_x formation mechanisms. Chapter 5 describes simulations of surface-flame burners acting in concert with separated "screens" (porous media placed a short distance above a radiant burner) and the implications for pollutant formation and burner efficiency. A bilayer submerged-flame burner is analyzed in Chapter 6. Experimental measurements of gas temperature are described and data from other researchers are compared with the model predictions. A summary, conclusions, and suggestions for future research are presented in Chapter 7.

References cited in a chapter are listed at the end of the respective chapter. An additional list of all of the references cited in the dissertation follows the Summary and Conclusions (Chapter 7).

1.7 REFERENCES

Andersen, F. (1992), "Heat Transport Model for Fibre Burners", *Progress in Energy and Combustion Science* 18, pp. 1-12.

Anonymous (1991), "Infrared Paint Curing Heats Up", *Manufacturing Engineering* 106(1), p. 22.

Bartz, D.F., Moreno, F.E., and Duggan, P.A. (1992), "Ultra-low NO_x Ultra-High *VOC* Destruction with Adiabatic Radiant Combustors", *Fossil Fuel Combustion* (Roberto Ruiz, Ed.), ASME PD-39, pp. 7-12.

Blevins, L.G., Sivathanu, Y.R., Shahien, M.A., and Gore, J.P. (1994), "A Study of Global Properties of Radiant Tube Flames", *Proceedings of the First ISHMT-ASME Heat and Mass Transfer Conference and Twelfth National Heat and Mass Transfer Conference*, Tata McGraw-Hill (New Delhi), January 5-7, Bombay, India.

Blevins, L.G. and Gore, J.P. (1996), "Radiative Efficiency of a Quartz Radiant Heating Tube", *Combustion Science and Technology* 112, pp. 369-374.

Bouma, P.H., Eggels, R.L.G.M., Somers, L.M.T., de Goey, L.P.H., Nieuwenhuizen, J.K. and van der Drift, A. (1995), "A Numerical and Experimental Study of the NO-Emission of Ceramic Foam Surface Burners", *Combustion Science and Technology* 108(1-3), pp. 193-203.

Bouma, P.H., Somers, L.M.T., de Goey, L.P.H., and Nieuwenhuizen, J.K. (1994), "Modelling of Methane-Air Combustion on Ceramic Foam Surface Burners in the Radiation Mode", presented at the Eurotherm Seminar number 37 'Heat Transfer in Radiating and Combusting Systems-2', Saluggia, Italy, 5-7 October.

Chen, Y.-K., Matthews, R.D., and Howell, J.R. (1987), "The Effect of Radiation on the Structure of Premixed Flame within a Highly Porous Inert Medium", in *Radiation, Phase Change Heat Transfer and Thermal Systems* (Y. Jaluria *et al.*, Ed.), ASME HTD-81, pp. 35-41.

Echigo, R. (1982), "Effective Energy Conversion Method Between Gas Enthalpy and Thermal Radiation and Application to Industrial Furnaces", in *Proceedings of the 7th International Heat Transfer Conference*, Hemisphere Publishing Corp. (Washington, D.C.), Vol. VI, p. 361.

Echigo, R. (1985), "Radiative Heat Transfer Enhancement to a Water Tube by Combustion Gases in Porous Medium", *Proceedings: International Symposium on Heat Transfer*, Vol. 3, pp. 186-193.

Escobedo, F. and Viljoen, H.J. (1994), "Modeling of Porous Radiant Burners with Large Extinction Coefficients", *Canadian Journal of Chemical Engineering* 72(5), pp. 805-814.

Fristrom, R.M. (1995), *Flame Structure and Processes*, Oxford University Press (New York).

Golombok, M., Prothero, A., Shirvill, L.C., and Small, L.M. (1991), "Surface Combustion in Metal Fibre Burners", *Combustion Science and Technology* 77, pp. 203-223.

Goovaerts, J., Ratnani, K. and Hendry, B (1991), "Infrared Applications in Pulp Drying", *Pulp and Paper Canada* 92(11), pp. 24-27.

Hall, M.J. and Hiatt, J.P.(1994), "Exit Flows from Highly Porous Media," *Physics of Fluids* 6(2), pp. 469-479.

Harder, R.F., Viskanta, R., and Ramadhyani, S. (1987), "Gas-Fired Radiant Tubes: A Review of the Literature", Gas Research Institute Report, GRI-87/0343.

Howell, J.R., Hall, M.J. and Ellzey, J.L. (1995), "Combustion within Porous Inert Media", in *Heat Transfer in Porous Media and Two-Phase Flow*, (Y. Bayazitoglu and U.B. Sathuvalli, Ed.), ASME HTD-302, pp. 1-28.

Hsu, P.-F., and Matthews, R.D. (1993), "The Necessity of Using Detailed Kinetics in Models for Premixed Combustion in Porous Media", *Combustion and Flame* 93(4), pp. 457-466.

Hsu, P.-F., Evans, W.D., and Howell, J.R. (1993), "Experimental and Numerical Study of Premixed Combustion within Nonhomogenous Porous Ceramics", *Combustion Science and Technology* 90, pp. 149-172.

Kaplan, M. and Hall, M.J. (1995), "The Combustion of Liquid Fuels within a Porous Media Radiant Burner", *Experimental Thermal and Fluid Science* 11(1), pp. 13-20.

Kendall, R.M., DesJardin, S.T., Sullivan, J.D. (1992), *Basic Research on Radiant Burners*, Gas Research Institute Report number 92-7027-171.

Kuang, H.D., Thibault, J., Chen, R., and Grandjean, B.P.A. (1995), "Pilot Scale Investigation of IR Drying of Paper", *Tappi Journal* 78(7), pp. 129-137.

Kulkarni, M.R. and Peck, R.E. (1993), "Modeling Radiant Surface Burner Performance", 1993 Fall Meeting of the Western States Section of the Combustion Institute, Menlo Park, California, Paper WSCI93-106.

Kulkarni, M.R. (1996), "Experimental and Numerical Analysis of Radiant Surface Burners", Ph.D. thesis, Arizona State University.

Lavigne, D. (1990), "A High Efficiency Gas-Fired Infrared Dryer", *Appita Journal* 43(4), pp. 258-259.

Lee, L. (1994), "Gas Infrared Drying: Update on Technology", *Pulp and Paper Canada* 95(12), pp. 102-104.

Levinsky, H.B. (1989), "A Computational Study of the Behavior of Radiant Burners", International Gas Research Conference, Tokyo.

Lyons, J.W. (1985), *Fire*, Scientific American Library, W.H. Freeman and Company (New York).

Mattsson, P., Pelkonen, J., Riikonen, A., and Oy, N. (1990), "Infrared Drying of Coated Paper", *Paperi ja Puu – Paper and Timber* 72(4), pp. 347-349.

Meng, W.H., McCordic, C., Gore, J.P., and Herold, K.E. (1991), "A Study of Effects of Porous Ceramic Inserts on Heat Transfer and Combustion in a Fired Heat Exchanger", in *ASME/JSME Thermal Engineering Proceedings*, Vol. 5, pp. 181-188.

Merriam-Webster Inc. (1987), *Webster's Ninth New Collegiate Dictionary*, Merriam-Webster, Inc. Publishers (Springfield, MA).

Mital, R., Gore, J.P., Viskanta, R., and Singh, S. (1995), "Global Radiation and Emission Characteristics of Reticulated Ceramic Radiant Burners", in *Proceedings of 1995 Joint Thermal Meeting on Combustion Fundamentals and Applications* (J.P. Gore, Ed.), Central and Western States and Mexican National sections of the Combustion Institute, pp. 32-37.

Mital, R., Gore, J.P., Viskanta, R., and Singh, S. (1996), "Structure of Submerged Flames in Reticulated Ceramic Radiant Burners", 1996 Technical Meeting of the Central States Section of the Combustion Institute, St. Louis.

Ramamurthy, H., Ramadhyani, S., and Viskanta, R. (1995) "A Thermal System Model for a Radiant-Tube Continuous Reheating Furnace", *Journal of Materials Engineering and Performance* 4(5), pp. 519-531.

Rumminger, M.D., Hamlin, R.D., and Dibble, R.W. (1996), "Numerical Analysis of a Catalytic Radiant Burner: The Effect on Radiant Efficiency and Operability", Third International Workshop on Catalytic Combustion, Amsterdam, to appear in *Catalysis Today.*

Sakai, N. and Hanzawa, T. (1994), "Applications and Advances in Far-Infrared Heating in Japan", *Trends in Food Science and Technology* 5(11), pp. 357-362.

Sathe, S.B., Peck, R.E., and Tong, T.W. (1990), "A Numerical Analysis of Heat Transfer and Combustion in Porous Radiant Burners," *International Journal of Heat and Mass Transfer* 33, pp. 1331-1338.

Singh, S.N. (1996), Personal communication, January.

Sullivan, J.D. and Kendall, R.M. (1992), "Thermal Performance and NO_x emissions from Porous Surface Radiant Burners," International Gas Research Conference, Orlando, Florida.

Tidball, R.K., Donaldson, R.J., and Gotterba, J.A. (1989), *Radiant Burner Technology Base - Burner Research and Development*, Final Report, Alzeta Report No. 89/723-724/148, March.

Tong, T.W. and Li, W. (1995), "Enhancement of Thermal Emission from Porous Radiant Burners", *Journal of Quantitative Spectroscopy and Radiative Transfer* 53, pp. 235-248.

Tseng, C.-J. and Howell, J.R. (1996), "Combustion of Liquid Fuels in a Porous Radiant Burner", *Combustion Science and Technology* 112, pp. 141-163.

van der Drift, A., Beckers, G.J.J., Smit, K., Beesteheerde, J. (1994), "An Experimental and Numerical Study of Porous Radiant Burners", presented at the Eurotherm Seminar number 37 'Heat Transfer in Radiating and Combusting Systems-2', Saluggia, Italy, 5-7 October.

Warnatz, J. (1992), "Resolution of Gas Phase and Surface Combustion into Elementary Reactions", *Twenty-Fourth Symposium (International) on Combustion*, The Combustion Institute, Pittsburgh.

Weinberg, F.J. (1974), "The First Half-Million Years of Combustion Research and Today's Burning Problems", *Fifteenth Symposium (International) on Combustion*, The Combustion Institute, Pittsburgh, pp. 1-17.

Williams, A., Woolley, R., and Lawes, M. (1992), "The Formation of NO_x in Surface Burners", *Combustion and Flame* 89, pp. 157-166.

CHAPTER 2

Numerical Modeling of Porous Direct-Fired Radiant Burners

2.1 INTRODUCTION

The number of possible variations of porous direct-fired radiant burners is staggering. The porous media in radiant burners can be constructed with different pore sizes, fiber diameter, porosity, material, and thickness. Multiple layer structures can also be formed, thus adding to the number of possibilities. With so many parameters to vary, an experimental parametric study would be costly and time-consuming. A numerical model allows free variation of burner properties and investigation of many different burner designs with minimal effort. Furthermore, a numerical burner model allows unique insight into burner processes. For example, with the model we obtain information about heat propagation in the porous medium or the location of flame stabilization.

In this chapter, a numerical model of a single-flame porous direct-fired radiant burner is described. The governing equations and boundary conditions

are presented and explained. Computational methods, chemical reaction modeling and the properties of porous media are also discussed. Note that when the terms "porous direct-fired radiant burner" or "radiant burner" are used in the following sections, they refer solely to single-flame porous direct-fired radiant burners. Other types of burners (e.g. indirect-fired radiant tubes, ported-tile burners) are not examined in this dissertation (recall Figure 1-1).

2.2 NUMERICAL MODEL

We represent a porous direct-fired radiant burner with a steady-state one-dimensional model. The one-dimensional approximation is appropriate for the burners we are studying because the flame zone is much thinner than the non-axial dimensions of the porous medium. One-dimensional models have been used successfully for flat flames on burners of similar geometry such as a water-cooled porous plug burner (Kee *et al.*, 1985).

The model in this dissertation is an improvement over previous models because it includes *all* of the following: separate energy equations for the gas and solid, multistep chemistry, a domain that allows more accurate calculation of solid boundary temperatures, a user-definable flow rate, and a radiatively participating porous medium. We use the two-flux approximation (also called the Schuster-Schwarzchild approximation) for the radiative heat transfer in the porous medium (Viskanta, 1966). The position of the flame is not fixed, but instead the flame can move as input conditions and burner properties change.

Our model was influenced by the pioneering work of Sathe *et al.* (1990) and Singh *et al.* (1992). The code is an extension of Sandia National Laboratory's one-dimensional premixed flame code (Kee *et al.*, 1985).

We assume the flame is one-dimensional and laminar, the gas is optically thin and ideal, combustion occurs at constant pressure, the porous medium is spectrally gray, and the porous medium is a hemispherically isotropic scatterer.

Figure 2-1 shows the computational domain for the model. Fuel and air enter an adiabatic, infinite duct at the left ($x = x_{in,}$), flow into the porous medium—which extends from $x = 0$ to $x = L$—and exit at $x = x_{out}$ after reacting.

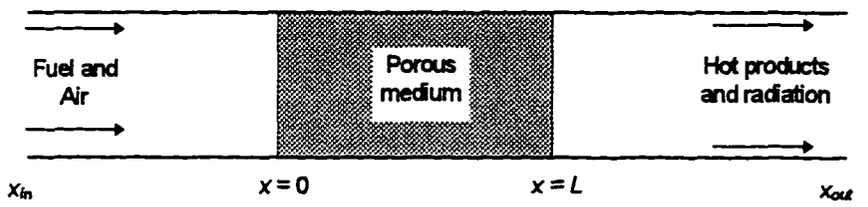

Figure 2-1: Computational domain for radiant burner model. $x = 0$ and $x = L$ are the edges of the porous medium (shaded region). Upper and lower boundary lines are shown, but the actual boundaries are at $+\infty$ and $-\infty$.

The boundary conditions for the gas are evaluated at the inlet and exit of the system (x_{in} and x_{out} in Figure 2-1) and the solid energy and radiative transfer boundary conditions are evaluated at $x = 0$ and $x = L$, points that are *between* the gas end points. The computational domain used in this formulation is unlike the domain in most of the studies cited in Chapter 1, exceptions are Sathe *et al.* (1990)

and Kulkarni (1996). The separated boundary conditions allow more accurate calculation of solid boundary temperatures, especially in surface-flame burners where a non-negligible fraction of the heat release can occur downstream of the burner surface (Williams *et al.*, 1992). Additionally, when we apply the adiabatic boundary condition to the gaseous species, we place the boundary far enough downstream (at least 15 cm) to ensure that most of the primary exothermic reactions have been completed.

2.3 GOVERNING EQUATIONS

The system is governed by equations for mass continuity, gas-phase species conservation, gas-phase energy conservation, porous-solid energy conservation, the radiative transfer equations for the solid, and the ideal gas law.

The mass continuity equation is

$$\dot{m}'' = \rho u \varepsilon \qquad [2\text{-}1]$$

where $\dot{m}''$ is the mass flow rate per unit area, ρ is the mass density of the gas, u is the gas velocity, and ε is the porosity of the solid ($\varepsilon = 1$ in the gas only region). The material is assumed to be isotropic, thus the volumetric porosity and cross-sectional area porosity are equal.

The gas species conservation equation is

$$\rho u \varepsilon \frac{dY_k}{dx} + \frac{d}{dx}(\rho \varepsilon Y_k V_k) = \dot{\omega}_k W_k \varepsilon \qquad k = 1,\ldots,kk \qquad [2\text{-}2]$$

where Y_k is the mass fraction of the k-th species, V_k is the diffusive velocity of the k-th species, W_k is the molecular mass of the k-th species, $\dot{\omega}_k$ is the production rate of the k-th species, and kk is the total number of gas-phase species. One equation is solved for each molecular species.

The gas-phase energy equation is

$$\rho u \varepsilon c_{p_g} \frac{dT_g}{dx} - \frac{d}{dx}\left(k_{g,e}\frac{dT_g}{dx}\right) + \sum_{k=1}^{kk} \rho \varepsilon Y_k V_k c_{p_k} \frac{dT_g}{dx} + h_v\left(T_g - T_s\right) = -\sum_{k=1}^{kk}\left[\dot{\omega}_k h_k \varepsilon W_k\right] \quad [2\text{-}3]$$

where c_{p_g} is the specific heat of the gas mixture, c_{p_k} is the specific heat of the k-th species, T_g is the gas temperature, T_s is the solid temperature, h_v is the volumetric convective heat transfer coefficient between the solid and gas, h_k is the enthalpy for the k-th species, and $k_{g,e}$ is the effective thermal conductivity of the gas mixture.

The porous medium energy equation is

$$\frac{d}{dx}\left[k_{s,e}\frac{dT_s}{dx}\right] + h_v\left(T_g - T_s\right) = \frac{dq_r}{dx} \quad [2\text{-}4]$$

where $k_{s,e}$ is the effective thermal conductivity of the porous medium, q_r is the net radiative flux (the difference between forward radiation flux (q^+) and backward radiation flux (q^-)) and $k_{e,s}$ is the effective thermal conductivity of the solid. Note that the effective thermal conductivity correlation for the porous medium typically includes material properties such as porosity, pore diameter, and fiber size.

The radiative transfer equations for the two-flux approximation are

$$\frac{dq^+}{dx} = -2\sigma_e q^+ + 2\sigma_e \omega_o \left(f q^+ + b q^-\right) + 2\sigma_e \left(1-\omega_o\right)\sigma T_s^4 \qquad [2\text{-}5]$$

$$-\frac{dq^-}{dx} = -2\sigma_e q^- + 2\sigma_e \omega_o \left(f q^- + b q^+\right) + 2\sigma_e \left(1-\omega_o\right)\sigma T_s^4 \qquad [2\text{-}6]$$

where ω_o is the single scattering albedo, σ_e is the extinction coefficient, f is the forward-scattering fraction (a non-isotropic scattering parameter), b is the backward-scattering fraction, and σ is the Stefan-Boltzmann constant. More details about the two-flux approximation can be found in Viskanta (1966).

The radiant efficiency of the burner is given by the following expression:

$$\text{Radiant Efficiency} = \frac{\text{Radiant Flux}}{\text{Chemical Energy Input}} = \frac{q^+(L) - q^-(L)}{\text{Firing Rate}} \qquad [2\text{-}7]$$

The firing rate is the product of the fuel flow rate and the higher heating value of the fuel (methane in this dissertation).

2.4 BOUNDARY CONDITIONS

Boundary condition at the gas inlet (x_{in}) is given by

$$T_g = T_{given}, \quad Y_k = Y_{k,given} \qquad [2\text{-}8]$$

The gas inlet (x_{in}) is typically placed 3-5 cm upstream of the porous medium.

The boundary condition at the upstream face of the porous medium ($x = 0$) by

$$-(1-\varepsilon)k_s \left.\frac{dT_s}{dx}\right|_{x=0} = h_o\left(T_g - T_s\right) - \left(q^-(0) - q^+(0)\right) \qquad [2\text{-}9]$$

$$q^+(0) = eQ_+ + \chi_o q^-(0) \qquad [2\text{-}10]$$

where h_o is the convective heat transfer coefficient (per unit area), Q_+ is the ambient radiant flux from negative infinity (e.g. the burner housing), χ_o is the reflectivity of the porous medium, and e is the average emissivity of the surface.

At the downstream face of the porous medium ($x = L$) we find the porous medium temperature such that the total radiant losses from the burner equal the net convective heat transfer from the gas to the porous medium (which *is* also equal to the product of $\dot{m}''$ and the enthalpy change of the gas between x_{in} and x_{out}). Since non-radiative heat losses are not included in the model, any net heat transfer from the gas to the porous medium must emerge as radiant energy. We chose this approach—as opposed to solving an equation similar to Eq. [2-9] at the boundary—because the downstream face of the porous medium is a point at which the porous medium energy equation is evaluated on a per-unit-area basis, while the gas-phase energy equation is evaluated on a per-unit-volume basis. Also, the knowledge of the convection coefficient at the downstream solid boundary is highly uncertain. The complex geometry of the downstream porous medium surface has prevented measurements of the (area-based) convection coefficient. Thus, to avoid use of highly uncertain properties (the convective heat transfer coefficient *and* area-to-volume conversion), an energy balance is

used. We do not use this energy balance method at the upstream boundary because temperatures are lower, the convective heat transfer rate is smaller, and radiant emission is significantly smaller.

The backward radiant flux value at the boundary is found with the following expression:

$$q^{-}(L) = eQ_{-} + \chi_o \, q^{+}(L) \qquad [2\text{-}11]$$

where Q_- is the ambient radiant flux from positive infinity (e.g., the recipient of the radiation, called the load).

We assume that the main exothermic reactions are complete and the gas is adiabatic at the gas outlet

$$dT_g/dx = 0, \quad dY_k/dx = 0 \qquad [2\text{-}12]$$

The computational boundary for the gas outlet is typically 10 to 15 cm downstream of the porous medium.

2.5 COMPUTATIONAL METHODS

We find steady-state solutions with a modified-damped Newton-Raphson method, *Twopnt* (Grcar, 1992), on *DEC 3000 Alpha* computers. Solution time depends strongly on the initial guess and varies from several minutes to several hours. The solver uses an adaptive gridding technique and solutions typically contain 100-150 grid points. For numerical convergence, we specify an absolute tolerance of 10^{-10} and a relative tolerance of 10^{-5}.

A detailed description of the modified damped Newton's method for two-point boundary value problems used in *Twopnt* is in Grcar (1992). Extensive notes about the application of *Twopnt* can be found in the manuals of *Premix* (Kee *et al.*, 1985) and *Spin* (Coltrin *et al.*, 1991). The purpose of the *Twopnt* algorithm is to find a solution vector that minimizes the residual of the finite difference equations. The program uses standard techniques that increase the robustness and speed of Newton's method, such as reusing Jacobian matrices, reducing the length of search step when necessary and using time stepping to move the system towards the solution.

The finite differences used in the radiant burner code follow those used in the original premixed flame code (Kee *et al.* , 1985). Windward differencing is used for nearly all first order derivatives, such as

$$\left(\dot{m}''\frac{dT_g}{dx}\right)_j \approx \dot{m}_j''\left(\frac{T_{g,j}-T_{g,j-1}}{x_j-x_{j-1}}\right) \qquad [2\text{-}13]$$

where j refers to the mesh point number. Artificial diffusion will be minimal because of the adaptive grid technique (Kee *et al.*, 1985).

The first derivative for the summation term in the gas-phase energy equation (Eq. [2-3]) is approximated by a central difference formula

$$\left(\frac{dT_g}{dx}\right)_j \approx \left(\frac{h_{j-1}}{h_j(h_j+h_{j-1})}T_{g,j+1}+\frac{h_j-h_{j-1}}{h_jh_{j-1}}T_{g,j}-\frac{h_j}{h_{j-1}(h_j+h_{j-1})}T_{g,j-1}\right) \qquad [2\text{-}14]$$

where $h_j = x_{j+1} - x_j$. The coefficients are evaluated at the current mesh point.

Adaptive grid methods are popular for combustion simulations because they allow the mesh to be dense where required, such as in the flame front, and sparse in areas where profiles are flat. The efficient placement of grids in the flame front is critical if one wants solutions in a reasonable amount of time and with good resolution. The radiant burner code begins with a coarse mesh and as solutions are found, *Twopnt* adds new grid points in regions that are not sufficiently resolved. See Grcar (1992) for full details about the adaptive grid method used in *Twopnt*.

Old solutions with the old numerical grid are used as initial guesses for new problems. After a continuous series of runs in which the flow rate or equivalence ratio was changed by a significant amount, the flame may have shifted on the numerical grid, thus leaving a collection of closely spaced grid points outside of the flame front. A regrid routine is included in the code to remove the unnecessary grid points.

2.6 CHEMICAL KINETICS

We use the *Chemkin* subroutines for chemical kinetics management (Kee *et al.*, 1989) and the *Transport* subroutines (Kee *et al.*, 1985) to calculate gas properties. The packages are modular and make many intricate calculations tractable, such as reaction rate analysis.

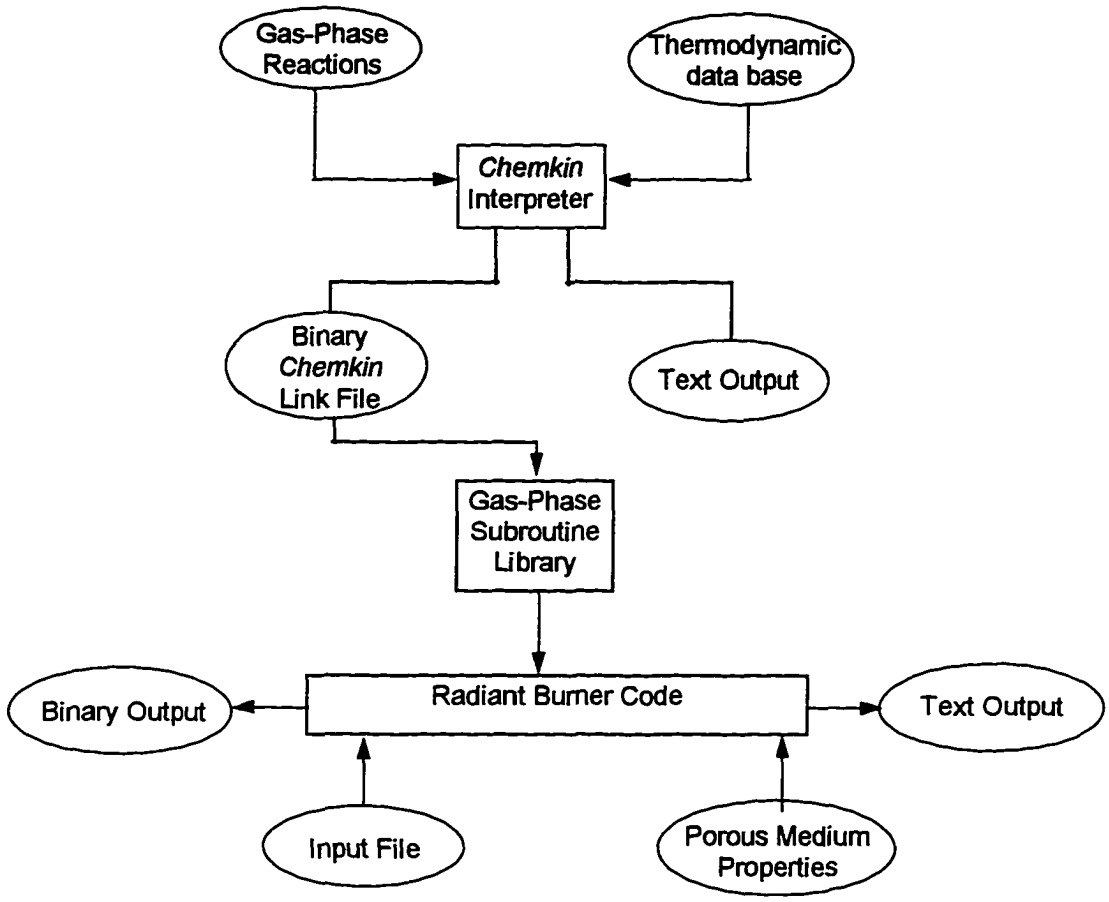

Figure 2-2: Diagram of *Chemkin* and input files and their interface with the radiant burner code (after Kee *et al.*, 1989). A FORTRAN post-processing code is used to read the binary output file from the radiant burner code.

For calculations in which NO_x formation is analyzed, we use the Gas Research Institute-developed methane-air chemical kinetic mechanism with nitrogen chemistry (GRI-Mech 2.11, Bowman *et al.*, 1995). The detailed mechanism contains methane and nitrogen chemistry with 49 species and 279 reactions. A reduced mechanism (*DRM19*, Kazakov and Frenklach, 1994) for methane combustion is used when pollutant emission results are not desired. The reduced mechanism contains 21 species and 84 reactions and was created

using a detailed reduction technique (Frenklach, 1991; Wang and Frenklach, 1991). We are interested in using the smaller mechanism primarily for reasons of convenience: smaller mechanisms run faster and allow better grid resolution (i.e., more grid points). Comparison of the full mechanism with the reduced mechanism is performed for surface-flame burners in Chapter 3. Lists of species and reactions contained in each mechanism, as well as information about obtaining the mechanisms, can be found in the appendix.

2.7 PROPERTIES OF THE POROUS MEDIA

The sensitivity of chemical reaction and radiation to temperature requires careful consideration of the properties of the porous medium. For the model described in this document, the following porous medium properties are needed: effective thermal conductivity ($k_{s,e}$), extinction coefficient (σ_e), single scattering albedo (ω_o), forward scattering fraction (f), porosity (ε), and convective heat transfer coefficient (h_v). The extinction coefficient determines how quickly radiant energy is absorbed or scattered by the porous medium; it is the sum of the scattering coefficient and the absorption coefficient. The scattering albedo is the ratio of the scattering coefficient to the extinction coefficient; it is the measure of the fraction of radiant energy that is extinguished through scattering. The thermal conductivity used for the porous medium is an *effective* thermal conductivity, which depends on the material *and* the structure of the porous

medium. The forward scattering fraction is an asymmetry parameter for the radiant heat transfer model and denotes the fraction of scattered radiation that scatters in the forward direction. The convective heat transfer coefficient is used for heat transfer between the gas and porous medium. A review of physical properties of porous media used in radiant burners was presented by Howell (1995). A review of convection in consolidated porous media was presented by Viskanta (1995).

2.7.1 Surface-Flame Burners

2.7.1.1 Metal Fiber Matrices

The porous media in some surface-flame burners consist of metal fibers that are formed into a matrix through sintering. The porosity of one commercially available metal fiber matrix has been reported to be 0.80 (Golombok, 1991). We use this value for the simulations of a surface-flame burner with a metal fiber porous medium.

The effective thermal conductivity of sintered metal fibers was studied and a correlation was developed by Mantle and Chang (1991). The correlation is

$$\frac{k_{s,e}}{k_s} = 1 + \frac{\varepsilon}{\left[(1-\varepsilon)/m\right] + \left[k_s/\left(k_g - k_s\right)\right]} \qquad [2\text{-}15]$$

where $m = [1.2\text{-}29(d/L_f)](0.81\text{-}\varepsilon)^2 + [1.09\text{-}2.5(d/L_f)]$, d is the fiber diameter, L_f is the fiber length ($L_f = 1.0$ cm was used for this study). Figure 2-3 shows how the

effective thermal conductivity varies with porosity for several fiber sizes. The effective thermal conductivity of the gas is approximated with a relation from Yagi *et al.* (1960).

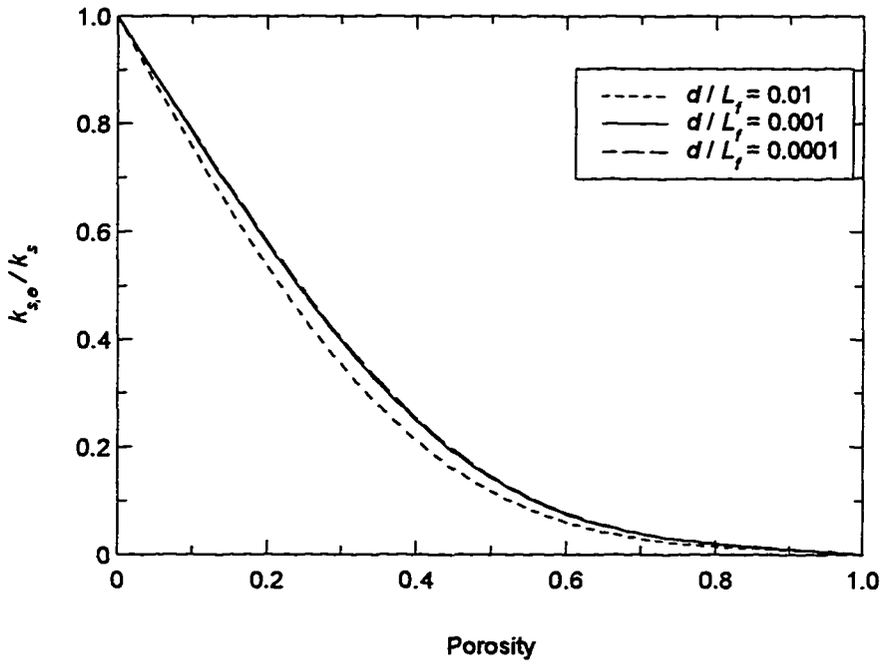

Figure 2-3: Effective thermal conductivity correlation from Mantle and Chang. k_s is the thermal conductivity of the solid in bulk form; $k_{s,e}$ is the effective thermal conductivity of the metal fiber matrix. In the legend, d denotes the fiber diameter, L_f denotes the fiber length.

The convection coefficient within a metal fiber matrix comes from measurements by Golombok *et al.* (1991). In the correlation, the Reynolds number is based on fiber diameter ($\mathrm{Re} = \dot{m}'' d / \mu$) and the Nusselt number (Nu) is based on a unit area formulation (i.e., $\mathrm{Nu} = h_o d / k$) and the fiber diameter. For Re < 0.4 the correlation is

$$\mathrm{Nu} = 0.04\ \mathrm{Re}^{0.53} \qquad [2\text{-}16]$$

For Re > 0.4 the correlation is

$$\mathrm{Nu} = 0.10\ \mathrm{Re}^{1.64} \qquad [2\text{-}17]$$

The following equation from Golombok *et al.* (1991) is used to convert from area-based convection coefficient to volumetric convection coefficient:

$$h_v = \frac{4\ \mathrm{Nu}\ k_g(1-\varepsilon)}{d^2} \qquad [2\text{-}18]$$

Other properties for the porous medium are reasonable estimates: extinction coefficient of 1000 m^{-1}, scattering albedo of 0.65, and a forward scattering fraction of 0.6.

2.7.1.2 *Ceramic Fiber Matrices*

Although surface-flame burners that have a ceramic fiber porous medium are not analyzed in detail in this dissertation, sizable amounts of experimental data on their performance exists. In Chapter 3 and Chapter 5 model predictions are compared with experimental data for ceramic fiber surface-flame burners.

The following reasonable estimates are used for the ceramic fiber porous medium properties: porosity of 0.93, effective thermal conductivity of 0.05 W/m-K, extinction coefficient of 1000 m^{-1}, single scattering albedo of 0.7, and forward scattering fraction of 0.65. The volumetric convective heat transfer coefficient is from a correlation reported in Andersen (1991)

$$h_v = f_h \frac{k_g \dot{m}''}{\mu_g L} \qquad [2\text{-}19]$$

where f_h is an arbitrary adjustment factor ($f_h = 120$ is used here to acheive realistic surface temperatures), μ_g is the gas viscosity, L is the thickness of the porous medium.

2.7.1.3 *Ceramic Foam*

Surface-flame burners that have a porous medium made of ceramic foam are not studied in this dissertation (see Bouma *et al.* (1995) for work on ceramic foam surface-flame burners). However, submerged-flame burners that use ceramic foam are simulated. Information about the properties of those ceramic foams, which could be used for simulation of ceramic foam surface-flame burners, can be found in the section below.

2.7.2 Submerged-Flame Burners

For submerged-flame burners, radiant properties of the ceramic are critical because the flame stabilizes completely within the porous medium. The porous medium is typically bilayered, with a diffuse downstream layer and dense upstream layer. Incorrect properties for the porous medium can cause numerical non-convergence or can cause the flame to stabilize on the surface instead of inside of the porous medium. Some measurements of thermal properties of porous ceramics have been made for partially stabilized zirconia (Hsu and Howell, 1993; Hendricks and Howell, 1994) and silicon carbide (Hendricks and Howell, 1994). Mital *et al.* (1995) measured the extinction coefficient and

scattering albedo of YZA, mullite, silicon carbide, silicon carbide-coated-cordierite and uncoated cordierite. Although measurements were made for only 4, 6, and 8 pore-per-cm (PPC) samples, estimates have been made for the 25 PPC downstream layer (Mital and Gore, 1995). The properties that are used in the simulations in Chapter 6 are

	Upstream Layer (25 PPC)	Downstream Layer (4 PPC)
Extinction coefficient (σ_e, m^{-1})	1000	115
Scattering albedo (ω_o)	0.77	0.72
Pore diameter (d, cm)	0.022	0.22
Porosity (ε)	0.65	0.80
Bulk thermal conductivity (k_s, W/m-K)	1.0	1.0
Forward scattering fraction (f)	0.6	0.6

The convection coefficient correlation for gas flow in porous ceramics is from Younis and Viskanta (1993). They used a single-blow transient technique to find the following empirical correlation for alumina ceramic foam from Hi-Tech Ceramics (Alfred, NY):

$$\mathrm{Nu} = 0.819\left[1 - 7.33(d/L)\right]\mathrm{Re}^{0.36\left[1+15.5(d/L)\right]} \qquad [2\text{-}20]$$

where Nu is the *volumetric* Nusselt number ($\mathrm{Nu} = h_v d^2/k_g$), d is the average pore diameter, L is the length of the porous medium, and Re is the Reynolds number based on pore diameter. The correlation applies for $5.1 < \mathrm{Re} < 563$ and $0.005 < d/L < 0.136$. The volumetric convection coefficient in typical simulations

is on the order of 10^7 W/m^3-K in the upstream layer and 10^5 W/m^3-K in the downstream layer.

An experimentally determined effective thermal conductivity correlation for ceramic foam has not yet been incorporated into the model. As far as we know, no measurements of the effective thermal conductivity of ceramic foam have been made. The translation we use to convert from bulk thermal conductivity to effective thermal conductivity is $k_{s,e} = (1-\varepsilon)\, k_s$, that is, a linear dependence on $(1-\varepsilon)$. The effective thermal conductivity of the gas is approximated with a relation from Yagi *et al.* (1960).

2.7.3 Common Properties of the Porous Media

At the upstream boundary of the porous medium we use a convective heat transfer coefficient between the gas and burner surface for a stagnation flow from Kanury (1988) that is

$$\mathrm{Nu} = 0.57(1-\varepsilon)\mathrm{Re}^{0.5}\,\mathrm{Pr}^{0.4} \qquad [2\text{-}21]$$

Note that the Nusselt number is area-based. The correlation was developed for flow impinging onto a flat plate, but we have modified it for use in this application by adding the $(1-\varepsilon)$ term to approximate the area of the solid in the porous medium. This convective heat transfer coefficient is used for the upstream boundary of all burners studied in this dissertation. Neither the

surface-flame burner nor the submerged-flame burner is sensitive to the convection coefficient of the upstream edge.

2.8 SUMMARY

We represent a porous direct-fired radiant burner with a one-dimensional numerical model. Combustion in the radiant burner is modeled by equations for mass continuity, gas-phase species conservation, gas-phase energy conservation, porous-solid energy conservation, radiative transfer equations for the porous medium, and the ideal gas law. The model is an improvement over previous models because it includes *all* of the following: separate energy equations for the gas and solid, multistep chemistry, a domain that allows more accurate calculation of solid boundary temperatures, a user-definable flow rate, and a radiatively participating porous medium. The multistep kinetics are managed by *Chemkin* subroutines and a modified-damped Newton-Raphson method is used to solve the differential equations.

The model requires the following porous medium properties: porosity, effective thermal conductivity, extinction coefficient, single scattering albedo, forward scattering fraction, and convective heat transfer coefficient. Many of the properties used are from experimental measurements; the rest are estimates.

The next chapter investigates the radiant efficiency of surface-flame burners.

2.9 REFERENCES

Bouma, P.H., Eggels, R.L.G.M., Somers, L.M.T., de Goey, L.P.H., Nieuwenhuizen, J.K., and Van Der Drift, A. (1995), "A Numerical and Experimental Study of the NO-Emission of Ceramic Foam Surface Burners", *Combustion Science and Technology* 108 (1-3), pp. 193-203.

Bowman, C.T., Hanson, R.K., Davidson, D.F., Gardiner, Jr., W.C., Lissianski, V., Smith, G.P., Golden, D.M., Frenklach, M., and Goldenberg, M. (1995), GRI-Mech 2.11, http://www.me.berkeley.edu/gri_mech/

Coltrin, M.E., Kee, R.J., Evans, G.H., Meeks, E., Rupley, F.M., and Grcar, J.F. (1991), A Fortran Program for Modeling One-Dimensional Rotating-Disk/Stagnation-Flow Chemical Vapor Deposition Reactors, Sandia National Laboratory, SAND91-8003.

Frenklach, M. (1991), "Reduction of Chemical Reaction Models", in *Numerical Approaches to Combustion Modeling* (E. S. Oran and J. P. Boris, Ed.), Progress in Astronautics and Aeronautics, Vol. 135, American Institute of Aeronautics and Astronautics, Washington, D.C., pp. 129-154.

Golombok, M., Prothero, A., Shirvill, L.C., and Small, L.M. (1991), "Surface Combustion in Metal Fibre Burners", *Combustion Science and Technology* 77, pp. 203-223.

Grcar, J.F. (1992), The Twopnt Program for Boundary Value Problems, Sandia National Laboratory, SAND91-8230.

Hendricks, T.J. and Howell, J.R. (1994a), "Absorption/Scattering Coefficients and Scattering Phase Functions in Reticulated Porous Ceramics", in *Radiative Heat Transfer: Current Research*(Y. Bayazitoglu *et al.*, Ed.), HTD-276, pp. 105-113, *AIAA/ASME Heat Transfer Conference*, Colorado Springs, June.

Howell, J.R., Hall, M.J. and Ellzey, J.L. (1995), "Combustion within Porous Inert Media", in *Heat Transfer in Porous Media and Two-Phase Flow*, (Y. Bayazitoglu and U.B. Sathuvalli, Ed.), ASME HTD-302, pp. 1-28.

Hsu, P.F. and Howell, J.R. (1993), "Measurements of Thermal Conductivity and Optical Properties of Porous Partially Stabilized Zirconia, *Experimental Heat Transfer* 5, pp. 293-313.

Kanury, A. M. (1988), *Introduction to Combustion Phenomena*, 5th ed., Gordon and Breach (New York).

Kazakov, A. and Frenklach, M. (1994), *DRM-19*, http://www.me.berkeley.edu/drm/

Kee, R.J., Dixon-Lewis, G., Warnatz, J., Coltrin, M.E., and Miller, J.A. (1986), A Fortran Computer Package for the Evaluation of Gas-Phase, Multicomponent Transport Properties, Sandia National Laboratory, SAND86-8246.

Kee, R.J., Grcar, J.F., Smooke, M.D., and Miller, J.A. (1985), A Fortran Program for Modeling Steady Laminar One-Dimensional Premixed Flames, Sandia National Laboratory, SAND85-8240.

Kee, R.J., Rupley, F.M. and Miller, J.A. (1989), CHEMKIN-II: A Fortran Chemical Kinetics Package for the Analysis of Gas Phase Chemical Kinetics, Sandia National Laboratory, SAND89-8009B.

Mantle, W.J. and Chang, W.S. (1991), "Effective Thermal Conductivity of Sintered Metal Fibers", *Journal of Thermophysics and Heat Transfer* 5(4), pp. 545-549.

Mital, R. and Gore, J.P. (1995), personal communication.

Mital, R., Gore, J.P., and Viskanta, R. (1995), "Measurements of Extinction Coefficient and Single Scattering Albedo of Reticulated Porous Ceramic at High Temperatures", AIAA Paper No. 95-2036.

Sathe, S.B., Peck, R.E., and Tong, T.W. (1990), "A Numerical Analysis of Heat Transfer and Combustion in Porous Radiant Burners," *International Journal of Heat and Mass Transfer* 33, pp. 1331-1338.

Singh, S., Ziolkowski, M., Sultzbaugh, J., and Viskanta, R. (1992), "Mathematical Model of a Ceramic Burner Radiant Heater", in *Fossil Fuel Combustion* (Roberto Ruiz, Ed.), ASME PD-33, pp. 111-116.

Viskanta, R. (1966), "Radiation Transfer and Interaction of Convection with Radiation Heat Transfer," in *Advances in Heat Transfer* (T.E. Irvine, Jr. and J.P. Hartnett, Ed.), Vol. 3, Academic Press (New York), pp. 176-252.

Viskanta, R. (1995), "Convective Heat Transfer in Consolidated Porous Materials: A Perspective", presented at the Symposium on Thermal Science and Engineering in honor of Chancellor Chang-Lin Tien, November, Berkeley, CA.

Wang, H. and Frenklach, M. (1991), "Detailed Reduction of Reaction Mechanisms for Flame Modeling", *Combustion and Flame* 87, pp. 365-370 (1991).

Williams, A., Woolley, R., and Lawes, M. (1992), "The Formation of NO_x in Surface Burners", *Combustion and Flame* 89, pp. 157-166.

Yagi, S., Kunii, D. and Wakao, N. (1960), "Studies of Axial Effective Thermal Conductivities in Packed Beds", *AIChE Journal* 6, pp. 543-546.

Younis, L.B. and Viskanta, R. (1993), "Experimental determination of the volumetric heat transfer coefficient between stream of air and ceramic foam", *International Journal Heat Mass Transfer* 36(6), pp. 1425-1434.

CHAPTER 3

Radiant Efficiency of Surface-Flame Burners

3.1 INTRODUCTION

A surface-flame burner is a porous direct-fired radiant burner in which the flame stabilizes on the surface of a porous medium (see Figure 3-1). A surface-flame burner can operate in two modes: the radiant mode (at low firing rates) in which the surface glows evenly, and the blue flame mode (at high firing rates) where part or all of the flame has lifted from the surface. The transition between modes occurs at different firing rates and equivalence ratios for different burner designs.

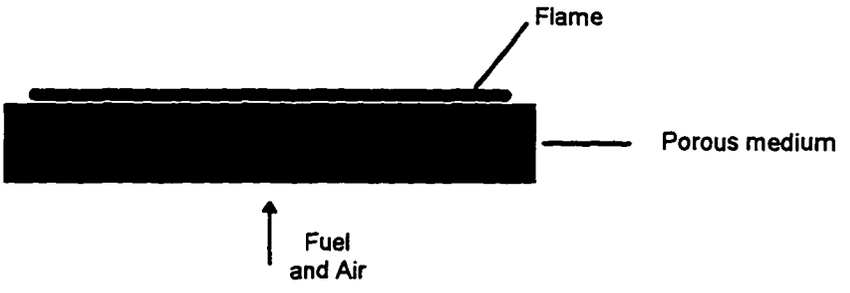

Figure 3-1: Surface-flame burner. The fuel and air flow through a porous medium and a flame stabilizes on the surface of the porous medium.

The model used in this dissertation is the most comprehensive to date and the perspective is not one of strictly heat transfer (as in many other studies), but is an interdisciplinary view from the fields of combustion *and* heat transfer. In this chapter, the radiant performance of surface-flame burners is studied. The dependence of radiant efficiency (radiant flux / chemical energy input) on equivalence ratio and firing rate is explained. Flame structure in surface-flame burners is described. The results of a parametric study of radiative performance of surface-flame burners are presented and the mechanisms that lead to variation of radiant efficiency are explained. A surface-flame burner with a bilayered porous medium is analyzed to determine the possible radiant efficiency benefits of such a burner.

3.2 MECHANISM COMPARISON

Complex chemical kinetics are necessary for accurate simulations of combustion within porous media (Hsu and Matthews, 1993). Chemical mechanisms—including the ones that we use—are generally validated by comparing the predicted laminar flame speed with measurements (among many other comparisons), which is important for surface-flame burners. Accurate chemical mechanisms are especially important because the heat source in a radiant burner is a premixed flame with a characteristic burning velocity that depends only on mixture composition, pressure, heat losses and temperature (Fristrom, 1995).

The flame adjusts itself so that the burning velocity is equal to the speed of the incoming unburned gas.

Simulation of pollutant formation, with the resultant multiple radical species and complex reaction pathways, requires a 'full' mechanism that has been constructed with accurate pollutant chemistry. For simulation of thermal performance of a burner, though, a reduced or skeletal mechanism can suffice as long as the flame speed is accurately reproduced. In this section, predictions of surface-flame burner performance using a detailed mechanism (GRI-Mech 2.11, Bowman *et al.*, 1995) and a reduced mechanism (*DRM19*, Kazakov and Frenklach, 1994) for methane combustion are compared. The detailed mechanism contains methane and nitrogen chemistry with 49 species and 279 reactions; the reduced mechanism contains 21 species and 84 reactions and was created using a detailed reduction technique (Frenklach, 1991; Wang and Frenklach, 1991). We are interested in using the smaller mechanism primarily for reasons of convenience and efficiency: smaller mechanisms run faster and allow better grid resolution (i.e. more grid points), and thus permit more simulations.

Figure 3-2 shows radiant efficiency predictions using the full and reduced mechanisms for a surface-flame burner at two equivalence ratios. A nearly constant offset between the reduced mechanism (dashed line) and the detailed mechanism (solid line) occurs across a wide range of conditions. Typical

deviations are on the order of 4% at low firing rates but over 10% at high firing rates. This behavior is acceptable because at high firing rates the burners enter blue flame mode, which is not of strong interest to us. Deviation between the mechanisms is a result of differences in flame speed prediction.

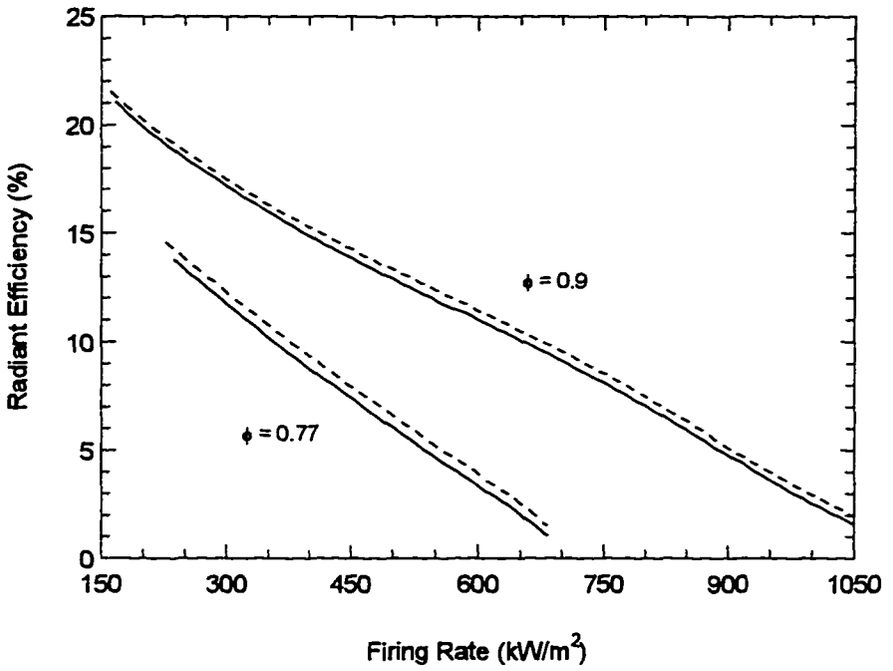

Figure 3-2: Radiant efficiency as firing rate varies for the full (solid lines) and reduced (dashed lines) mechanisms. The equivalence ratio is 0.77 (lower curves) and 0.9 (upper curves).

Predictions for exit gas temperature (15 cm downstream of the porous medium) and porous medium surface temperature are shown in Figure 3-3 for two equivalence ratios. Deviations between gas temperature predictions are under 20 K at all conditions (<1 %); surface temperature deviations are less than 50 K (5%) at each firing rate.

The UNIX "time" command was used to demonstrate the differences in computational speed between *DRM19* and GRI-Mech 2.11. A $\phi = 0.9$ flame on a surface-flame burner was simulated for ten different firing rates with each mechanism. The reduced mechanism simulation required only 20% as long as the detailed mechanism simulation.

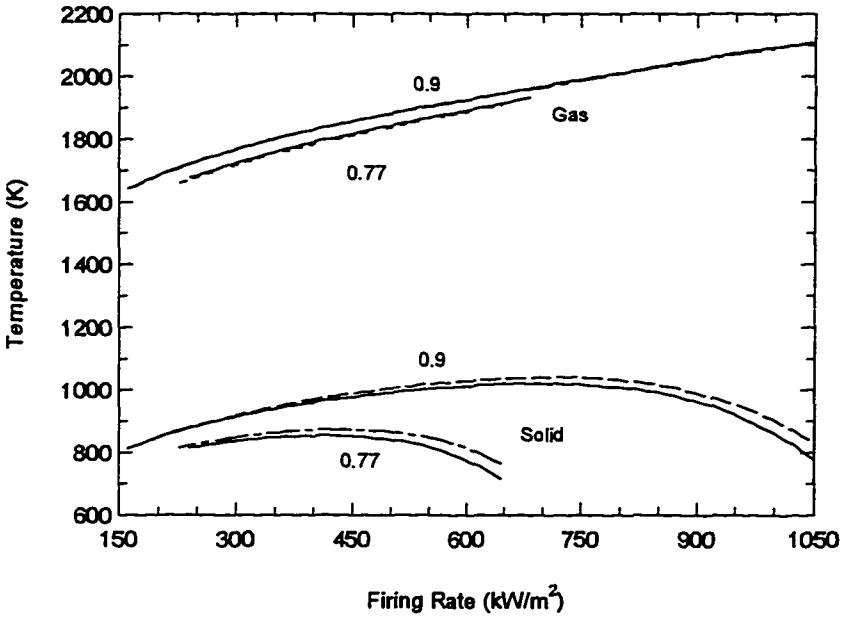

Figure 3-3: Maximum gas temperature and surface temperature for full (solid) and reduced (dashed) mechanisms. The numbers refer to the equivalence ratio (0.9 and 0.77).

3.3 COMPARISON WITH EXPERIMENTAL DATA

In this section, model predictions for gas temperature and radiant efficiency are compared with published measurements from a paper by Williams *et al.* (1992). Williams *et al.* (1992) used a Pyrocore® burner (Alzeta Corporation, Santa Clara, CA) that had a cylindrical-shaped porous medium with an outside diameter of 4

cm and a length of 10 cm. The porous medium was a matrix of ceramic fibers that was approximately 0.4 cm thick. They measured gas temperature, radiant efficiency, surface temperature, major species profiles and NO_x profiles.

The following reasonable estimates were used to represent a ceramic fiber porous medium: extinction coefficient of 1000 m^{-1}, burner thickness of 4 mm, scattering albedo of 0.7, forward scattering fraction of 0.65, porosity of 0.8, effective thermal conductivity 0.05 W/m-K, and a convective heat transfer coefficient correlation from Andersen (1991) with $f_h = 120$.

Gas temperature was measured by Williams *et al.* (1992) with a CARS technique using N_2 spectra. The accuracy was estimated to be ± 30 K with a reproducibility of ± 20 K. Figure 3-4 shows the measurements and predictions for a firing rate of 366 kW/m^2 and four equivalence ratios (ϕ = 0.77, 0.83, 0.91, and 1.0). Agreement is quite good, with the deviation increasing at farther distances from the burner surface, which is a result of radiative cooling of the combustion gases. The numerical model does not include losses through gas radiation above the burner.

Figure 3-5 shows the measurements and predictions for two firing rates at ϕ = 1.0. Again, agreement is good. The deviation increases at distances downstream of the burner surface, due to gas radiation.

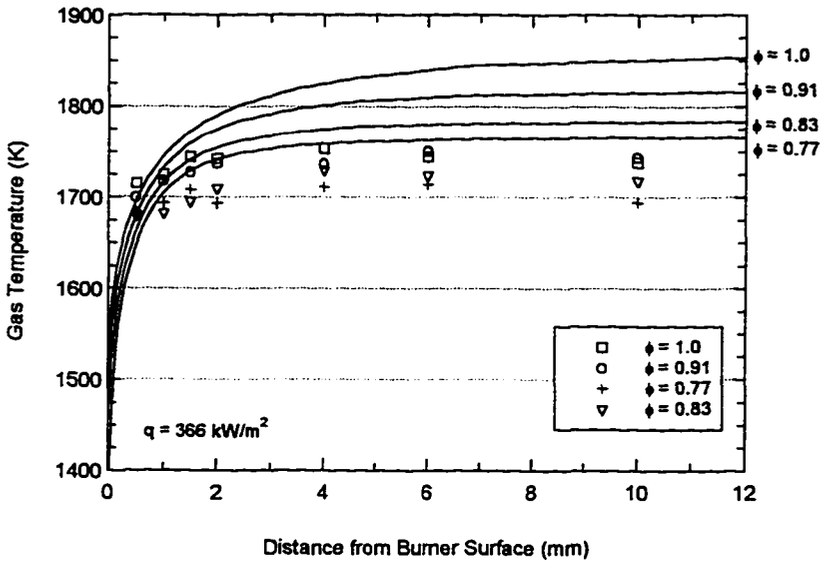

Figure 3-4: Comparison of gas temperature measurements (points) with predictions (lines) for a firing rate of 366 kW/m² and four equivalence ratios. The burner is a cylindrical-shaped burner with a ceramic fiber porous medium (Pyrocore®, Alzeta Corp.). The stated accuracy of the temperature measurements is ±30 K. Data from Williams *et al.* (1992).

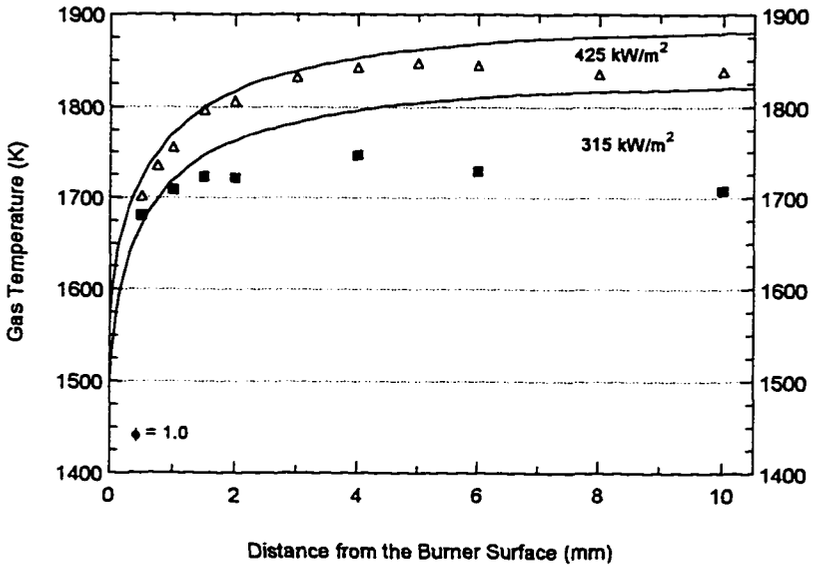

Figure 3-5: Comparison of gas temperature measurements (points) with predictions (lines) for ϕ = 1.0 and two firing rates. The stated accuracy of the temperature measurements is ±30 K. Data from Williams *et al.* (1992).

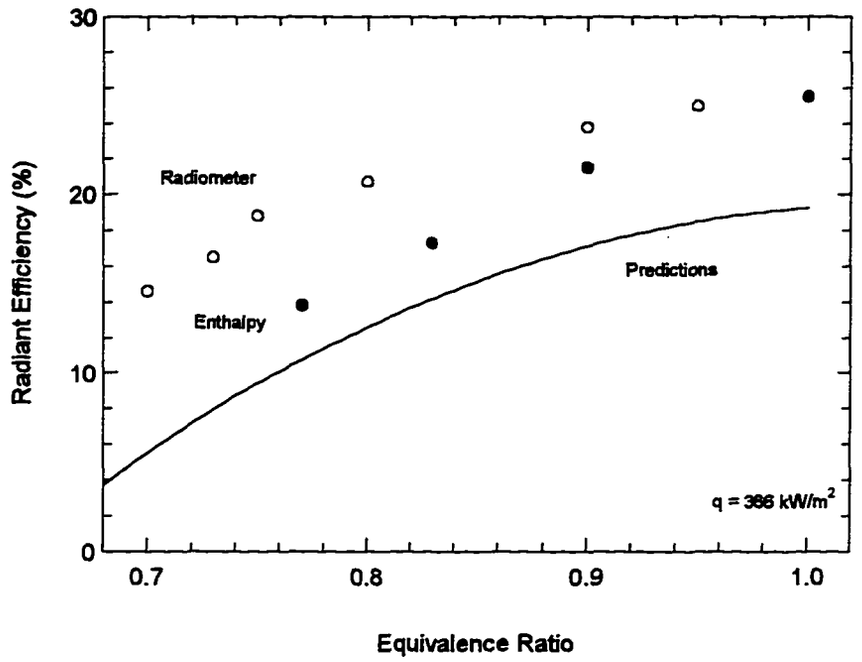

Figure 3-6: Comparison of radiant efficiency measurements (points) with predictions (lines) for q = 366 kW/m² and various equivalence ratios. The filled circles (●) represent radiant efficiency based on the enthalpy of the burned gas, the open circles (○) are the direct radiation measurement. Data from Williams *et al.* (1992).

Figure 3-6 shows radiant efficiency predictions and measurements for the cylindrical burner used in Williams *et al.* (1992). Radiation measurements were made with a Land total radiation pyrometer. A radiant efficiency based on the enthalpy of the burned gas was also calculated by Williams *et al.* (1992).

The model underpredicts the radiant efficiency but clearly matches the trend. Measurement of radiant efficiency is difficult and involves large uncertainty, such as the view factor between the pyrometer and burner, and directional radiation emission by the burner. The radiant efficiency reported by Williams *et al.* (1992) is significantly higher than other reported measurements

for ceramic fiber burners, such as Sullivan and Kendall (1992) and Schweizer and Sullivan (1994), who report significantly lower efficiencies for a planar ceramic fiber burner. Although the burner geometries (cylindrical vs. planar) and porous medium thicknesses (4 mm vs. 10 mm) are different, these burner differences should not result in large differences in radiant efficiency.

Compared with the radiant efficiency based on burned-gas enthalpy, the model prediction is too low. The experiment had heat loss from gas radiation, which decreases the gas temperature downstream of the burner, thus increasing the radiant efficiency in the measurement. Furthermore, in the model the temperature of the gas is slowly increasing downstream of the burner, which increases the deviation between model and experiment. Thus, overprediction of gas temperature leads to underprediction of radiant efficiency. Nonetheless, the model performs acceptably given the uncertainty associated with radiant efficiency measurements and the difference between model and experiment.

3.4 BURNER OPERATION AND PREMIXED FLAME STABILIZATION

Calculations and measurements showing that radiant efficiency decreases as firing rate increases in direct-fired radiant burners have been presented several times (Khanna *et al.*, 1994; Mital *et al.*, 1995; Kulkarni, 1996). However, the reason for this behavior has not yet been clearly explained. Here we offer an interpretation of the dependence of radiant efficiency on firing rate (seen in Figure 3-2) and then present numerical results that support the assertion.

A mixture of fuel and air has a fundamental adiabatic flame speed, S_L, that depends only on mixture composition, pressure, initial temperature and heat losses (Fristrom, 1995). The unburned gas flows at a velocity of V through the porous medium. As the firing rate decreases, the velocity of the unburned gas decreases but the adiabatic flame speed of the mixture remains constant. Thus, when V is less than S_L the flame loses heat to the porous medium to reduce the flame speed to V. As the firing rate decreases, the flame loses more heat in order to lower the flame speed to V. Most of this heat lost by the gas is radiated away by the burner. The same dependence of heat loss on firing rate has been shown for premixed flames stabilized on a cooled porous plug (van Maaren *et al.*, 1994), in which the heat lost by the gas is transferred to cooling water in the porous plug. Figure 3-7 shows the variation of heat loss with firing rate for a water-cooled burner and a surface-flame burner (called a "radiation-cooled burner" for the remainder of this section). Radiation from the gas—which is not considered in the model—is a primary reason for the differences in heat loss between the model and experiment in Figure 3-7. Additionally, the experimental burner might have had some heat loss to the burner that was not captured by the cooling water. In summary, as the firing rate decreases, a larger percentage of the chemical heat must be lost for the flame to stabilize upon the burner, thus radiant efficiency increases.

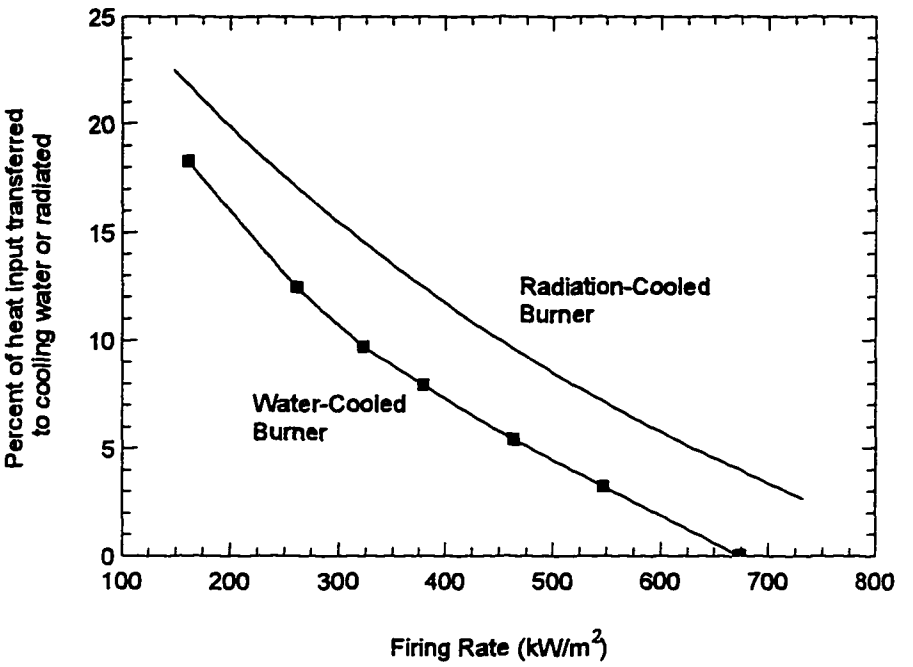

Figure 3-7: Heat loss from a premixed flame as firing rate varies. Water-cooled burner data adapted from van Maaren *et al.* (1994). The equivalence ratio is 0.8.

3.5 FLAME STRUCTURE IN SURFACE-FLAME BURNERS

The investigation of flame structure in surface-flame burners can illustrate basic features of burner operation. Calculations were performed for methane-air flames for two conditions at $\phi = 0.9$: a low firing rate (150 kW/m^2) and a high firing rate (600 kW/m^2). The low firing rate corresponds to a burner operating in full radiant mode, while the high firing rate corresponds to a burner that is operating near the blue-flame mode (perhaps with slight flame detachment). The porous medium has the following properties: extinction coefficient of 1000 m^{-1}, thickness of 5 mm, scattering albedo of 0.7, forward scattering fraction of 0.65, porosity of 0.8, effective thermal conductivity for the porous medium

based on a bulk conductivity of 1.0 W/m-K, and a 22-micron fiber diameter. The initial gas temperature for all simulations is 300 K, unless otherwise noted.

Figure 3-8 shows the gas and solid temperatures for each firing rate. The vertical dashed lines are the boundaries of the porous medium. Flow is from left to right. The temperature of the exhaust increases as firing rate increases. In this case the temperature difference is nearly 300 K, which has profound impact on the NO_x emission, as we shall see in Chapter 4. The upstream portion of the porous medium is cooler at the higher flow rate because the convective heat transfer coefficient rises with increasing gas velocity. Recall that the flame is not fixed, but instead can move as circumstances dictate.

Figure 3-9 shows the net radiant flux in the porous medium for two firing rates. In most of the porous medium, the net radiant flux is in the upstream direction, a very important characteristic that will be explored further in this chapter. Near the downstream edge the net radiant flux becomes positive and rises sharply to reach the boundary value.

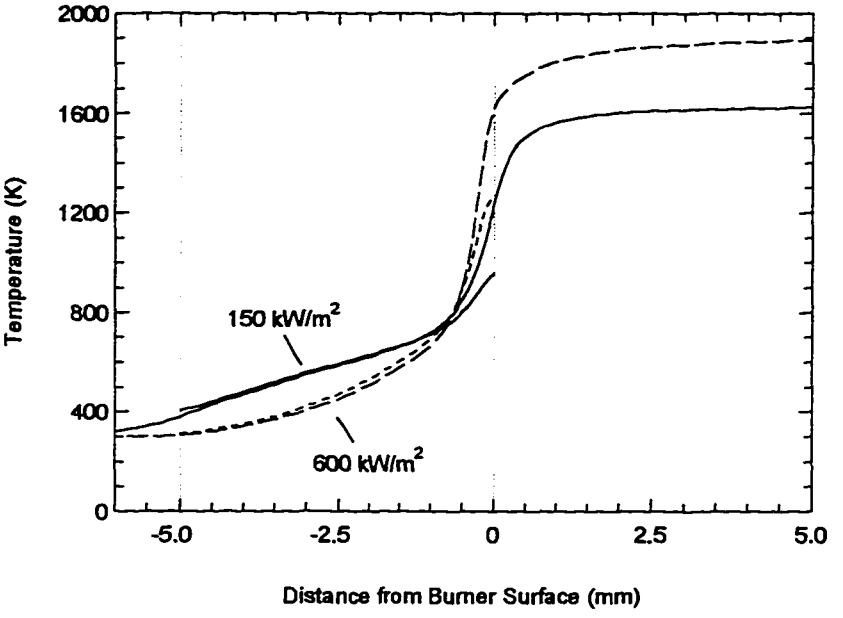

Figure 3-8: Gas and solid temperature for a $\phi = 0.9$ flame at two firing rates, 150 kW/m² (solid lines) and 600 kW/m² (dashed lines). The vertical dashed lines mark the boundaries of the porous medium. The solid temperature curves span the region between the vertical dashed lines.

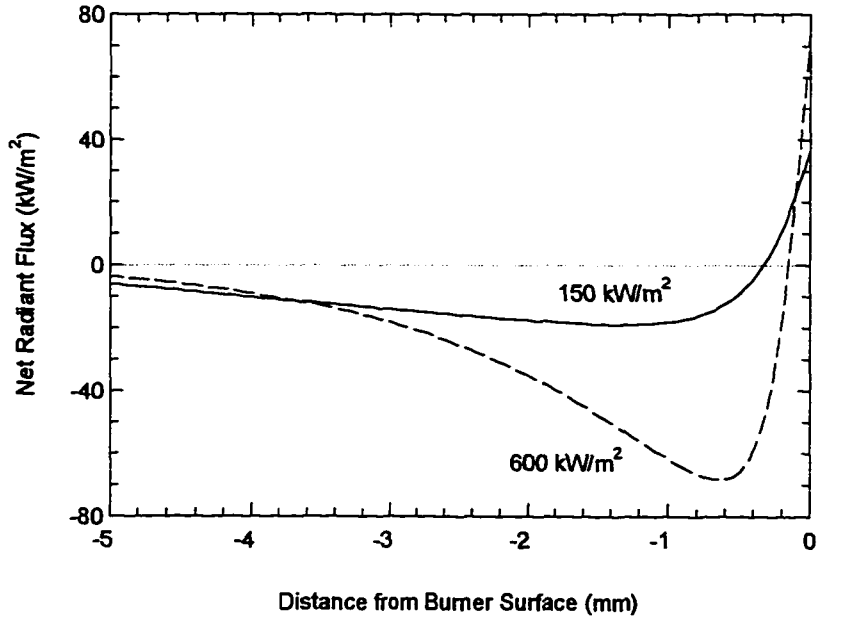

Figure 3-9: Net radiant flux in the porous medium of a radiant burner at $\phi = 0.9$ for two firing rates (in kW/m²).

Figure 3-10 shows the mole fractions of the major species at 150 kW/m^2. The vertical dashed lines mark the location of the porous medium. The bulk of the methane decomposition occurs within the porous medium and much of the CO_2 formation occurs outside the porous medium. The peaks of major radicals (O, OH, and H) are found in the gas-only region just downstream of the porous medium (see Figure 3-11).

Figure 3-12 shows the major species for the high firing rate; Figure 3-13 shows the major radical profiles. The profiles have moved upstream slightly and the radical peaks are nearly inside the porous medium.

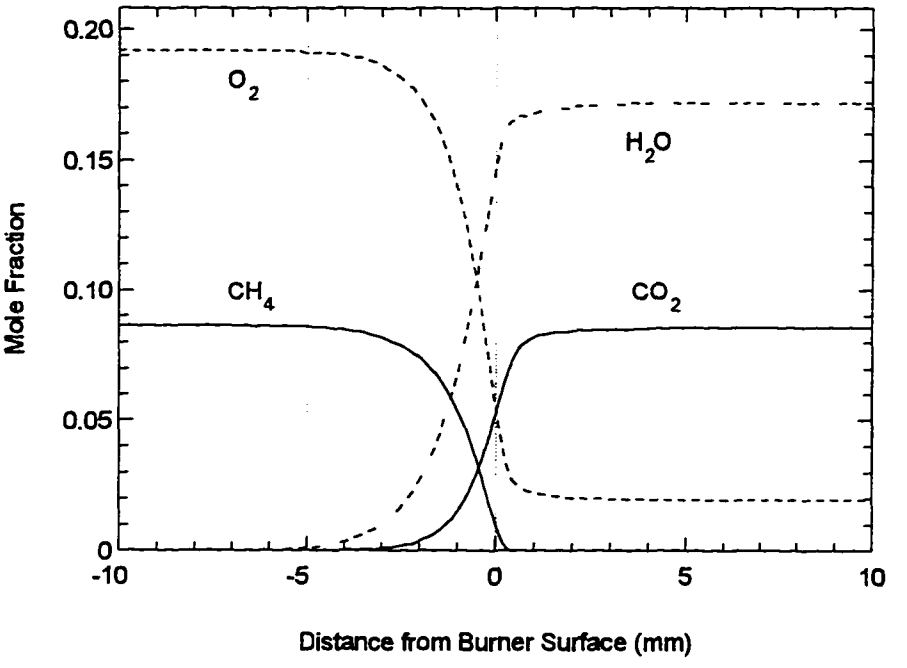

Figure 3-10: Major species concentrations in a surface-flame burner operated at 150 kW/m^2 and $\phi = 0.9$.

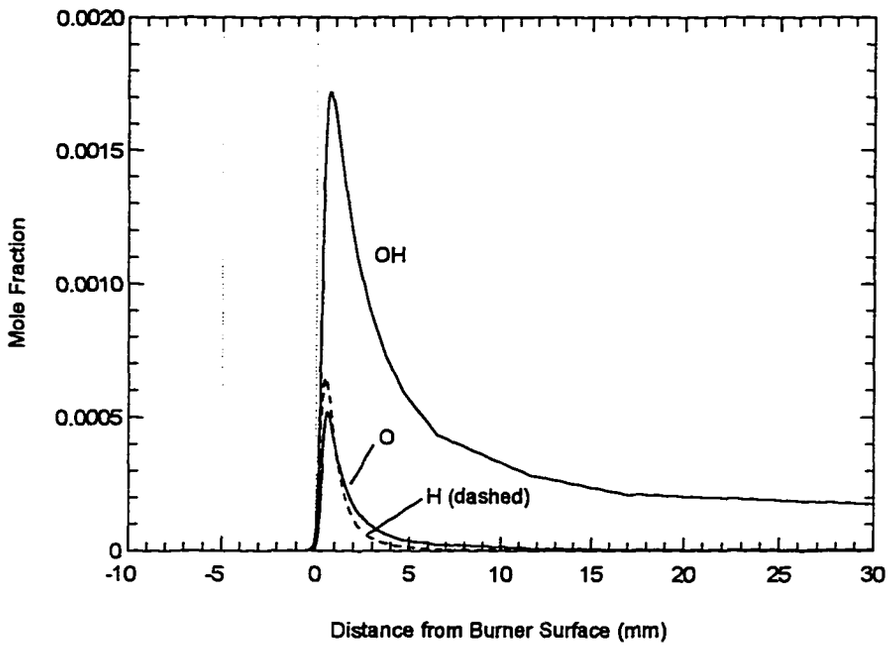

Figure 3-11: Major radical concentrations in a surface-flame burner operated at 150 kW/m² and $\phi = 0.9$.

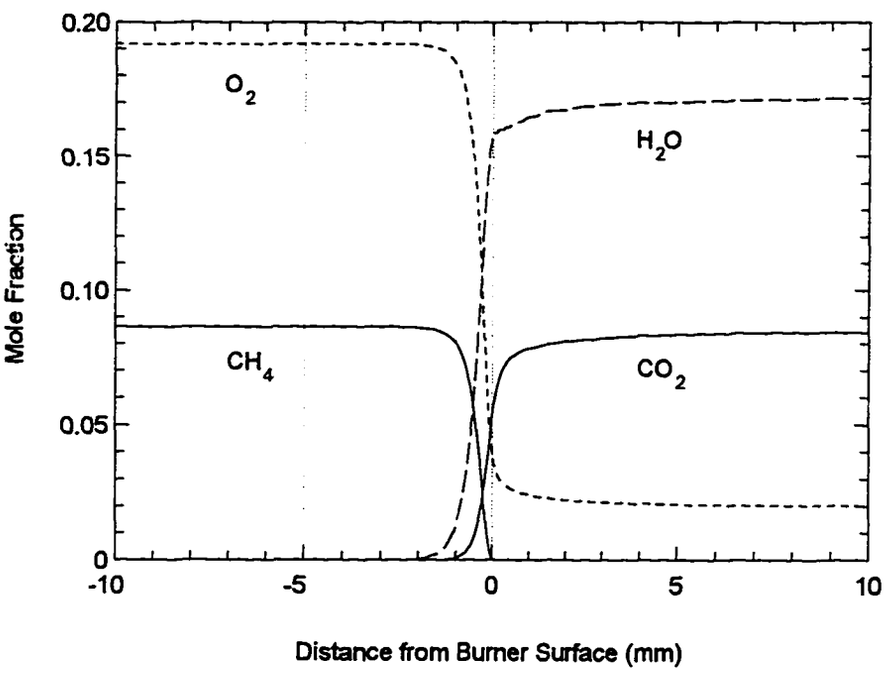

Figure 3-12: Major species concentrations in a surface-flame burner operated at 600 kW/m² and $\phi = 0.9$.

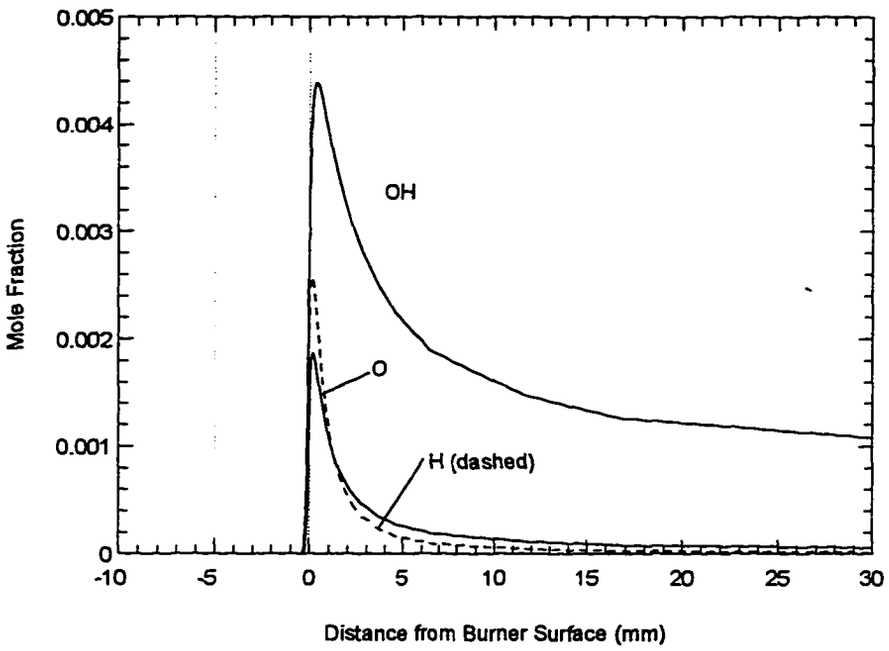

Figure 3-13: Major radical concentrations in a surface-flame burner operated at 600 kW/m² and $\phi = 0.9$.

Figure 3-14 shows the chemical heat release for the two flow conditions. The chemical heat release rate $\dot{q}$ (W/cm³) is calculated as

$$\dot{q} = \sum_k W_k \dot{\omega}_k h_k \qquad [3\text{-}1]$$

where $\dot{w}_k$ is the reaction rate of the k-th species (mol/cm³-s), W_k is the molecular mass of the k-th species (g/mol), and h_k is the enthalpy of the k-th species (J/g). The relative location of the two curves shows that the flame moves upstream as the firing rate increases from 150 to 600 kW/m². At a low firing rate, the flame is relatively far from the burner surface—even though the flow velocity is low—to prevent the heat release from being overcome by heat losses. As the firing rate increases, the heat release increases, which allows more heat transfer to the

porous medium. Some of the heat propagates upstream in the porous medium and preheats the gas, which increases the laminar flame speed, allowing the flame to move upstream into the burner. Eventually, though, the convective velocity pushes the flame away from the burner (Viskanta, 1995). This behavior has been described in numerical studies (Kulkarni and Peck, 1993), and was also briefly experimentally examined by Williams *et al.* (1992). However, the experiment of Williams *et al.* (1992) was not conclusive because of the difficulty of gas temperature measurements very close to the porous medium (< 1 mm).

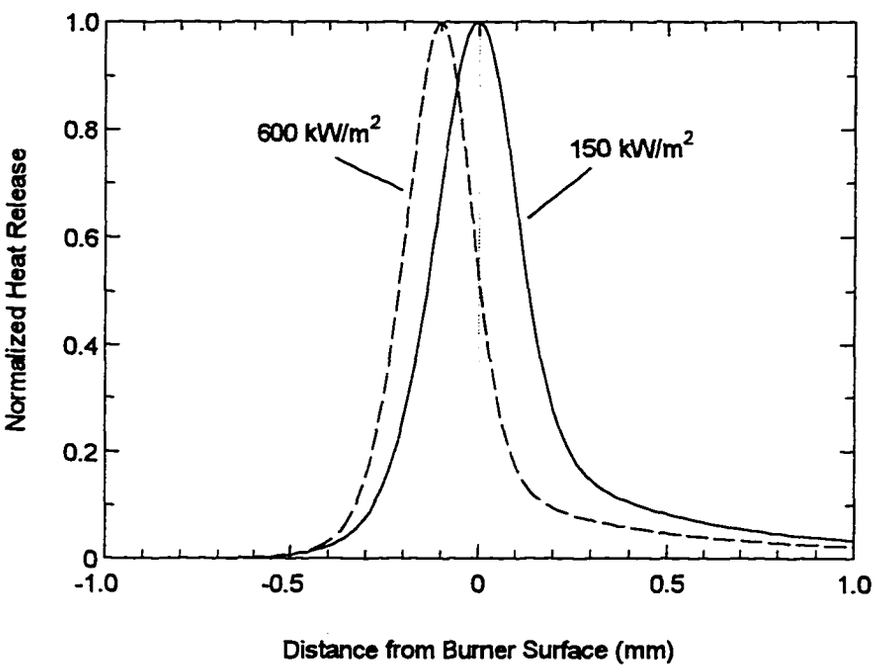

Figure 3-14: Normalized heat release profiles for two firing rates at $\phi = 0.9$, calculated using Eq. [3-1] from Section 3.5.

3.6 PARAMETRIC STUDY OF SURFACE-FLAME BURNER RADIANT EFFICIENCY

The porous media used in radiant burners have many properties that can affect performance. These include radiative properties like single scattering albedo, extinction coefficient and forward scattering fraction; thermal properties like effective thermal conductivity and convection coefficient; and physical properties like pore diameter, fiber diameter, porous medium thickness, and porosity. Creating a test matrix to study many of the possible combinations would be daunting and performance of the experiments would be a lengthy and expensive procedure. With the numerical model, though, one can vary the properties and quickly learn how the burner might behave and identify promising configurations for experiment.

A numerical parametric study was performed to determine how burner properties affect the radiant efficiency of a surface-flame burner. Six parameters were independently varied: extinction coefficient, burner thickness, forward scattering fraction, single scattering albedo, porosity, and effective thermal conductivity. The "base" burner properties were chosen to represent an average fiber burner: extinction coefficient of 1000 m^{-1}, burner thickness of 5 mm, scattering albedo of 0.7, forward scattering fraction of 0.65, porosity of 0.8, effective thermal conductivity that corresponds to bulk conductivity of 1.0 W/m-K (using the correlation from Mantle and Chang (1991) with a 22-μm

fiber diameter). In all simulations in this section, the porous medium is a single layer with constant properties throughout (except for the convection coefficient, which depends on gas temperature and composition).

At $\phi = 0.9$ (11% excess air), two firing rates in the radiant mode (150 and 300 kW/m^2) and one firing rate near the blue flame mode (600 kW/m^2) were considered. The upper limit of 600 kW/m^2 was chosen because above that firing rate it would be unlikely to find a real burner that does not have partial flame lift-off. At $\phi = 0.77$ (30% excess air), two firing rates in the radiant mode were considered (150 and 300 kW/m^2). The variation of radiant efficiency with firing rate and equivalence ratio was presented in Figure 3-2. A similar but less comprehensive study was performed by Kulkarni (1996), but the flame position was fixed in his model and he only offered a brief explanation of the underlying reasons behind surface-flame burner radiant efficiency. The results presented below are for a burner with a moving flame and are presented in such a way that the effect of each property on burner performance is clear. Additional analysis of heat transfer and heat propagation is included to conclusively define how burner properties affect radiant efficiency (in Section 3.7 below).

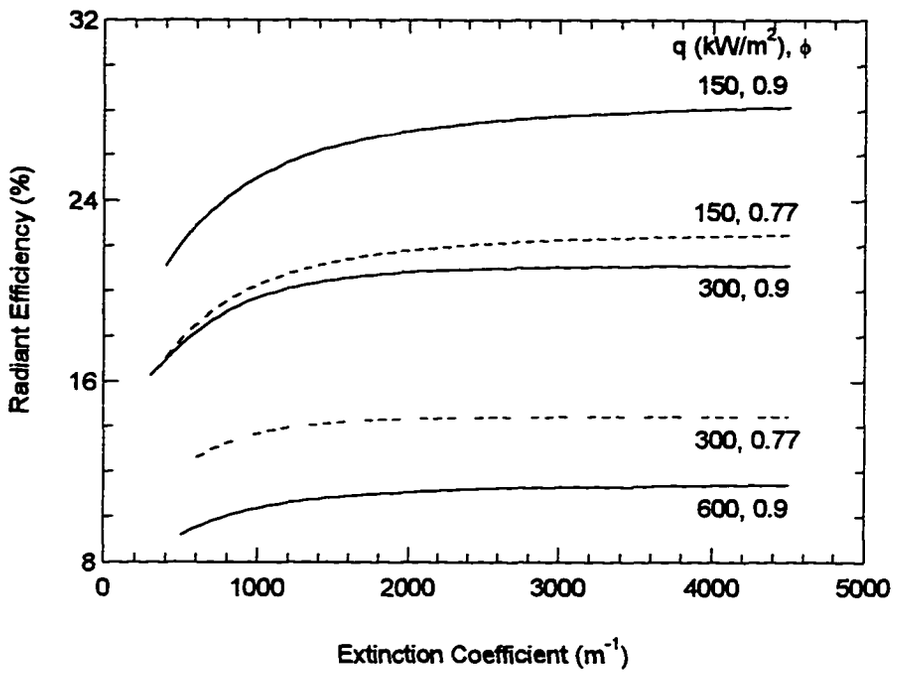

Figure 3-15: Variation of radiant efficiency with extinction coefficient for several conditions. The first number near each curve refers to the firing rate in kW/m² and the second refers to the equivalence ratio. Solid lines are for ϕ = 0.9 (11% excess air); dashed lines are for ϕ = 0.77 (30% excess air).

Figure 3-15 shows the variation of radiant efficiency with extinction coefficient. As the burner becomes optically denser, the radiant efficiency increases quickly then levels off. At low values of extinction coefficient more radiant heat passes through the porous medium and escapes. Solutions were not found for the 600 kW/m² firing rate for extinction coefficient below 400 m^{-1}, presumably because flash back occurred. Numerical non-convergence at low extinction coefficients has been observed by other authors, notably Kulkarni (1996). Note that the lower limit for convergence also depends on the other properties of the burner.

Behavior similar to that seen in Figure 3-15 occurs when burner length is varied (see Figure 3-16). When the burner is thin, some of the heat propagates completely through the burner and escapes from the upstream edge, thus reducing the radiant efficiency. As the thickness increases, the amount of heat that can pass entirely through the burner decreases. The burner thickness where the radiant efficiency is nearly the maximum value shifts to shorter distances as firing rate increases. This occurs because the convective heat transfer coefficient increases with increasing flow rate.

Although the optical depth (the product of extinction coefficient and length = $\sigma_e L$) is a traditional dimensionless parameter used in radiative heat transfer in participating media, the multi-mode heat transfer prevents Figure 3-15 and Figure 3-16 from being condensed into one figure because *all three* heat transfer modes depend on burner thickness: length for extinction of thermal radiation, surface area for convective heat transfer, and the temperature gradient for conduction.

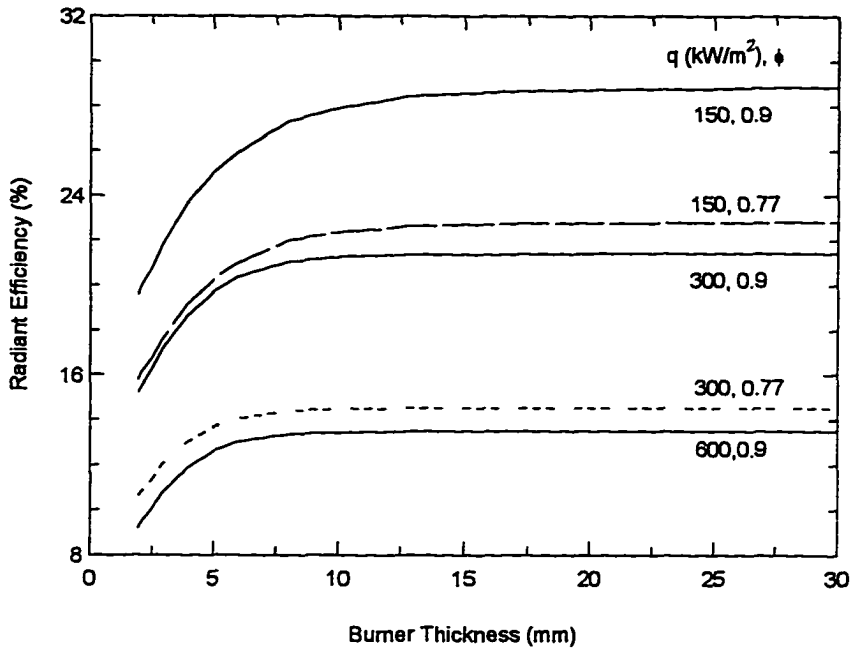

Figure 3-16: Variation of radiant efficiency with burner thickness for several conditions. Solid lines are for $\phi = 0.9$, dashed lines are for $\phi = 0.77$.

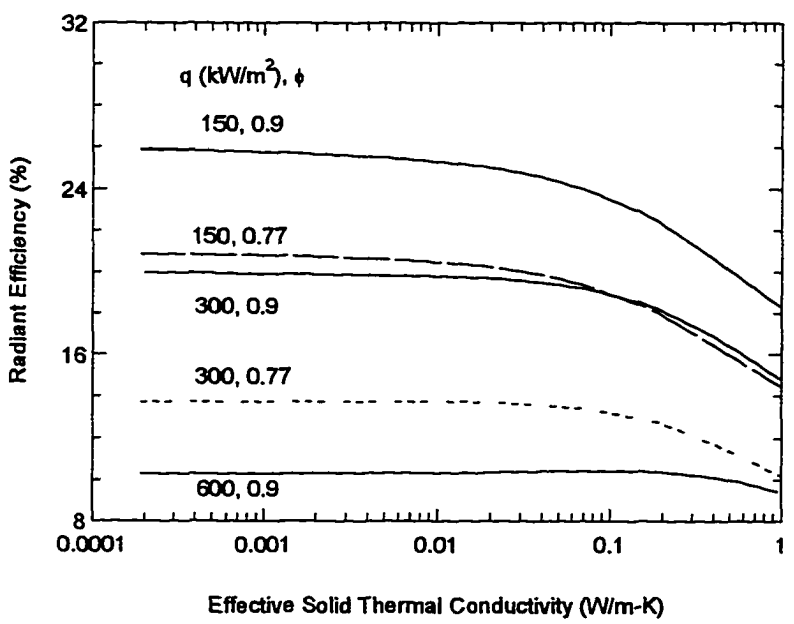

Figure 3-17: Variation of radiant efficiency with effective thermal conductivity for several conditions. Solid lines are for $\phi = 0.9$; dashed lines are for $\phi = 0.77$. Note the log scale on the x-axis.

The influence of effective solid thermal conductivity ($k_{s,e}$) is displayed in Figure 3-17. The radiant efficiency declines as $k_{s,e}$ increases because heat conducts upstream and radiates out of the upstream edge at higher rates when $k_{s,e}$ is large. The shape of the radiant efficiency curves also depend on other burner parameters, such as burner thickness and extinction coefficient. For example, the decline in radiant efficiency would not be as steep for a thicker (than 5 mm) porous medium and would be steeper for a thinner porous medium.

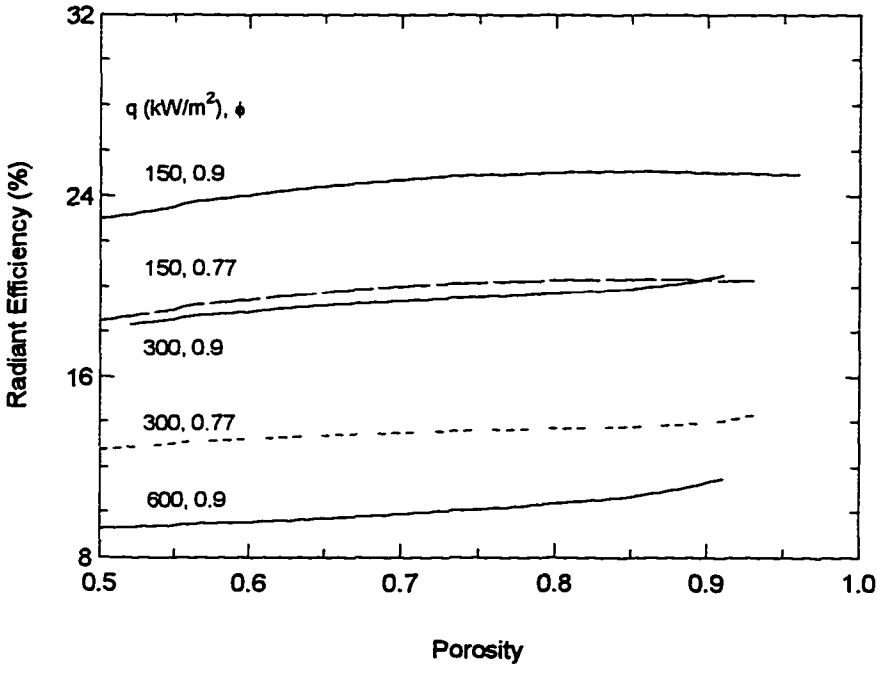

Figure 3-18: Variation of radiant efficiency with porosity for several conditions. Solid lines are for ϕ = 0.9; dashed lines are for ϕ = 0.77.

Figure 3-18 shows the effect of porosity on radiant efficiency. A slight increase in radiant efficiency occurs as the porosity increases because the heat

transfer coefficient decreases, allowing more heat transfer between the flame and porous medium. Note that porosity affects the convective heat transfer coefficient (inversely) and the effective thermal conductivity (inversely). Solutions could not be found for very high porosities, presumably because the flame moved through the burner and flashed back, which is similar to behavior at low extinction coefficient and high firing rate.

Several of the burner properties studied have little impact on radiant efficiency. At lower firing rates and equivalence ratios, an increase in scattering albedo decreases radiant efficiency slightly. If less radiant energy is absorbed by the porous medium (high albedo), more can escape through the upstream edge. Increasing the forward scattering fraction will slightly decrease the radiant efficiency. This occurs because in the upstream half of the porous medium, the net radiant flux is in the backward direction (recall Figure 3-9) and forward scattering increases the amount of heat that escapes.

The importance of the convective heat transfer coefficient for radiant efficiency was investigated by simulating radiant burner operation with four different convective heat transfer coefficient correlations:

1. the Golombok *et al.* (1991) correlation (Eq. [2-16] and [2-17] in Chapter 2), $Nu = a\ Re^b$;
2. a correlation from Andersen (1991) (Eq. [2-18] in Chapter 2, with f_k = 12);
3. a constant h_v of 10^7 W/m^3-K;
4. a constant h_v of 10^8 W/m^3-K.

The Andersen (1991) correlation gave the lowest convective heat transfer coefficients; the constant h_v of 10^8 W/m^3-K was the highest. Figure 3-19 shows that the convective heat transfer coefficient has little impact on radiant efficiency. However, we find that the convective heat transfer coefficient is important for flame stability; if h_v is too low, the flame can flash back at high firing rates.

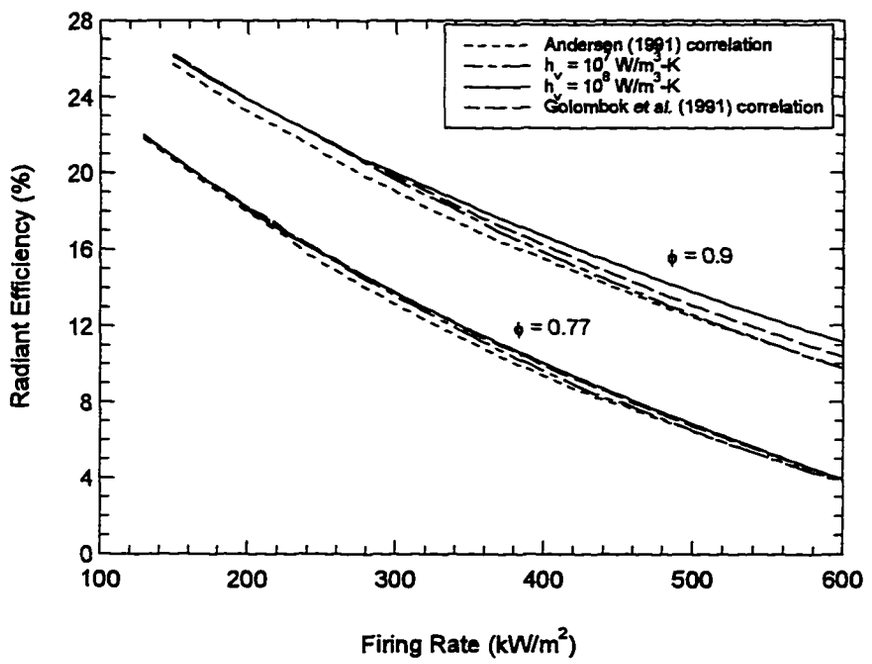

Figure 3-19: Variation of radiant efficiency for several different convective heat transfer coefficient correlations.

In order to investigate the range of efficiencies possible in surface-flame burners, a set of porous medium properties was chosen to give an "optimized" burner (with high radiant efficiency) and a "de-optimized" burner (with low radiant efficiency). Figure 3-20 shows the radiant efficiency for the optimized burner and the de-optimized burner. The optimized burner had the following

properties: extinction coefficient of 4000 m^{-1}; thickness of 10 mm; scattering albedo of 0.7; forward scattering fraction of 0.8; porosity of 0.85; effective thermal conductivity that corresponds to bulk conductivity of 1.0 W/m-K. The de-optimized burner had the following properties: extinction coefficient of 400 m^{-1}; thickness of 2 mm; scattering albedo of 0.4; forward scattering fraction of 0.4; porosity of 0.5; effective thermal conductivity that corresponds to bulk conductivity of 75.0 W/m-K. Note that the radiant efficiency gains are not strictly additive, that is, while independently doubling the extinction coefficient or thickness would increase the radiant efficiency by Y percent for each change, doubling both will not improve radiant efficiency by $2Y$ percent. This is because the radiant efficiency gains are primarily caused by 'radiation containment'. A thicker, less conductive, or optically denser burner can each serve the purpose of preventing radiant energy from penetrating to the upstream edge. The curves in Figure 3-20 can be viewed as bounds for the performance of a surface-flame burner made with a porous medium that is a homogenous single layer.

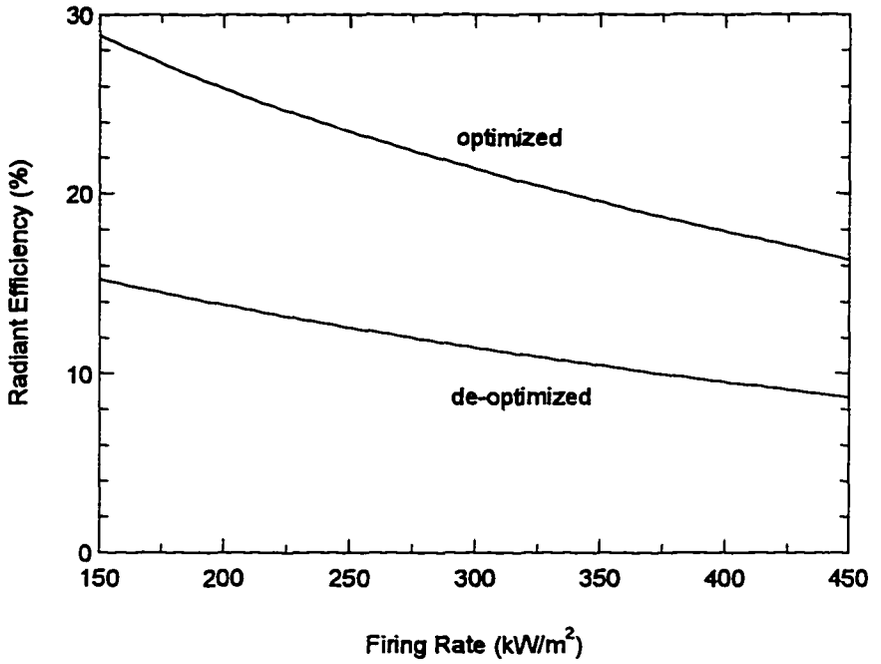

Figure 3-20: Radiant efficiency for optimized and de-optimized surface-flame burners. $\phi = 0.9$.

3.7 MECHANISMS OF RADIANT EFFICIENCY VARIATION

This section will demonstrate that the dominant factor for radiant efficiency variation between different surface-flame burner designs is heat redirection. This is done by analyzing the heat transfer from the gas to the solid for many different burner designs and flow conditions.

Figure 3-21 shows the normalized net heat transfer from the gas to the solid (the "normalized heat transfer") for three firing rates at $\phi = 0.9$. The curves are normalized to allow presentation of all firing rates on one figure; the maximum net heat transfer is different for each firing rate. Figure 3-21 shows that as the extinction coefficient changes, the normalized heat transfer is nearly

constant for the firing rate of 150 kW/m^2. Normalized heat transfer varies less than 10% for 300 and 600 kW/m^2. At the highest firing rate, the flame is less sensitive to quenching and can have more contact with the burner, thus transferring more heat. Recall from Figure 3-15 that the radiant efficiency changed by more than 20% over the range of extinction coefficients for 150 kW/m^2 and 300 kW/m^2. Although the heat transfer remains nearly constant, the radiant efficiency changes.

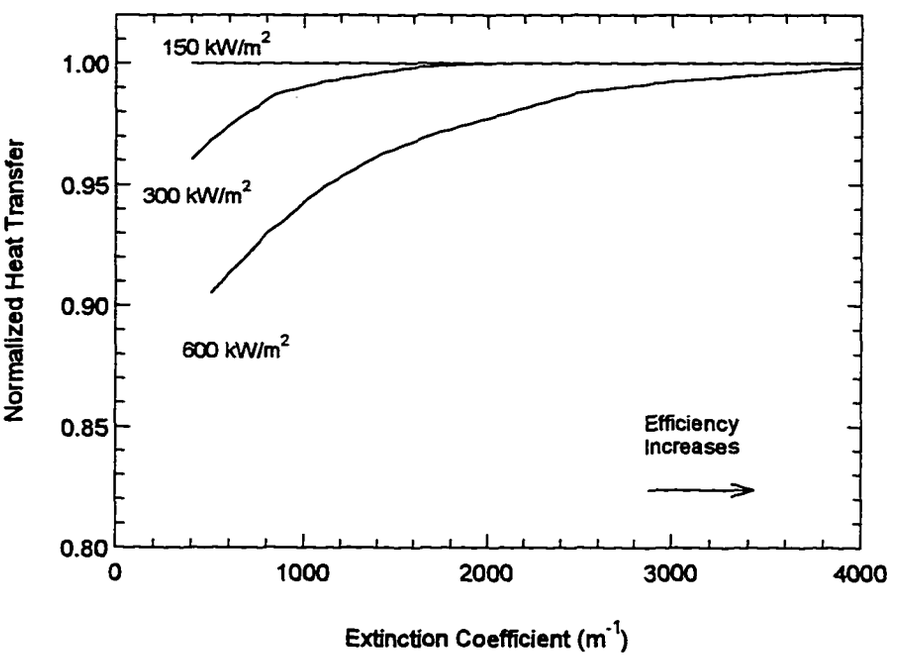

Figure 3-21: Normalized heat transfer from the flame as a function of extinction coefficient at ϕ = 0.9. The numbers near the curves refer to the firing rate.

Figure 3-22 explains the apparent contradiction between heat transfer and radiant efficiency at low firing rates by showing the fraction of the heat transferred from the gas to the porous medium that is converted into useful (i.e.

forward) radiation. Even though the heat transfer at 150 kW/m^2 is nearly constant, the amount of heat that exits the forward face of the burner increases with increasing extinction coefficient. Figure 3-23 offers another view of this situation by displaying the net heat flux in the porous medium for three burners with different extinction coefficients operating at $\phi = 0.9$ and 150 kW/m^2. As the extinction coefficient increases, the curve shifts upward, which decreases the backward heat flux and increases the forward heat flux.

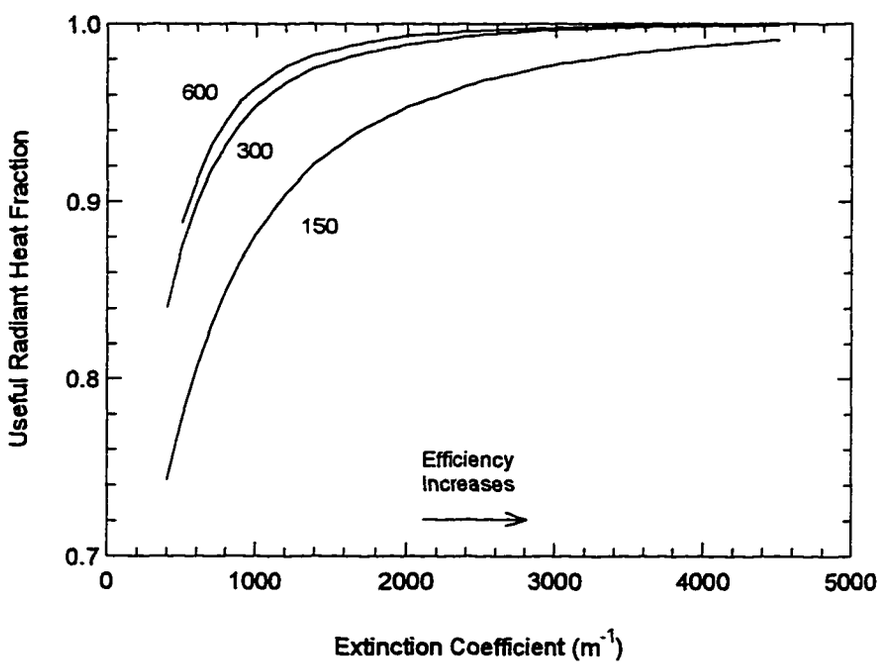

Figure 3-22: The fraction of heat transferred from the gas to solid that is converted to useful (forward) radiation as extinction coefficient varies for several firing rates (in kW/m^2) at $\phi = 0.9$.

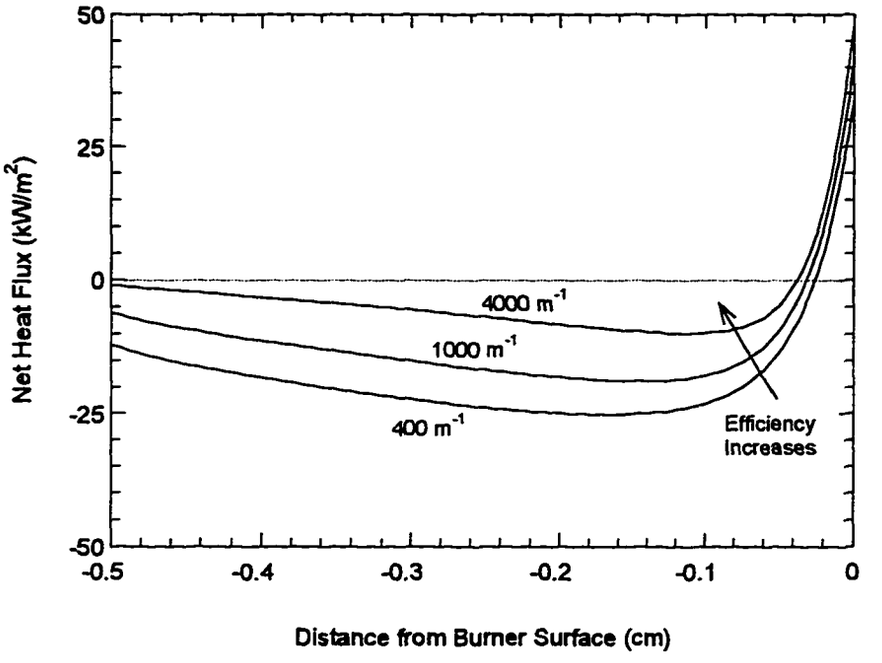

Figure 3-23: Net heat flux in the porous medium at 150 kW/m² and ϕ = 0.9 for three values of extinction coefficient. The numbers near the curve refer to the extinction coefficient of the porous medium.

Further evidence of the heat transfer redirection is seen in the next few figures. Figure 3-24 shows the normalized heat transfer for a ϕ = 0.9 flame at three firing rates as effective thermal conductivity is varied. The change is miniscule at 150 and 300 kW/m² and also small at 600 kW/m² (under 10%). Recall that the radiant efficiency varied by over 20% for each firing rate (Figure 3-17). Figure 3-25 and Figure 3-26 explain why the radiant efficiency changes: as effective thermal conductivity decreases, less heat is able to propagate to the upstream edge of the burner.

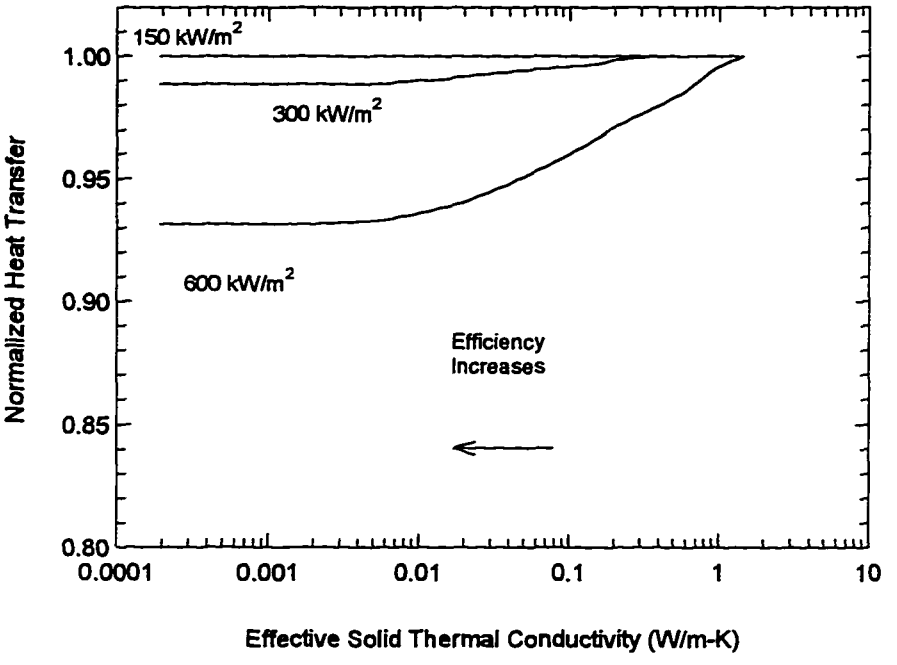

Figure 3-24: Normalized heat transfer for thermal conductivity variation for three firing rates at $\phi = 0.9$. The numbers refer to firing rate.

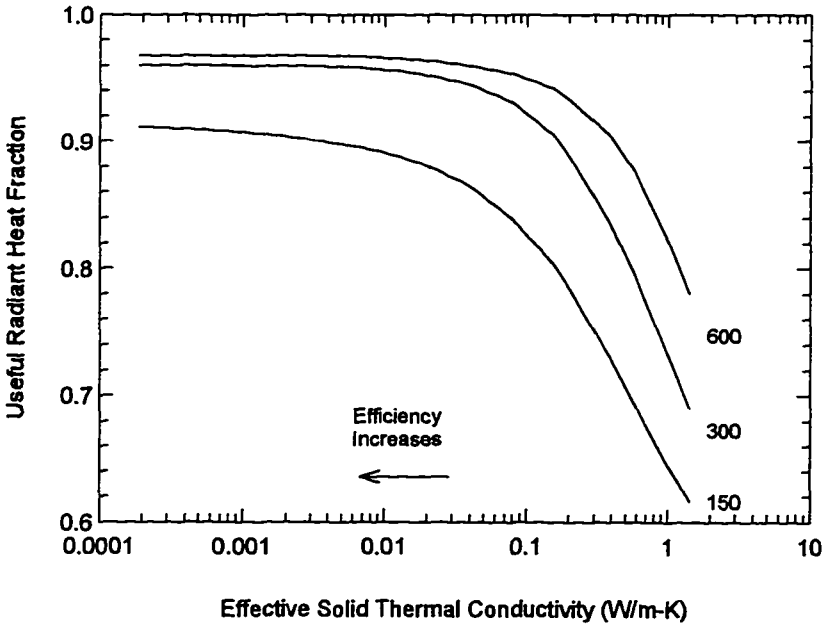

Figure 3-25: Fraction of heat transferred from the gas to solid that is converted into forward (useful) radiation as thermal conductivity varies for three firing rates (in kW/m²). The equivalence ratio is 0.9.

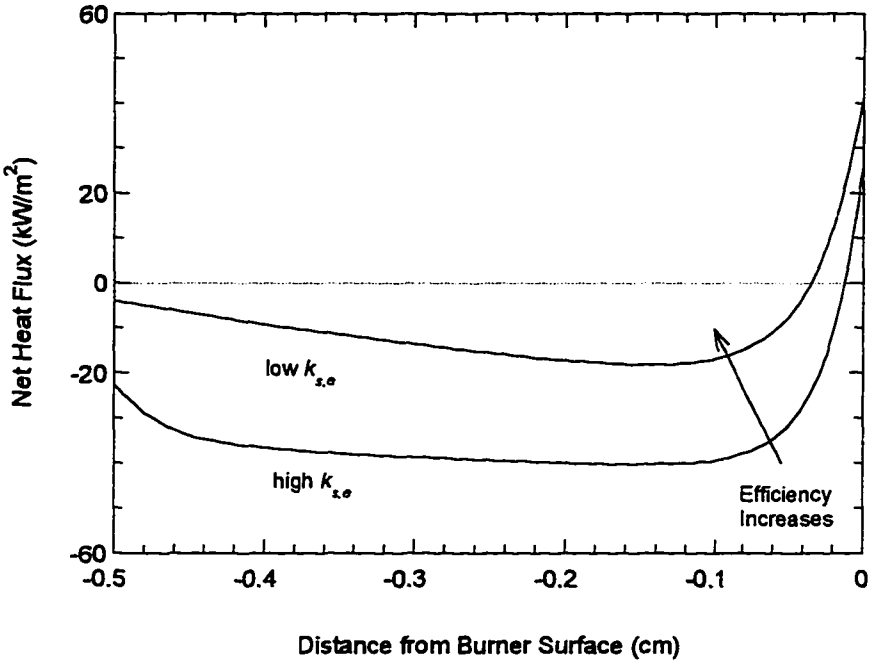

Figure 3-26: Net heat flux in porous medium for two effective thermal conductivities ($k_{s,f}$) at a firing rate of 150 kW/m² and ϕ = 0.9.

The most important conclusion to draw from the results presented above is that the heat transferred from the gas to the solid is roughly constant for surface-flame burners at a given flow rate and equivalence ratio. The flame properties are roughly independent of burner design; radiant efficiency changes are almost exclusively caused by redirection of heat. An increase in radiant efficiency occurs when high fractions of the heat transferred from the gas to the solid are converted into forward radiation (recall Figure 3-22 and Figure 3-25).

3.8 BILAYERED SURFACE-FLAME BURNER

In the previous sections, the porous medium of the surface-flame burner has been a single layer with constant properties throughout. Heat escaping through

3.8 BILAYERED SURFACE-FLAME BURNER

In the previous sections, the porous medium of the surface-flame burner has been a single layer with constant properties throughout. Heat escaping through the upstream edge of the porous medium was shown to reduce radiant efficiency. Thus, heat propagation through the porous medium should be reduced. Additionally, the high radiant efficiency of a submerged-flame burner demonstrates that by allowing the flame to stabilize in the porous medium the heat lost by the flame can increase (see Chapter 6 or Mital *et al.*, 1995). Decreasing the "denseness" (e.g. optical denseness, convective heat transfer coefficient) of the burner will allow the flame to crawl into the burner, but will also allow heat to escape through the upstream boundary. With this in mind, we simulated a bilayered *surface-flame burner*, which we call the "backstop" burner. Figure 3-27 shows the design of a backstop burner, which is a surface-flame burner with a dense, thin layer on the upstream edge of the porous medium. The burner operates in surface mode for high stability.

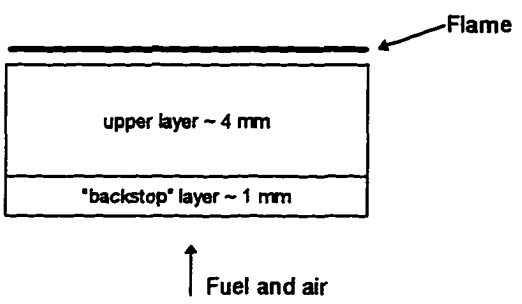

Figure 3-27: Schematic of a "backstop" burner, which is a surface-flame burner with a dense, thin layer added to the upstream edge. The burner operates in surface mode.

We performed simulations of these burners for firing rates of 150 and 300 kW/m^2 at $\phi = 0.9$ and varied the extinction coefficient, porosity and effective thermal conductivity of the upper layer. Table 3-1 shows the properties of the backstop layer and the base upper layer (which is the starting point for all parameter variations). The results for the backstop burner are compared with results for the surface-flame burner of the previous section (the "single-layer burner")

	"Backstop" layer	Base upper layer
Burner thickness (mm)	1	4
Extinction coefficient (m^{-1})	4000	1000
Scattering albedo	0.7	0.7
Forward scattering fraction	0.65	0.65
Bulk thermal conductivity (W/m-K)	0.1	10
Porosity (%)	65	80
Fiber diameter (μm)	22	22

Table 3-1: Properties of the backstop burner. The base upper layer is the starting point for all parameter variations.

Figure 3-28 shows the dependence of radiant efficiency on the extinction coefficient of the upper layer. The backstop burner has a slightly higher radiant efficiency than the single-layer burner for most conditions. A large increase in radiant efficiency occurs for very low extinction coefficients at 300 kW/m^2 because the burner is shifting into submerged-flame mode. The shift does not occur for the lowest firing rate because the upper layer is still dense enough to prevent the weaker flame from moving upstream. Since we are not interested in

submerged-flame mode at this time, the results at very low extinction coefficient are not relevant (submerged-flame burners will be covered in detail in Chapter 6).

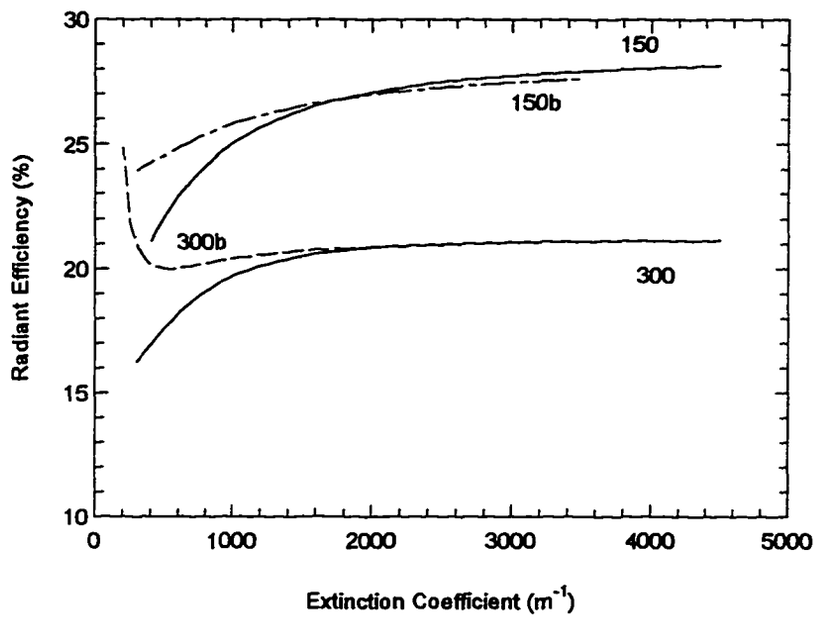

Figure 3-28: Radiant efficiency for single-layer (solid lines) and "backstop" burners (dashed lines) as extinction coefficient of the upper layer varies for two firing rates at $\phi = 0.9$. The numbers refer to firing rate in kW/m² and the letter 'b' signifies a backstop burner.

The same trend of slightly higher radiant efficiency in the backstop burner as porosity and effective thermal conductivity are varied is shown in Figure 3-29 and Figure 3-30. By preventing heat from escaping through the upstream edge of the burner, the backstop burner increases radiant efficiency marginally. Efficiencies are about 10% higher than the base radiant efficiency (for example, a radiant efficiency increase from 15% to 16.5% or from 19% to 21%), which might not justify the added cost of a bilayer structure.

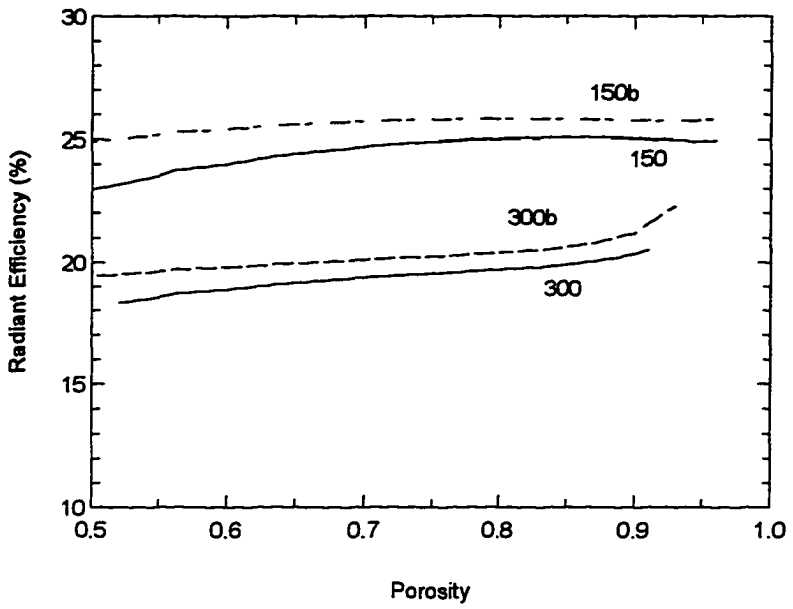

Figure 3-29: Radiant efficiency for single-layer and "backstop" burners as porosity of the upper layer varies for two firing rates at $\phi = 0.9$. The numbers refer to the firing rate in kW/m² and the backstop burners are denoted with dashed lines and a 'b'.

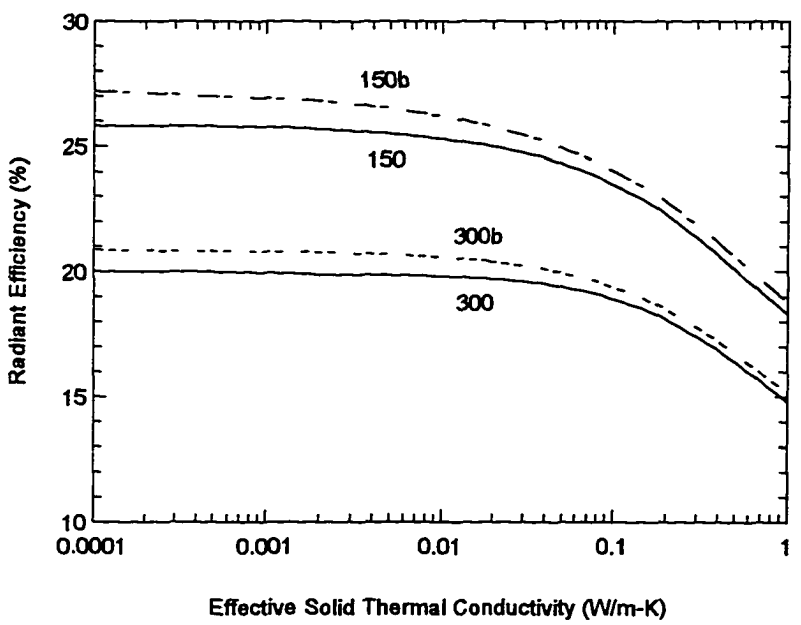

Figure 3-30: Radiant efficiency for single-layer and "backstop" burners as effective thermal conductivity of the upper layer varies for two firing rates. The numbers refer to the firing rate in kW/m² and the backstop burners are denoted with dashed lines and a 'b'.

3.9 CONCLUSIONS

Surface-flame burners have been simulated with a reduced methane combustion mechanism that compares favorably with the detailed mechanism. A parametric study of radiant efficiency in surface-flame burners showed that the following properties lead to maximum radiant efficiency: high extinction coefficient, low single scattering albedo, low thermal conductivity, high porosity, and large thickness. Radiant efficiency changes caused by variations of more than one parameter are generally not additive.

The amount of heat transferred from the flame to the porous medium is nearly constant for most variations of porous medium properties and depends primarily on equivalence ratio and firing rate. Radiant efficiency changes are a result of heat redirection inside the porous medium. A highly efficient burner will convert all of the heat transferred from the gas into forward radiation. Thus, the maximum radiant efficiency of a surface flame burner is the amount of heat that the flame must lose for stabilization divided by the firing rate.

A "backstop" burner, which is a surface-flame burner with a dense layer added to the upstream edge of the burner (thus creating a bilayered porous medium), can increase radiant efficiency in surface-flame burners marginally.

The next chapter contains a detailed analysis of NO_x formation in surface-flame burners.

3.10 REFERENCES

Bowman, C.T., Hanson, R.K., Davidson, D.F., Gardiner, Jr., W.C., Lissianski, V., Smith, G.P., Golden, D.M., Frenklach, M., and Goldenberg, M. (1995), GRI-Mech 2.11, http://www.me.berkeley.edu/gri_mech/

Frenklach, M. (1991), "Reduction of Chemical Reaction Models," in *Numerical Approaches to Combustion Modeling* (E. S. Oran and J. P. Boris, Ed.), Progress in Astronautics and Aeronautics, Vol. 135, American Institute of Aeronautics and Astronautics, Washington, D.C., pp. 129-154.

Fristrom, R.M. (1995), *Flame Structure and Processes*, Oxford University Press (New York).

Hsu, P.-F. and Matthews, R.D. (1993), "The Necessity of Using Detailed Kinetics in Models for Premixed Combustion in Porous Media", *Combustion and Flame* 93(4), pp. 457-466.

Kazakov, A. and Frenklach, M. (1994), *DRM-19*, http://www.me.berkeley.edu/drm/

Khanna, V., Goel, R., and Ellzey, J.L. (1994), "Measurements of Emissions and Radiation for Methane Combustion within a Porous Medium Burner", *Combustion Science and Technology* 99, pp. 133-142.

Kulkarni, M.R. (1996) "Experimental and Numerical Analysis of Radiant Surface Burners", Ph.D. dissertation, Arizona State University.

Kulkarni, M.R. and Peck, R.E. (1993), "Modeling Radiant Surface Burner Performance", 1993 Fall Meeting of the Western States Section of the Combustion Institute, Menlo Park, California, Paper WSCI 93-106.

Mantle, W.J. and Chang, W.S. (1991), "Effective Thermal Conductivity of Sintered Metal Fibers", *Journal of Thermophysics and Heat Transfer* 5 (4), pp. 545-549.

Mital, R., Gore, J.P., Viskanta, R., and Singh, S. (1995), "Global Radiation and Emission Characteristics of Reticulated Ceramic Radiant Burners", in *Proceedings of 1995 Joint Thermal Meeting on Combustion Fundamentals and Applications* (J.P. Gore, Ed.), Central and Western States and Mexican National sections of the Combustion Institute, pp. 32-37.

van Maaren, A., Thung, D.S., and De Goey, L.P.H. (1994), "Measurement of Flame Temperature and Adiabatic Burning Velocity of Methane/Air Mixtures", *Combustion Science and Technology* 96(4-6), pp. 327-344.

Viskanta, R. (1995) "Interaction of Combustion and Heat Transfer in Porous Inert Media", International Symposium on Transport Phenomena in Combustion (ISTP-8), July, San Francisco, CA.

Wang, H. and Frenklach, M. (1991), "Detailed Reduction of Reaction Mechanisms for Flame Modeling", *Combustion and Flame* 87, pp. 365-370.

Williams, A., Woolley, R., and Lawes, M. (1992), "The Formation of NO_x in Surface Burners", *Combustion and Flame* 89, pp. 157-166.

CHAPTER 4

Nitric Oxide Formation in Surface-Flame Burners

4.1 INTRODUCTION

Understanding of interactions between premixed flames and porous media will enable design of radiant burners with higher radiant efficiency, wider operating range and lower pollutant emission. As nitrogen oxide ($NO_x \equiv NO + NO_2$) regulations become more stringent, design of gas burners with minimal NO_x emissions will be critical.

This chapter uncovers the most important mechanisms of NO_x formation in surface-flame burners and explores whether fundamental performance limits may exist. We numerically and experimentally investigate NO_x formation in surface-flame burners operating in radiant and blue-flame mode and present NO_x profiles that show the chemical kinetic source of the NO_x. The model points to methods to reduce NO_x levels in current burners.

4.2 PROPERTIES OF THE POROUS MEDIUM

The surface-flame burner examined in this chapter has a porous medium that is fabricated from 22-micron diameter fibers of a high-temperature alloy. The thickness of the porous medium is 2.2 mm and the porosity is 0.8. The gas-to-solid convection coefficient is from measurements by Golombok *et al.* (1991) and depends on porosity, fiber diameter, gas velocity and local gas properties. We use reasonable estimates for the following properties: an extinction coefficient of 1000 m^{-1}, a scattering albedo of 0.7, and a forward scattering fraction of 0.65. The effective thermal conductivity is calculated with a formula from Mantle and Chang (1991). Details about the properties of the porous medium are in Chapter 2 (Section 2.7.1.1).

4.3 REACTION RATE ANALYSIS

We use a chemical mechanism for methane combustion (GRI-Mech 2.11, Bowman *et al.*, 1996) that includes nitrogen chemistry and consists of 49 species and 279 reactions. We consider the following NO formation mechanisms in our reaction rate analysis:

1. the extended Zeldovich mechanism, $N_2+O \leftrightarrow N+NO$, $O_2+N \leftrightarrow NO+O$, $N+OH \leftrightarrow NO+H$ (Zeldovich, 1946);
2. the Fenimore pathway, which is initiated by $CH+N_2 \leftrightarrow HCN+N$ (Fenimore, 1970);
3. the N_2O mechanism, $NH+NO \leftrightarrow N_2O+H$, $NCO+NO \leftrightarrow N_2O+CO$; and $N_2O+O \leftrightarrow 2NO$ (Wolfrum, 1972; Malte and Pratt, 1974);
4. the NNH mechanism, $NNH+O \leftrightarrow NH+NO$ (Bozzelli and Dean, 1995);
5. the remaining reactions in the mechanism that produce NO

Reactions involving conversion of NO_2 to NO are not considered because NO is converted into NO_2 in the flame front and then the NO_2 is converted back to NO, resulting in no significant change in the NO concentration. At high pressure or in combustors with rapid quenching (such as gas turbines), however, the reconversion of NO_2 to NO can be incomplete, which results in elevated concentrations of NO_2 (Flagan and Seinfeld, 1988). In the surface-flame burner studied here, NO_2 emissions are insignificant; nearly all of the NO_x is NO.

The contribution from each NO mechanism was found by reaction rate analysis, as in Schlegel *et al.* (1994). The NO production rate for each mechanism was calculated and the production rate was numerically integrated to obtain an axial NO profile. The result was then multiplied by the molecular mass of NO and divided by mass flow rate per unit area, thus

$$[\mathrm{NO}]_i(x) = \frac{M_{NO}}{\dot{m}''} \int_0^x \dot{\omega}_i \, dz \qquad [4\text{-}1]$$

where $[NO]_i(x)$ is the concentration of NO produced by the i-th mechanism at location x, M_{NO} is the molecular mass of NO, $\dot{m}''$ is the mass flow rate per unit area (g/s-cm^2) and $\dot{\omega}_i$ is the reaction rate (mol/s-cm^3) for the i-th NO mechanism. The contribution of N-atoms from the Fenimore pathway was calculated by determining the fraction of N atoms created by the reaction $CH+N_2 \leftrightarrow HCN+N$ and by the HCN to NCO to NH to N pathway, which Miller and Bowman (1989) describe as the primary pathway for NO formation through the $CH+N_2$ reaction (i.e. the Fenimore mechanism).

4.4 EXPERIMENTAL MEASUREMENTS OF NO_x

We experimentally measured NO_x profiles above a surface-flame burner with a porous medium that was made of sintered metal-fibers. A 2.2-mm thick, 152-mm on a side square metal-fiber porous medium was glued into a housing that was filled with glass beads to ensure a uniform flow to the burner. The burner was mounted on an up-down translation stage. The burner radiated to the room and the gases cooled naturally. Natural gas (about 95% CH_4) was metered with a calibrated rotometer and air was metered with a sonic-orifice flow meter.

Exhaust gases were sampled above the center of the burner using a vertical uncooled low-aspect-ratio quartz probe with a orifice diameter of 0.6 mm and an expansion ratio of 4.3 inside the probe. The sample-collection pump

was sufficiently powerful to ensure sonic conditions in the probe. After a short passage (~30 cm) through stainless steel tubing, the sample entered a heated line that was maintained at 80°C to prevent water from condensing in the line before the water trap. The sample entered an ice bath for water removal and then entered the analyzer. We used a Horiba Chemiluminescent NO_x-analyzer with ranges of 0-10 ppm and 0-30 ppm, and 9.4 ppm NO_x span gas. O_2 was measured with a Horiba magneto-pneumatic analyzer; CO_2 was measured with a Horiba infrared analyzer (Disclaimer: mention of company names does not imply endorsement).

We measured NO_x, O_2, and CO_2 concentrations for three firing rates (200, 300, and 600 kW/m^2) at $\phi = 0.9$ and two firing rates (200, 300 kW/m^2) at $\phi = 0.8$. At the lower firing rates the burner was operating in radiant mode, but at 600 kW/m^2 the flame was slightly lifted around the edges of the metal fiber porous medium and thus technically a blue-flame burner. All measurements were made for total NO_x to avoid concerns about conversion of NO to NO_2. Our modeling shows that nearly all of the NO_x is NO for the conditions we are studying .

4.5 COMPARISON OF MODEL AND EXPERIMENT

Model predictions of NO_x concentration (corrected to 0% oxygen, dry) for $\phi = 0.9$ are compared with measurements in Figure 4-1. The agreement is good at lower firing rates but not at the highest firing rate. For the highest firing rate, the gas is hot enough such that the Zeldovich mechanism is active, thus the temperature of the gas is extremely important. The gas above the burner radiates heat and additional heat was lost from the porous medium to the burner housing. Calculations in which the gas temperature is artificially lowered above the burner by just 5% (70-100 K) show excellent agreement with the experiment (see the dashed line in Figure 4-1). We suspect that the combination of gas radiation and heat loss to the burner housing lowered the temperature enough to slow NO_x formation. Thus, a slight deviation in temperature at the highest firing rate could result in the discrepancy between the model temperature and experiment temperature because the active NO_x formation mechanisms are extremely sensitive to temperature. Nonetheless, we can learn much from the numerical model even with this over-prediction of NO_x.

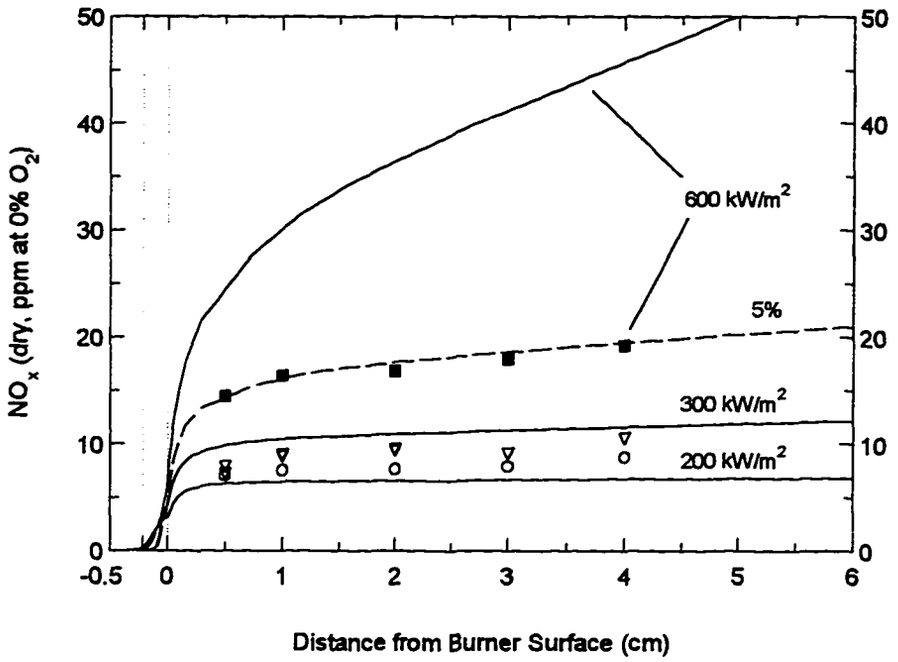

Figure 4-1: Predicted and measured NOx profiles for three firing rates at $\phi = 0.9$. Upper line and solid squares 600 kW/m², blue-flame mode; middle solid line and triangles are 300 kW/m², radiant mode; lower solid line and circles are 200 kW/m², radiant mode. The dashed line shows the effect of decreasing the 600 kW/m² temperature by 5% (70-100 K) above the porous medium. The porous medium extends from -0.22 cm to 0.0 cm. The appearance of NO_x in the porous medium is a result of the correction to 0% O_2.

Figure 4-2 shows the calculated gas temperature profiles for the experimental burner at $\phi = 0.9$. Final temperatures for each condition are noted on the right side of the figure. The upper limit of the plot is deliberately set to 2137 K—which is the adiabatic flame temperature of a $\phi = 0.9$ methane-air flame—to highlight the temperature decrease that is obtainable by using a surface-flame burner. In this case, we find temperature decreases of between about 200 and 500 K.

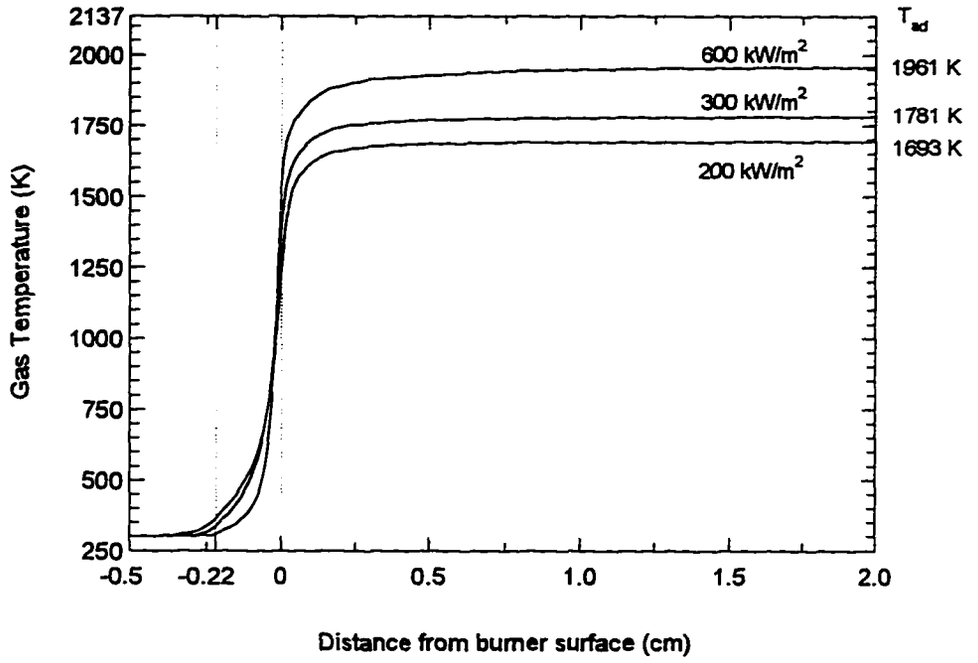

Figure 4-2: Gas temperature predictions for $\phi = 0.9$ and three firing rates. Note that 2137 K is the adiabatic flame temperature of a $\phi = 0.9$ methane-air mixture. The order of the temperature curves on the upstream edge of the porous medium is reversed, i.e. 600 kW/m² has the lowest upstream temperature. The porous medium extends from -0.22 cm to 0.0 cm.

Measurements and predictions for $\phi = 0.8$ are shown in Figure 4-3. Agreement is fair. The deviation at the lower firing rates for both equivalence ratios is possibly caused by uncertainty in rate constants of the less-well known NO mechanisms or experimental uncertainty. Overall, the model shows good agreement with the experiments, but for higher firing rates we consider the predictions to be an upper bound.

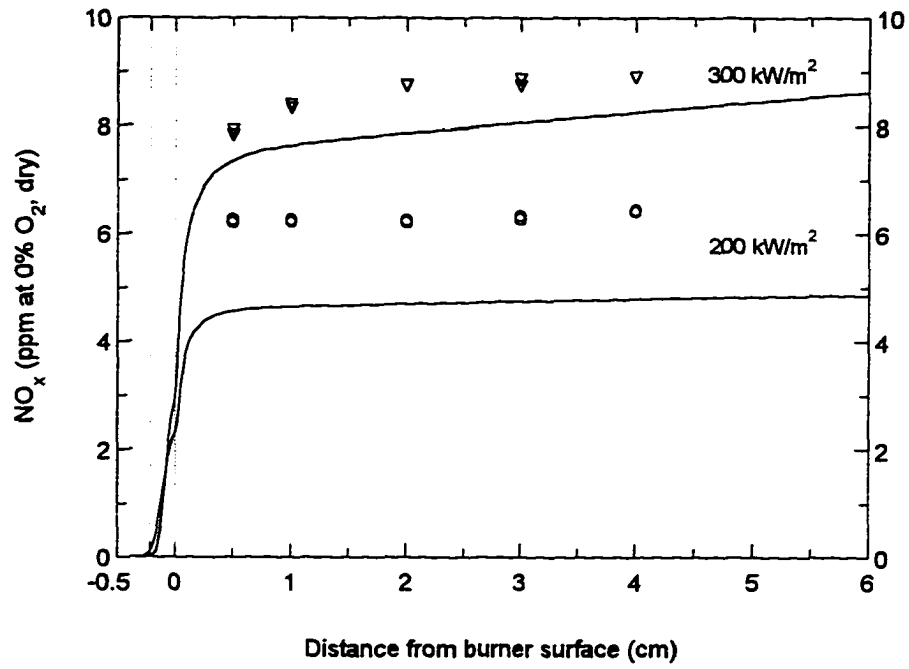

Figure 4-3: Predicted and measured NO_x profiles for two firing rates at $\phi = 0.8$, full radiant mode. Upper solid line and triangles correspond to a firing rate of 300 kW/m²; lower solid line and circles represent a firing rate of 200 kW/m². The appearance of NO_x upstream of the porous medium is a result of the correction to 0% O_2.

4.6 NUMERICAL ANALYSIS OF NO FORMATION MECHANISMS

Calculations were performed for commonly used equivalence ratios (ϕ = 0.8 and 0.9) and firing rates (200, 300 and 600 kW/m²). In each figure, the porous medium extends from -0.22 to 0.0 cm. The calculated NO levels shown in Figures 4-4, 4-5, and 4-6 are not corrected for oxygen or water. Note that the final mole percent of O_2 is 1.92% at ϕ = 0.9 and 3.88% at ϕ = 0.8. The final mole percent of H_2O is 17.3% at ϕ = 0.9 and 15.5% at ϕ = 0.8.

Figure 4-4 shows the NO profiles for a burner operating on the lower zone of the blue-flame mode (600 kW/m^2, ϕ = 0.9). NO levels reach almost 20 ppm just past the flame front, as about 15 ppm are formed in the flame front. For this firing rate, the Zeldovich reactions are dominant and responsible for much of the NO just above the burner, which causes the NO concentration to increase steadily until the gases cool. The peak gas temperature is 1961 K, which is approximately160 K lower than the adiabatic flame temperature of a ϕ = 0.9 methane-air mixture. The heat transfer from the flame to the porous medium reduces the NO formation rate substantially, resulting in a low-NO premixed burner with high stability. The NNH, N_2O and 'other' pathways each contribute about 2-4 ppm of NO; the Fenimore mechanism is responsible for about 1 ppm.

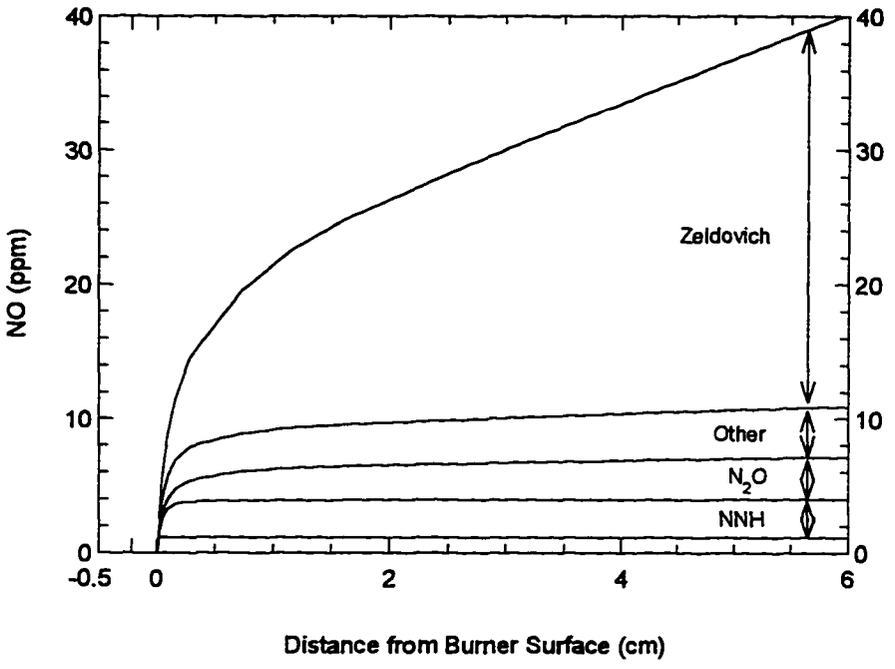

Figure 4-4: NO contributions from each mechanism and the combined NO concentration. The firing rate is 600 kW/m² and $\phi = 0.9$; the burner is most likely operating in blue-flame mode. The uppermost solid line is the total NO; lower lines delineate the contribution from each mechanism. The region between the x-axis and the first curve denotes the Fenimore NO contribution. The porous medium extends from -0.22 to 0.0 cm in this figure and following figures. The peak gas temperature is 1961 K.

As we decrease the firing rate and enter the radiant mode, more heat is extracted from the flame to stabilize it on the porous medium. Since the NO formation rate is highly dependent on gas temperature, the temperature change causes a significant alteration of the NO formation pathways. Figure 4-5 shows NO mechanism contributions for 300 kW/m² and $\phi = 0.9$. Most of the NO is formed in the flame front primarily through the NNH, N_2O and 'Other' pathways. Therefore, even if the exhaust gases are cooled immediately, at least 7

ppm of NO will be formed. Less than one-seventh of the NO is formed through the Fenimore pathway.

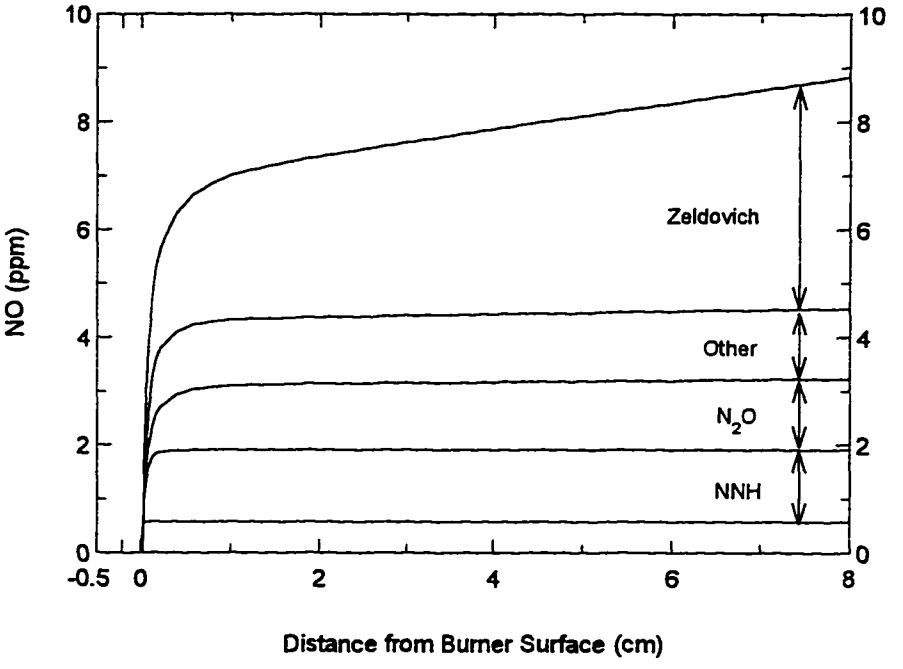

Figure 4-5: NO contributions from each mechanism and the combined NO concentration. The firing rate is 300 kW/m² and ϕ = 0.9. The uppermost solid line is the total NO; lower lines delineate the contribution from each mechanism. The region between the x-axis and the first curve denotes the Fenimore NO contribution. The peak gas temperature is 1781 K.

At the lowest firing rate (200 kW/m²) and lowest equivalence ratio (ϕ = 0.8), non-flame-front Zeldovich NO is almost negligible and most of the NO is formed in the flame front (see Figure 4-6). The contributions of flame-front Zeldovich, NNH, N_2O and 'Other' mechanisms are roughly equal at about 0.7 ppm each. The Fenimore mechanism is responsible for one-twelfth of the NO.

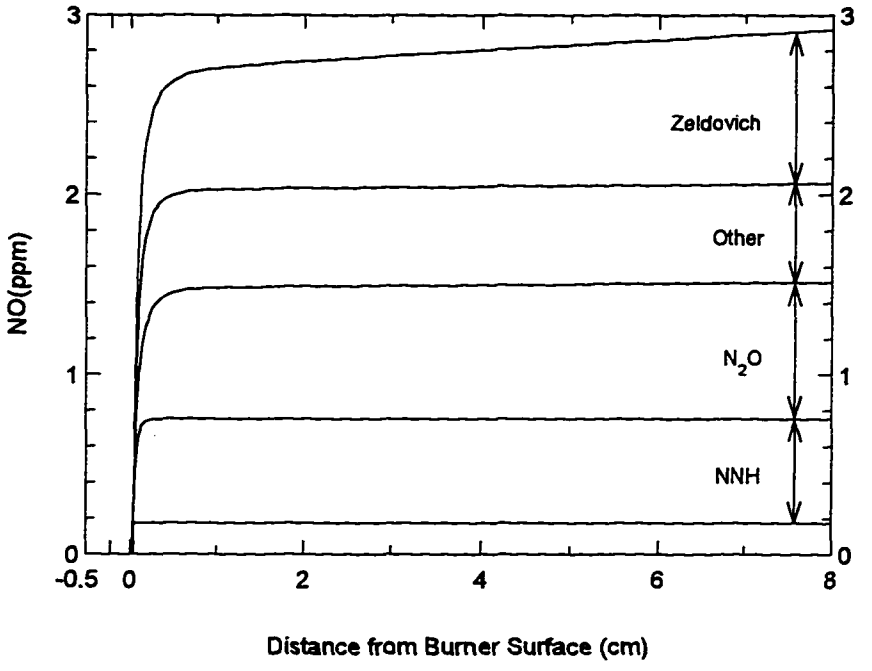

Figure 4-6: NO contributions from each mechanism and the combined NO concentration. The firing rate is 200 kW/m² and ϕ = 0.8. The uppermost solid line is the total NO; lower lines delineate the contribution from each mechanism. The region between the x-axis and the first curve denotes the Fenimore NO contribution. The peak gas temperature is 1655 K.

Presentation of NO_x emissions is not straightforward because NO_x reaches equilibrium very slowly. If one presents NO_x vs. firing rate, for example, the slope of the curve depends on how far away from the burner the NO_x is sampled. This behavior is shown in Figure 4-7, where NO_x emission indices at two distances are presented as a function of firing rate. The NO_x emission index ($EINO_x$) is defined as the mass of NO_x divided by the mass of fuel burned (similar to that of Turns and Myhr (1991)),

$$EINO_x(g/kg) = \frac{X_{NO} + X_{NO_2}}{X_{CH_4,i}} \cdot \frac{M_{NO_2}}{M_{CH_4}} \cdot 1000 \qquad [4\text{-}2]$$

where X_{NO} is the mole fraction of NO, X_{NO_2} is the mole fraction of NO_2, $X_{CH_4,i}$ is the initial mole fraction of CH_4, M_{NO_2} is the molecular mass of NO_2 (46 g/mol), and M_{CH_4} is the molecular mass of CH_4 (16 g/mol). The emission index is based on the molecular weight of NO_2 to allow comparison with chemiluminescent NO_x measurements in which all of the NO is converted to NO_2 in the analyzer. The transition between radiant mode and blue-flame mode for current surface-flame burners occurs at approximately 450 kW/m² (Singh, 1996) and is marked on Figure 4-7. The increase in NO_x emission with firing rate is more dramatic at the 10-cm plane than at the 1-cm plane. The importance of Figure 4-7, though, is that it shows loose bounds for NO_x emissions at various firing rates for a given equivalence ratio. Since the model has no gas radiation or burner housing heat losses, the 10-cm curve shows the maximum NO_x emissions one can expect from the surface-flame burner. Even if the burner is housed in a location that provides instant cooling of the exhaust above the burner, the lower curve shows the NO_x emissions that can be expected, assuming that the burner housing is adiabatic. Note that as the firing rate increases the flame begins to lift off the burner, thus reducing radiant output and becoming a blue-flame mode surface-flame burner. The model considers the flame to be perfectly flat; therefore,

effects of partially-lifted flames are not explicitly accounted for.

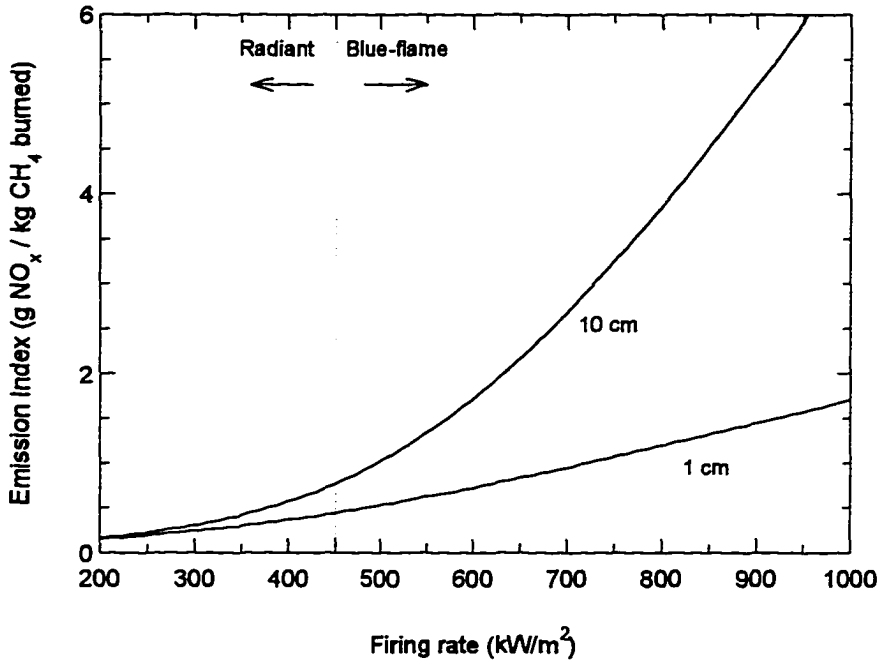

Figure 4-7: Calculated NO_x emission indices (g NO_x/kg CH_4 burned) at two distances from the burner: 1 cm and 10 cm for $\phi = 0.9$. The lower curve shows 'flame-front' NO_x while the upper curve shows NO_x formed in the flame and exhaust.

4.7 RADIANT EFFICIENCY AND POLLUTANT EMISSIONS

As the firing rate increases for a surface-flame burner, the radiant efficiency (percent of chemical input that is emitted as thermal radiation) declines while the NO_x emission rises (see Figure 4-8). Thus, a burner operated at a high firing rate will radiate inefficiently (with a partially lifted flame) and emit *relatively* high amounts of NO_x. However, the double performance penalty seen in Figure

4-8 can be avoided by augmenting the surface-flame burner with a second porous medium.

NO_x emissions in appliances have been reduced in the past by placing screens, bars or perforated metal in the flame or hot products. Surface-flame burners already have low NO_x emissions for most firing rates, but the results presented in Figure 4-7 show that if exhaust gases are cooled quickly, NO_x emissions can be lowered further. Thus, surface-flame burner users who operate at high firing rates—whether radiant efficiency is important or not—and who are concerned about NO_x emissions could lower NO_x emissions by placing a second porous medium (a "screen") downstream of the burner. Several important issues related to screens remain to be addressed. For example, an screen that is placed too close to the burner surface can interfere with the CO burn-out reactions, thus increasing CO emissions. Radiant feedback from the screen to the burner will increase the surface temperature of the burner, which will cause the flame to shift position, and might even increase the upper firing rate for radiant mode. The type and size of the screen is also important, as will be shown in Chapter 5. If the distance between the surface-flame burner and screen is reduced to zero, the flame might stabilize entirely within the porous medium, thus leading to a submerged-flame burner, a technology that is discussed in Chapter 6.

thus leading to a submerged-flame burner, a technology that is discussed in Chapter 6.

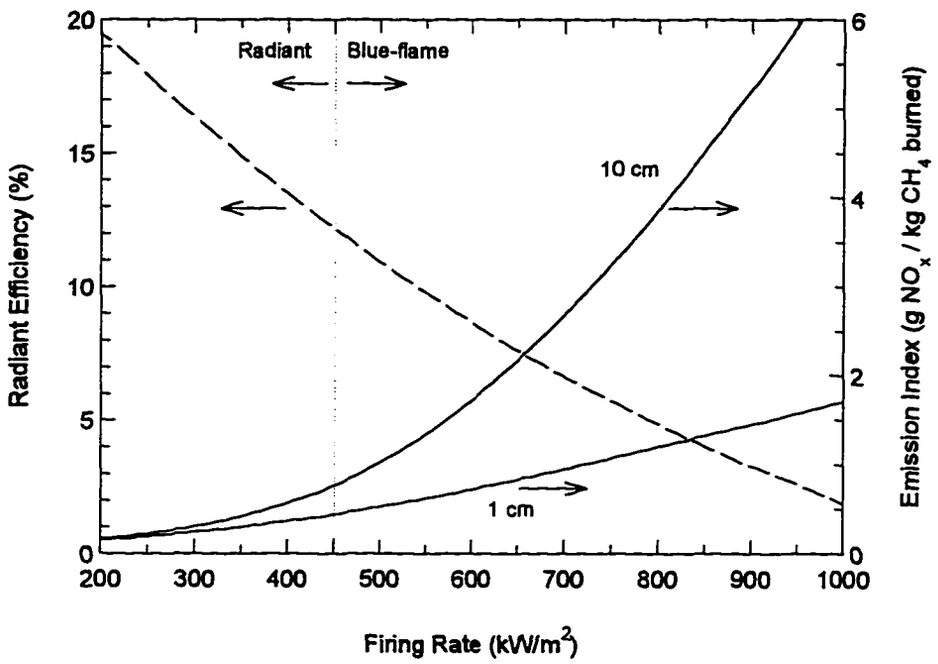

Figure 4-8: Predictions of radiant efficiency (dashed line) and NO_x emission index (g NO_x/kg CH_4 burned) at 1 cm and 10 cm above the burner. The 10-cm NO_x emission index should be seen as a rough upper limit because heat loss from the porous medium to the burner housing and radiation from the gas is neglected in the calculations.

4.8 CONCLUSIONS

Surface-flame burner operation in radiant and blue-flame mode has been simulated. Since the performance of a surface-flame burner is governed by many different factors, a comprehensive model is a valuable tool to gain insight

Deviations between model and experiment are the result of the heat loss in the experiment and uncertainty in the chemical rate constants for some of the NO reactions.

Simulations of surface-flame burners show that Zeldovich NO is significant only at high firing rates (above 600 kW/m^2 at $\phi = 0.9$), where it is responsible for 50-60% of the total NO (and increasing with height above the burner). The Zeldovich route is even more important at equivalence ratios closer to $\phi = 1.0$ and firing rates higher than 600 kW/m^2. At high firing rates with $\phi <$ 0.9, NO emissions decrease and the radiant efficiency drops rapidly. In the 200 and 300 kW/m^2 firing rate simulations, nearly all of the NO is formed in the flame front. The Zeldovich mechanism was responsible for 20-30% of the total NO, the Fenimore pathway accounts for about less than 10% of the NO, and 50-75% of the NO is formed through the NNH-path, the N_2O-path and other reactions. Since most of the NO is formed through the non-Zeldovich route at moderate to low firing rates, any attempt to predict NO emissions from surface-flame burners should use a full chemical mechanism that includes nitrogen chemistry.

The properties of the porous medium have little impact on NO_x emissions for burners operating in radiant mode (i.e., low firing rate) because changes in burner design do not cause significant temperature changes.

As firing rate increases, NO_x emissions rise rapidly. For applications that require high firing rate and extremely low NO_x, equipment to cool the exhaust gases might be appropriate. A screen, which can also protect the burner from physical damage, may cool the gases enough to suppress the thermal-NO reactions. The next chapter discusses the use of screens above radiant surface-flame burners.

4.9 REFERENCES

Bowman, C.T., Hanson, R.K., Davidson, D.F., Gardiner, Jr., W.C., Lissianski, V., Smith, G.P., Golden, D.M., Frenklach, M. and Goldenberg, M. (1995), GRI-Mech 2.11, http://www.me.berkeley.edu/gri_mech/

Bozzelli, J.W. and Dean, A.M. (1995), "O+NNH - A Possible New Route for NO_x Formation in flames", *International Journal of Chemical Kinetics* 27, p. 1097-1109.

Fenimore, C.P. (1970), "Formation of Nitric Oxide in Premixed Hydrocarbon Flames", *Thirteenth Symposium (International) on Combustion*, The Combustion Institute, Pittsburgh, pp. 373-380.

Flagan, R.C. and Seinfeld, J.H. (1988), *Fundamentals of Air Pollution Engineering*, Prentice-Hall, Inc. (Englewood Cliffs, NJ).

Fristrom, R.M. (1995) *Flame Structure and Processes*, Oxford University Press (New York).

Golombok, M., Prothero, A., Shirvill, L.C., and Small, L.M. (1991), "Surface Combustion in Metal Fibre Burners", *Combustion Science and Technology* 77, pp. 203-223.

Malte, P.C. and Pratt, D.T. (1974), "The Role of Energy-Releasing Kinetics in NO_x Formation: Fuel-Lean, Jet-Stirred CO-Air Combustion", *Combustion Science and Technology* 9, pp. 221.

Miller, J. A. and Bowman, C. T. (1989), "Mechanism and Modeling of Nitrogen Chemistry in Combustion", *Progress in Energy and Combustion Science* 15, pp. 287-338.

Schlegel, A., Buser, S., Benz, P., Bockhorn, H., and Mauss, F. (1994), *Twenty-fifth Symposium (International) on Combustion*, The Combustion Institute, Pittsburgh, pp. 1019-1026.

Singh, S. (1996), Personal communication, January.

Turns, S.R. and Myhr, F.H. (1991), "Oxides of Nitrogen Emissions from Turbulent Jet Flames - 1. Fuel Effects and Flame Radiation", *Combustion and Flame* 87(3-4), pp. 319-335.

Wolfrum, J. (1972), "Bildung von Stickstoffoxiden bei der Verbrennung", *Chemie Ingenieur Technik* 44, pp. 656.

Zeldovich, Y.B. (1946), "The Oxidation of Nitrogen in Combustion Explosions", *Acta Physiocochemica USSR* 21, pp. 577 .

CHAPTER 5

Interactions between a Surface-Flame Burner and a Screen Placed above the Burner

5.1 INTRODUCTION

Designers and users of radiant burners sometimes install a second porous medium or wire screen, called a "screen", "insert", "reverberator", or "reverberatory screen", above a radiant burner because the second porous medium can protect the burner surface from physical damage, improve burner radiant efficiency, and lower pollutant emission. For the sake of clarity and descriptiveness, the term "screen" is used to refer to the second porous medium.

Researchers at Alzeta Corporation measured the radiant efficiency and pollutant emissions of surface-flame burners with screens (Schweizer and Sullivan, 1994). Several researchers have explored the idea of using highly porous materials to capture waste heat from furnaces or, more generally, to convert convective heat to thermal radiation (Echigo, 1986; Echigo and Yoshida,

1988; Kennedy and Ettefagh, 1991). Each of the research efforts used a numerical model of the porous medium and hot gas, but did not consider chemical reactions because their applications involved gas far downstream of the flame.

The model presented in this chapter considers the system from start to finish: from reactants, through the flame zone, through the screen, and to the exhaust gas leaving the burner, with gas phase chemical reactions throughout. Not only does this allow investigation of the effect of a downstream screen on a premixed flame, but also allows analysis of pollutant formation. In this chapter we numerically analyze a surface-flame burner (which stabilizes a flame on the surface of an inert porous medium) with an added screen by using the one-dimensional model described in Chapter 2 with an additional model for the screen. The influences of burner-screen distance and screen properties on radiant efficiency, nitrogen oxide ($NO + NO_2 = NO_x$) formation, CO formation and flame stabilization are analyzed.

5.2 MODEL DESCRIPTION

A surface-flame burner with screen is a strongly coupled system with multiple interactions between different heat transfer modes and chemical reactions. In order to allow tractable simulations but retain important features of the burner-screen system, a number of assumptions and simplifications were made. The

overall model is one-dimensional, which is an appropriate assumption for surface-flame burners operating at laminar flow rates. However, the view factor (a geometric parameter that is defined as the fraction of the thermal radiation leaving one object which is intercepted by another object) between burner and screen is formulated in a way that considers non-infinite edge effects. The primary non-infinite effect is that as the screen is positioned farther from the burner, the view factor between burner and screen decreases. Other phenomena, such as convection heat transfer to the screen are calculated neglecting edge effects, which are expected to be small. Heat losses to the burner housing are negligible.

A popular design for a radiant burner screen is a woven wire mesh because of strength and availability. The radiative properties of wire mesh are not known and closed form view factor correlations are unavailable. A simplified model of the screen, which considers the screen to be a row of cylindrical tubes at constant temperature, is a satisfactory alternative. Furthermore, modeling the screen as a single row of tubes, as opposed to a woven wire mesh, allows use of radiative and convective correlations for tubes, which are not available for woven meshes. In any case, the essential physics are retained in the simplified model.

Figure 5-1 shows the computational domain for the model. In the model, combustion of premixed fuel and air occurs in an adiabatic, one-dimensional

duct that contains a porous medium and a screen. Fuel (CH_4) and air at 300 K enter an adiabatic duct at the bottom ($x = x_{in}$), flow into the porous medium (which extends from $x = -L$ to $x = 0$). Combustion occurs near the surface of the porous medium. The combustion products pass over the screen at $x = x_s$ and exit at $x = x_{out}$.

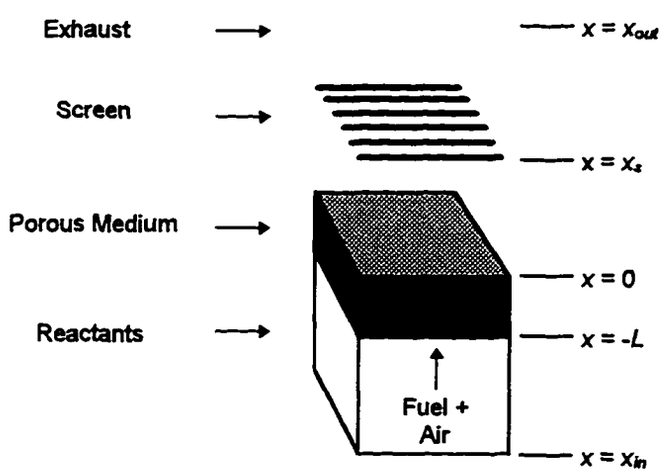

Figure 5-1: Computational domain for radiant burner model. $x = x_{in}$ is the fuel and air inlet, $x = -L$ and $x = 0$ are the edges of the porous medium (shaded region), $x = x_s$ is the location of the screen, and $x = x_{out}$ is the exit for the hot products.

Governing equations and boundary conditions for the burner alone are in Chapter 2. The radiant burner is a surface-flame burner, which was chosen for this study because it is stable (both physically and numerically) and is a typical direct-fired radiant burner.

5.3 RADIATION NETWORK MODEL

The model for the radiant heat transfer between the screen and burner is a simple radiation network. The use of networks to solve radiation problems was first proposed by Oppenheim (1956); details about the method can be found in most heat transfer texts (for example, Holman, 1990; Incropera and DeWitt, 1990). Figure 5-2 shows the burner-screen system with each object labeled and Figure 5-3 shows the network model of the radiant burner and screen. Object 1 is the burner, object 2 is the screen, object 3 is the downstream ambient surroundings (the "load"), and object 4 is the burner housing. Only radiation that impinges on the load (object 3) is considered in the efficiency calculation. Part of the radiant output from the burner passes through the screen undisturbed. Also, a portion of the radiation from the screen does not return to the burner, but instead is lost to the "housing".

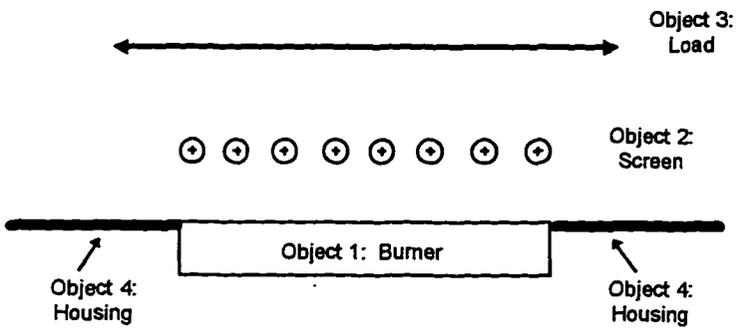

Figure 5-2: Schematic of burner-screen system with objects labeled.

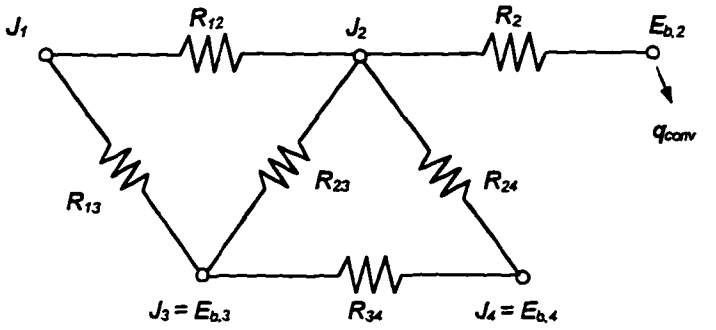

Figure 5-3: Radiation network for radiant burner and screen. The burner is object 1, the screen is object 2, the downstream ambient environment is object 3, and the upstream ambient environment is object 4. Note that objects 1 and 4 do not radiatively interact.

The node points ("voltages") are the radiosity (J_i) of the i-th object (the amount of radiation that leaves the i-th object). The "current" in the network is heat flux. The heat transfer resistances are defined by

$$R_{12} = \frac{1}{A_1 F_{12}},\ R_{23} = \frac{1}{A_2 F_{23}},\ R_{13} = \frac{1}{A_1 F_{13}},\ R_{24} = \frac{1}{A_2 F_{24}},\ R_{34} = \frac{1}{A_3 F_{34}},\ R_2 = \frac{1-\varepsilon_2}{\varepsilon_2 A_2} \qquad [5\text{-}1]$$

where F_{ij} is the view factor between object i and j, A_i is the surface area of object i, and ε_i is the emissivity of object i. Note that R_{14} is infinite because objects 1 and 4 do not "see" each other (i.e. $F_{14} = F_{41} = 0$).

The values of T_2, J_2, and the net heat fluxes from each object are found by solving the network with $J_3 = \sigma T_3^4$ and J_1 equal to the net radiation leaving the burner surface. A 'current' balance is written for the J_2 node

$$\frac{J_2 - J_1}{R_{12}} + \frac{J_2 - E_{b,2}}{R_2} + \frac{J_2 - E_{b,3}}{R_{23}} + \frac{J_2 - E_{b,4}}{R_{24}} = 0 \qquad [5\text{-}2]$$

and for the $E_{b,2}$ node

$$\frac{J_2 - E_{b,2}}{R_2} = q_{conv} = h_o A_2 (T_2 - T_g) \qquad [5\text{-}3]$$

where h_o is the convection coefficient between the screen and gas and T_g is the temperature of the gas. The convection coefficient h_o for the screen is calculated with a correlation for a single row of tubes (see section 5.5).

The radiant efficiency of the burner and screen is the net radiation from object 1 and object 2 to object 3 (the load) divided by the firing rate (q)

$$\text{Radiant Efficiency} = \frac{1}{q}\left(\frac{J_1 - J_3}{R_{13}} + \frac{J_2 - J_3}{R_{23}}\right) \cdot 100\% \qquad [5\text{-}4]$$

Or, the radiant efficiency is the percentage of chemical enthalpy input that is converted to radiant energy that strikes the load.

5.4 VIEW FACTOR CALCULATIONS

The view factor (also known as configuration factor) F_{ij}, defines the fraction of radiation from object i that is intercepted by object j. Equations for view factors of various simple and/or infinite objects are provided in many heat transfer books (e.g. Siegel and Howell, 1992). View factor calculations for complex objects, in contrast, are extraordinarily involved and closed-form expressions are rarely available. We approximate a finite set of parallel cylinders by using a

view factor for an infinite row of cylinders above a plane and adjusting for the finite size by including a view factor for aligned parallel rectangles.

Figure 5-4 shows the cross section of an infinite plane and row of cylinders, where s is the distance between cylinder centers and D is the diameter of one cylinder. We calculate the view factor $F_{12,c}$ for a row of infinite cylinders as

$$F_{12,c} = 1 - \left[1 - \left(\frac{D}{s}\right)^2\right]^2 + \left(\frac{D}{s}\right) tan^{-1}\left(\frac{s^2 - D^2}{D^2}\right)^{1/2} \quad [5\text{-}5]$$

where 1 is the plate and 2 is the row of tubes (Incropera and DeWitt, 1990).

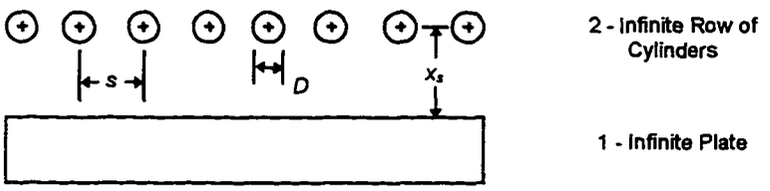

Figure 5-4: Schematic of infinite plate and row of cylinders showing cylinder nomenclature. The nomenclature is also used for the surface-flame burner and screen combination.

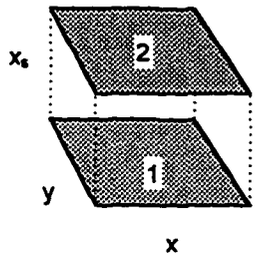

Figure 5-5: Schematic of aligned parallel rectangles used for part of view factor calculation.

The aligned parallel rectangles are diagrammed in Figure 5-5. The view factor $F_{12,r}$ for aligned parallel rectangles is calculated with the following formula:

$$F_{12,r} = \frac{2}{\pi XY}\left\{ ln\left[\frac{(1+X^2)(1+Y^2)}{1+X^2+Y^2}\right]^{1/2} + X(1+Y^2)^{1/2}\, tan^{-1}\frac{X}{(1+Y^2)^{1/2}} + X(1+Y^2)^{1/2}\, tan^{-1}\frac{X}{(1+Y^2)^{1/2}} - X\, tan^{-1}\, X - Y\, tan^{-1}\, Y \right\} \quad [5\text{-}6]$$

where $X = x / x_s$, $Y = y / x_s$., x and y are the lengths of the rectangle edges and x_s is the spacing between the rectangles (Incropera and Dewitt, 1990).

The net view factor from the burner to the screen is $F_{12} = F_{12,r} \cdot F_{12,c}$. While we concede that the view factor calculation is not exact, it captures the important features of the geometry. The other necessary view factors (burner-to-ambient, etc.) are calculated using reciprocity ($A_{ij}F_{ij} = A_{ji}F_{ji}$) and the summation rule ($\sum_{j=1}^{N} F_{ij} = 1$, where N is the total number of objects). For the screen, F_{21} is calculated by reciprocity with the burner, F_{22} is calculated through reciprocity with two infinite planes ($F_{22} = 1 - 2\,(A_1/A_2)\,F_{21}$). F_{23} is given by $F_{23} = 0.5\,(1 - F_{22})$. Then $F_{24} = 1 - F_{21} - F_{22} - F_{23}$. Thus, F_{21} is not equal to F_{23}, which further incorporates edge effects. An advantage of the radiation network method is that the only input parameters required are emissivity and the view factors. A refinement to the network could include geometrical definition of various loads for improved simulations of direct-fired radiant burners in industrial settings.

5.5 CONVECTION COEFFICIENT CORRELATION FOR THE SCREEN

The convection coefficient for the screen is calculated with a correlation for a single row of tubes (Gnielinski *et al.*, 1990), in which the Nusselt number ($Nu_L = h\,L\,/\,k_g$) is

$$Nu_L = 0.3 + \sqrt{Nu_{L,lam}^2 + Nu_{L,turb}^2} \qquad [5\text{-}7]$$

where the laminar Nusselt number is

$$Nu_{L,lam} = 0.664\,Re_{\psi,L}^{1/2}\,Pr^{1/3} \qquad [5\text{-}8]$$

and the turbulent Nusselt number is

$$Nu_{L,turb} = \frac{0.037\,Re_{\psi,L}^{0.8}\,Pr}{1 + 2.443\,Re_{\psi,L}^{-0.1}\left(Pr^{2/3} - 1\right)} \qquad [5\text{-}9]$$

with $Re_{\psi,L} = \dfrac{\dot{m}''L}{\psi\mu}$, $\psi = 1 - \dfrac{\pi}{4\,(s/D)}$, $Pr = \dfrac{\mu\,c_p}{k_g}$, and the characteristic length $L = D\pi/2$. The terms s and D are as in the view factor equation for cylinders above a plane (see Figure 5-4).

5.6 COMPUTATIONAL METHODS

The system of equations that models the radiant burner and screen is solved using the numerical methods described in Chapter 2. The screen is composed of five grid points, with finely spaced grid points in the gas-only regions upstream

and downstream of the screen to adequately resolve the temperature change in the gas. The screen is at a uniform temperature that is determined by solving Eq. [5-2] and [5-3] in conjunction with the radiant burner equations. The gas temperature used in the convective heat transfer term in Eq. [5-3] is the gas temperature at the upstream grid point in the screen. Although the screen has a spatially uniform temperature, the gas temperature varies through the screen.

5.7 COMPARISON WITH EXPERIMENTAL DATA

Researchers at Alzeta Corporation measured the radiant efficiency of a surface-flame burner with and without a screen. The experiments were made above an Alzeta *Pyrocore*® burner that has a ceramic fiber porous medium. The screen was made of a continuous fiber ceramic composite and was a woven mesh. The open area was about 30%, the fiber diameter was 3 mm, and the screen was 1 cm above the burner surface. The *Pyrocore*® burner was a 15 cm by 20 cm rectangle.

The model currently only simulates parallel cylinders, but the experimental screen was simulated by using the same open area (30%), fiber diameter (3 mm) and height of the screen (1 cm). For a 30% open area and a cylinder diameter of 3 mm, the centerline-to-centerline cylinder spacing is 4.286 mm. The size of the burner was 15 cm by 20 cm with the cylinders parallel to the short side of the burner. Even though the convection coefficient and radiation view factor are slightly different in the two configurations, the important physics are captured.

The following reasonable estimates were used for the ceramic fiber porous medium properties: thickness of 10 mm, porosity of 0.93, effective thermal conductivity of 0.05 W/m-K, extinction coefficient of 1000 m^{-1}, single scattering albedo of 0.7, forward scattering fraction of 0.65, and a convective heat transfer coefficient from a correlation reported in Andersen (1991) with f_h = 120 (see Eq. [2-19] in Section 2.7.1.2). The reduced methane mechanism *DRM19* (Kazakov and Frenklach, 1994) was used.

Figure 5-6 shows the experimental data and model predictions for a ceramic-fiber burner with a 30% open-area screen. The model prediction is in excellent agreement with the data across the range of equivalence ratios shown, despite the different screen geometry in the experiment and model.

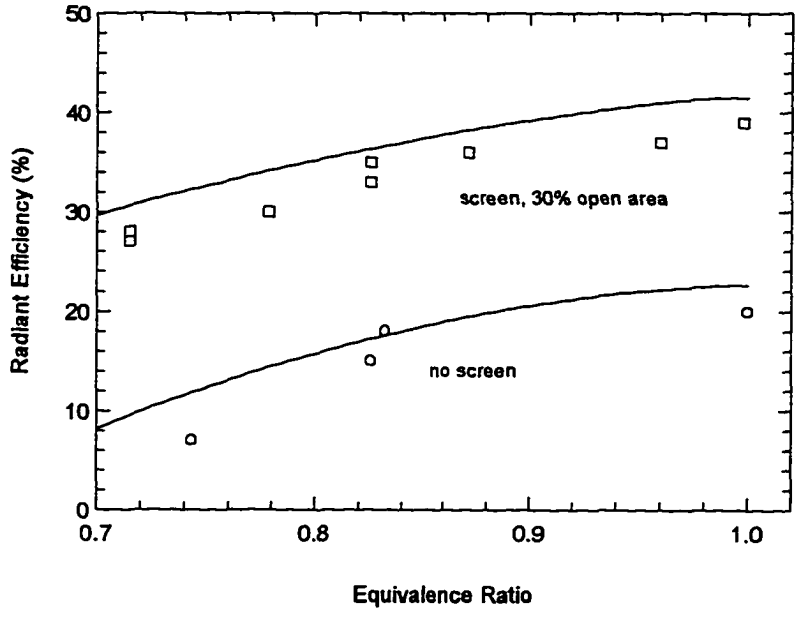

Figure 5-6: Comparison of experiment with model predictions for burners with and without a screen for a firing rate of 315 kW/m². The points represent data from Schweizer and Sullivan (1994), the curves are model predictions.

5.8 PARAMETRIC STUDY OF A SURFACE-FLAME BURNER WITH SCREEN

Calculations were performed at several different screen positions and geometries at several firing rates and equivalence ratios to determine how each parameter affects performance. The firing rates and equivalence ratios represented a wide range of operating conditions from radiant mode (150 and 300 kW/m^2 firing rates) to lifted-flame mode (600 kW/m^2, $\phi = 0.8$). The radiant efficiency, NO_x concentrations, and CO concentrations calculated for a surface-flame burner with a screen were each normalized by the value for a surface-flame burner without a screen (the "base case"), which is shown in Table 5-1. For surface-flame burners without screens, as firing rate increases (with ϕ held constant) the general trend is for radiant efficiency to decrease, and NO_x concentrations and CO concentrations to increase. As the equivalence ratio increases from the lean limit to stoichiometric (with firing rate held constant), radiant efficiency, NO_x concentrations and CO concentrations increase. At very low firing rates, however, the flame can be unstable, which results in high CO concentrations.

The burner used in the simulations in the following sections has a metal fiber porous medium. This porous medium was chosen to retain consistency with earlier chapters (3 and 4). Porous medium properties for a 5-mm thick metal fiber matrix with 22μm diameter Fecralloy fibers were described in detail in Section 2.7.1.1. The correlation for the convective heat transfer coefficient in

the porous medium is from Golombok *et al.* (1991) and the correlation for effective thermal conductivity is from Mantle and Chang (1991) with a bulk thermal conductivity of 1.0 W/m-K. Other properties for the porous medium are reasonable estimates: extinction coefficient of 1000 m^{-1}, scattering albedo of 0.65, forward scattering fraction of 0.6, and porosity of 0.8. For purposes of view factor calculation, the burner and screen are squares with 20 cm edge length. The screen is 1-mm thick with an emissivity is 0.5. GRI-Mech 2.11 (Bowman *et al.*, 1995) was used as the chemical mechanism for methane combustion.

ϕ	Firing Rate (q) (kW/m^2)	Radiant Efficiency (%)	NO_x (ppm, 0% O_2, dry)	CO (ppm, 0% O_2, dry)
0.8	150	21.5	3.4	9.2
0.8	300	14.8	9.0	50
0.8	600	5.23	44	280
0.9	150	25.4	4.8	19
0.9	300	19.3	13	110
0.9	600	10.0	70	640

Table 5-1: Radiant efficiency, NO_x concentrations, and CO concentrations for a surface-flame burner without screen (the "base case"). NO_x and CO concentrations are 'sampled' 10 cm above the burner.

5.8.1 The Influence of the Screen on Radiant Efficiency

Figure 5-7 shows how normalized radiant efficiency varies as the distance between burner and screen is changed when the screen is composed of 1-mm diameter cylinders with centerlines that are 3 mm apart (i.e. $D = 1$, $s = 3$). This is

a fairly dense packing which results in high convective heat transfer and a high view factor between the burner and screen. The efficiencies are slightly overestimated because radiation from the gas is not considered. The decrease in gas temperature from gas radiation above the burner surface will be smaller than in a screenless burner, though, because the exhaust gas is primarily radiating to two hot surfaces (the burner and the screen) instead of one hot surface and one cold surface (the burner and the room).

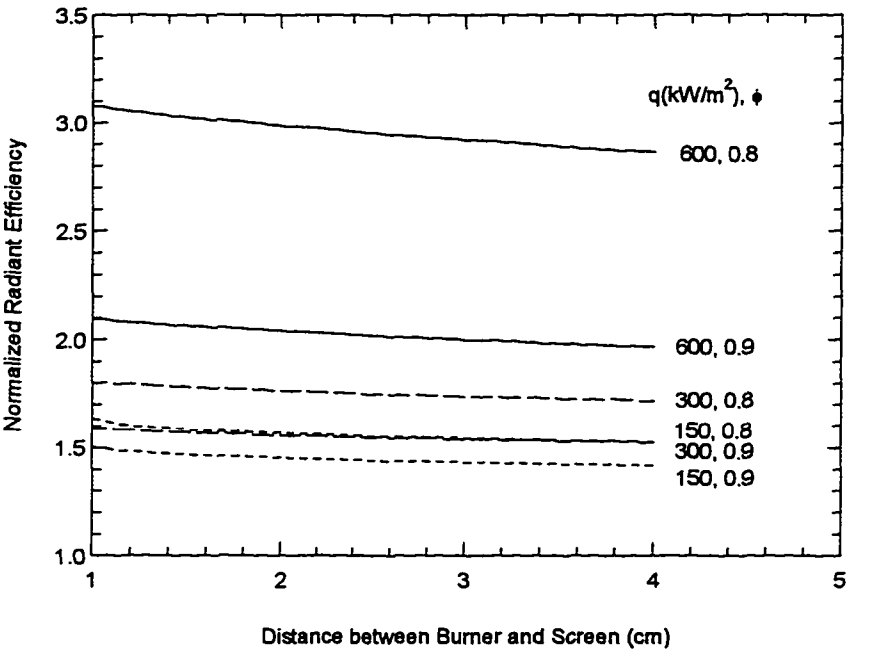

Figure 5-7: Normalized radiant efficiency for burners with D = 1.0 mm and s = 3.0 mm screens at three firing rates and two equivalence ratios. The first number next to each curve refers to firing rate (q) in kW/m² and the second number refers to the equivalence ratio (ϕ for CH_4 in air). Solid lines denote q = 600 kW/m², long dashed lines denote q = 300 kW/m², and short dashed lines denote q = 150 kW/m².

As the screen is moved away from the burner, the view factor between burner and screen decreases, which results in less radiative feedback to the burner and higher radiative losses to the burner housing. The minimal decrease in efficiency as the screen is displaced from 1 cm to 4 cm from the burner is a result of steadily increasing gas temperature in that region from chemical reactions. In other words, the increase in gas temperature compensates for a diminishing view factor between burner and screen. Gas radiation, however, would additionally result in a modest efficiency decrease as the screen is moved away from the burner.

Improvements in radiant efficiency are largest for burners with the lowest base efficiency (high q, low ϕ) because the gas flow rate is highest, which results in a large convective heat transfer coefficient between the combustion products and the screen. This result demonstrates that the radiant efficiency of surface-flame burners operating at high firing rate or lean equivalence ratio can be improved by using a screen. However, because surface-flame burners are seldom used for radiant heating with high firing rates, the impact of the efficiency gain should not be overstated.

The effects of radiation and convection are intertwined. In this model, nearly all of the heat that is convectively transferred from the gas to the screen eventually reaches the load or radiant burner (which is then re-radiated to the load and screen). Thus, a high rate of convective heat transfer is advantageous.

If the view factor is low, though, some of the heat from the screen will not impinge on the burner or the object being heated.

Figure 5-8 shows the effect of cylinder spacing (s) on radiant efficiency for two screen distances (x_s). The decrease in efficiency as cylinder spacing increases is weak, with a tripling of cylinder spacing resulting in less than a 50% decrease in efficiency. The primary reason for the weak dependence is that the convection coefficient decreases only slightly as spacing increases. Since the gas flow is laminar over the cylinders, each cylinder is roughly independent of the others, unlike in turbulent flows or in systems with multiple rows of tubes, where the flow field experienced by some tubes is a direct result of other tubes. The view factor between burner and screen decreases roughly linearly as cylinder spacing becomes larger, but the convective heat transfer from the gas to the screen is the dominant factor.

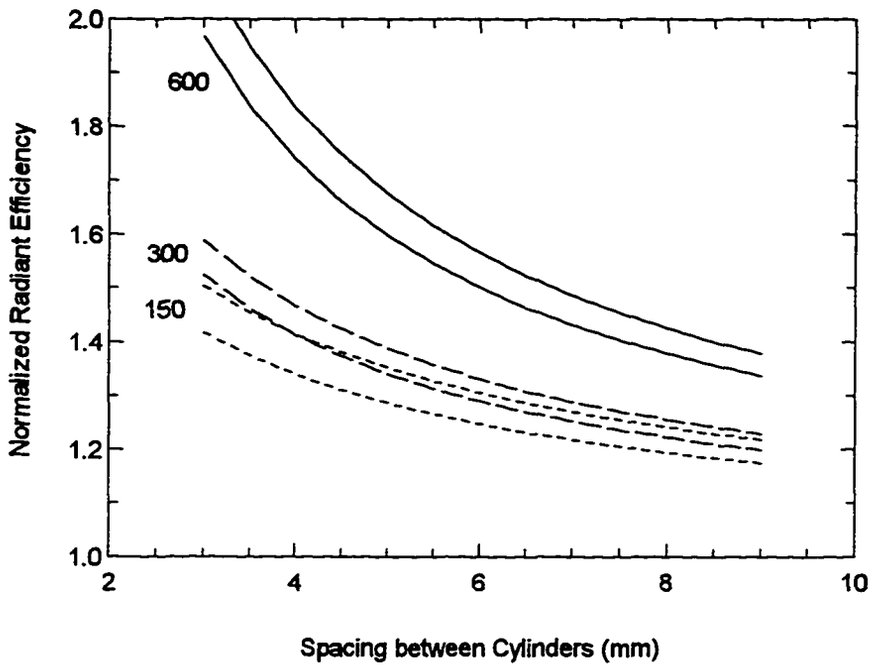

Figure 5-8: Normalized radiant efficiency as cylinder spacing varies for D = 1.0 mm. The screen was positioned at x_s = 1 cm and x_s = 4 cm. Solid lines denote the q = 600 kW/m², long dashed lines denote q = 300 kW/m², and short dashed lines denote q = 150 kW/m². The upper line for each firing rate represents the screen at x_s = 4 cm. ϕ = 0.9.

The dependence of radiant efficiency on cylinder diameter is shown in Figure 5-9 for three firing rates (q) and two burner-screen distances (x_s). As the cylinder diameter increases, the view factor between the burner and screen increases because more of the screen area is composed of solid cylinders. As a result, the radiant efficiency increases as cylinder diameter grows with constant spacing. Although large cylinders might improve steady-state efficiency, the pressure drop might be too high or the heat-up time too long for practical use.

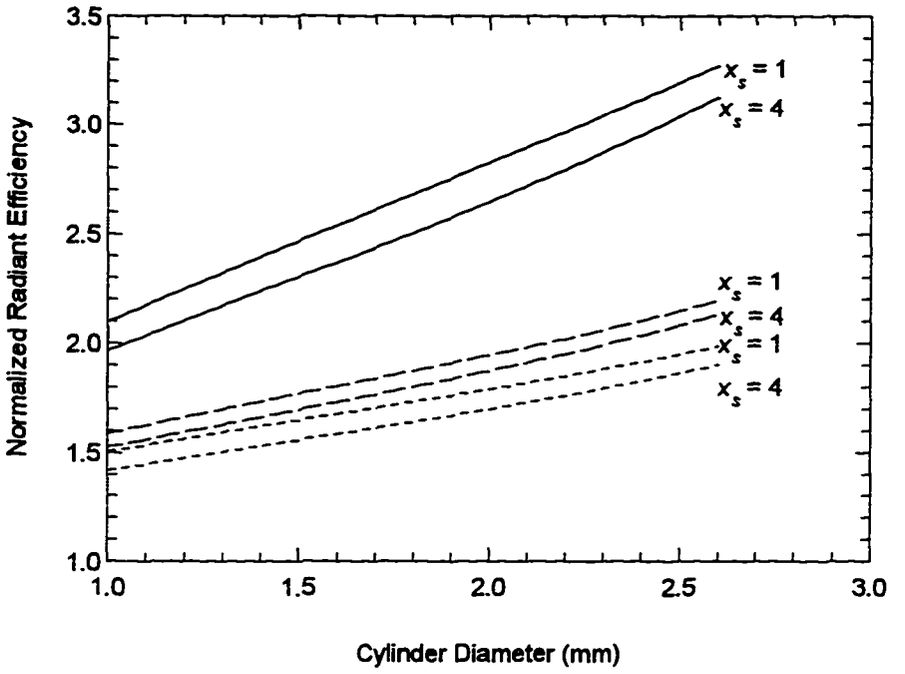

Figure 5-9: Normalized radiant efficiency as cylinder diameter (D) varies for s = 3.0 mm. The numbers to the right of the curves denote x_s in cm. Solid lines denote q = 600 kW/m², long dashed lines denote q = 300 kW/m², and short dashed lines denote q = 150 kW/m². ϕ = 0.9.

5.8.2 The Influence of the Screen on Pollutant Formation

5.8.2.1 Nitrogen Oxides

Screens have been used in gas appliances for many years to prevent thermal NO_x formation by cooling the flame. At high surface-flame burner firing rates the temperature of the exhaust gas is high enough to make thermal NO_x production significant (recall the results in Chapter 4). The NO_x results presented in Figure 5-10, Figure 5-11, and Figure 5-12 show that the most significant changes in NO_x production occur at the highest firing rate studied. We calculated large NO_x

reductions for the high firing rate because the screen cools the gases sufficiently to 'turn off' the thermal NO_x mechanism. Thus, the placement of a screen close to the burner will alleviate concerns about thermal NO_x from high firing rate burners. We found that the amount of flame-front NO_x increased slightly as a result of the radiative feedback from the screen. The decrease of NO_x emissions in a real burner at high firing rate, in which the post-flame gas temperature is decreasing through radiation, will be somewhat smaller.

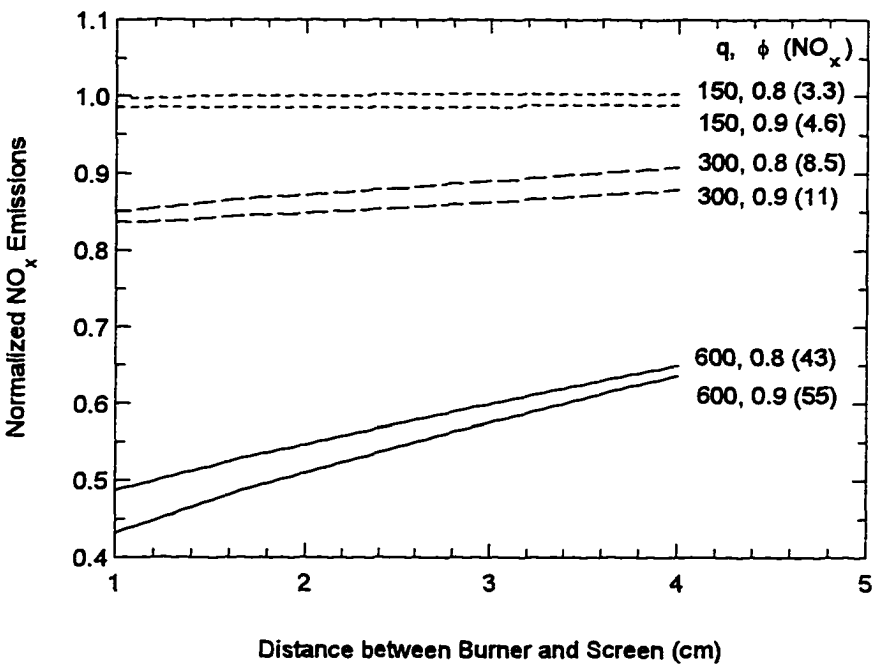

Figure 5-10: Normalized NO_x emissions 10 cm from burner with screen placed at various distances for several firing rates. The number in parentheses refers to the NO_x emission from the burner without a screen. D = 1 mm, s = 3 mm.

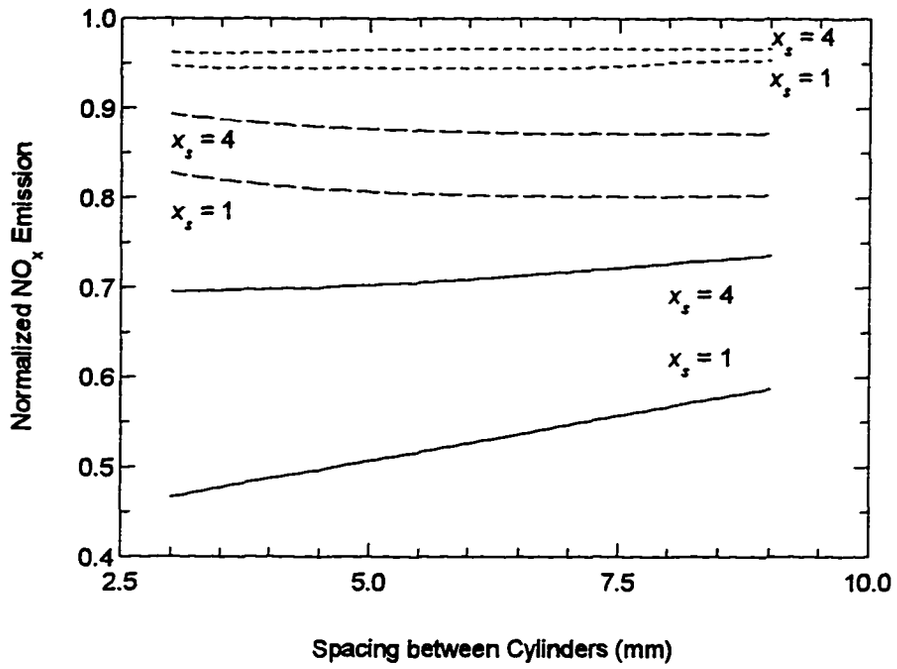

Figure 5-11: Normalized NO_x emissions 10 cm from the burner as spacing between cylinders varies at two values of x_s, for $D = 1$ mm and $\phi = 0.9$. Solid lines denote q = 600 kW/m², long dashed lines denote q = 300 kW/m², and short dashed lines denote q = 150 kW/m².

Variation of the cylinder spacing or diameter has little impact on NO_x emissions, as seen in Figure 5-11 and Figure 5-12. The small changes in NO_x production for the lower firing rates occur because the temperature of the exhaust gases is low enough that thermal NO_x formation is nearly negligible. This is not a significant setback because the NO_x emissions are already quite low (recall Table 5-1).

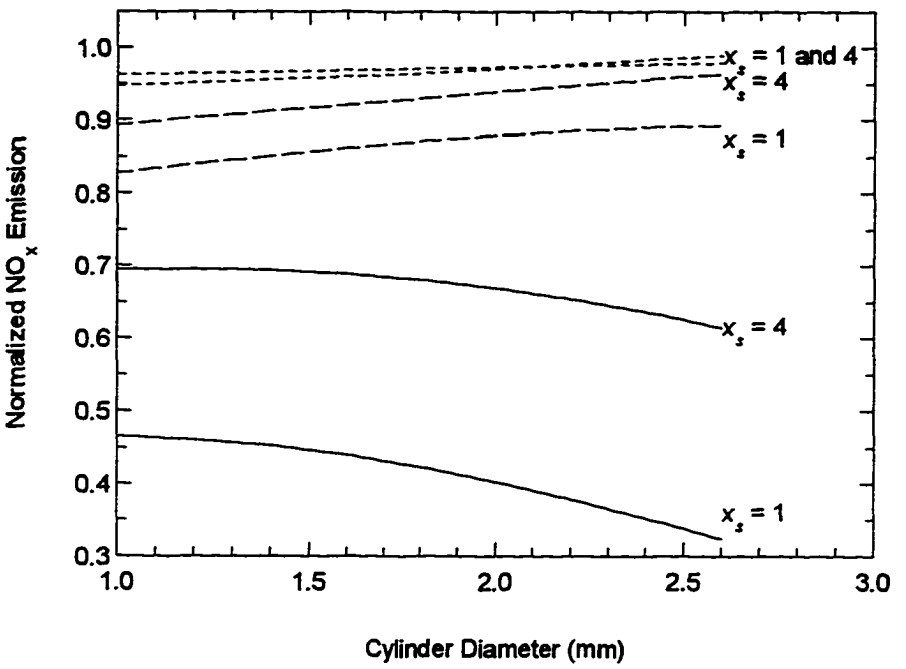

Figure 5-12: Normalized NO_x emissions as cylinder diameter varies for two screen heights. s = 3.0 mm and ϕ = 0.9. Solid lines denote q = 600 kW/m², long dashed lines denote q = 300 kW/m², and short dashed lines denote q = 150 kW/m².

5.8.2.2 Carbon Monoxide

Carbon monoxide (CO) is a concern whenever non-combustible objects interfere with a flame. It is well known that rapidly cooling a flame or exhaust interrupts the CO to CO_2 conversion, thus resulting in elevated levels of CO. Our calculations, in which the post-flame gases are rapidly cooled by several hundred Kelvin 1 to 4 cm from the premixed flame, showed dramatic *decreases* in CO concentration. This counterintuitive result encouraged us to investigate further. We used the program *Senkin* (Lutz, 1992), which simulates a one-dimensional reactor without mass transport (that is, a plug-flow reactor), to

remove transport phenomena and radiant burner specific items. The temperature profile computed by the radiant burner code was converted from distance to time and input to *Senkin* as a given temperature profile. We used two mechanisms (Miller and Bowman (1989) and GRI-Mech 2.11 (Bowman *et al.*, 1995)) to try to isolate the cause of the CO decrease. The results from *Senkin* show the same behavior as the radiant burner: as the gas cools rapidly in the screen region, the CO concentration *decreases*. Thus, we conclude that the CO behavior is not related to transport phenomena or to the radiant burner computer code. Instead, we presume that the decrease in CO is a result of an equilibrium shift: at equilibrium, the concentration of CO decreases as the temperature decreases. Equilibrium calculations confirm that the CO concentration decreases as the temperature decreases. Figure 5-13 shows the CO and temperature profiles for a burner operating at $\phi = 0.9$ and $q = 300$ kW/m^2 with and without a screen. The profiles are similar through the flame front, with the primary difference that the screened burner has a flame that is farther upstream. As the gas cools near the screen, though, the CO concentration in the screened burner decreases faster than the unscreened burner.

Optical measurements of CO (using the tunable diode laser technique of Nguyen *et al.* (1995) for example) above a surface-flame burner with screen should be performed to further investigate CO formation in the surface-flame

burner. At this stage, though, we can conclude that the addition of the screen will not have adverse effects on CO formation at distances of 1 cm and greater.

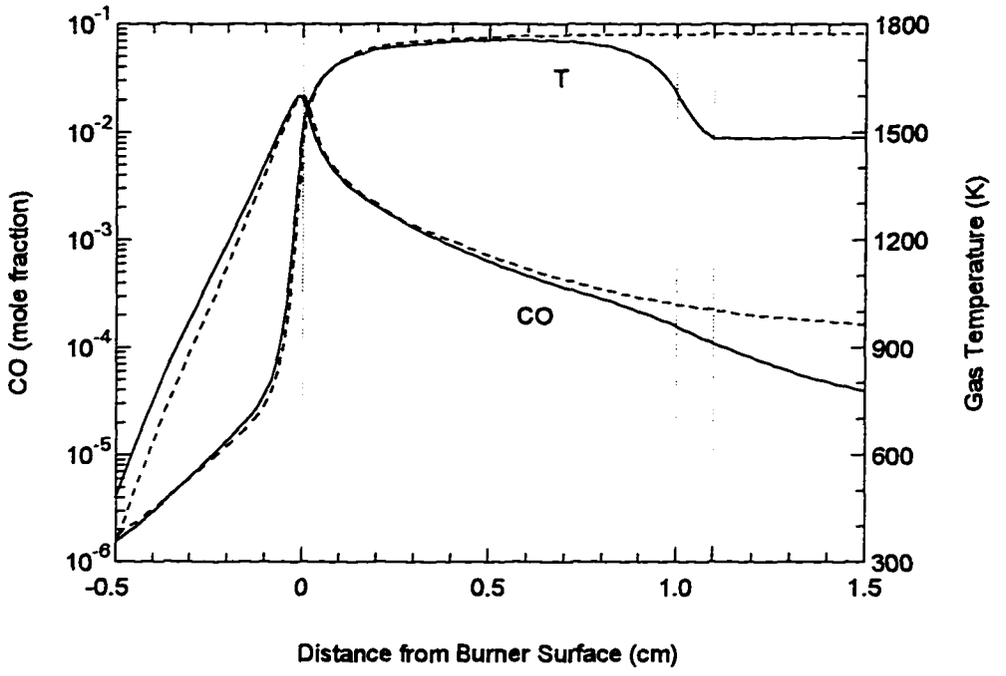

Figure 5-13: CO profiles and temperature profiles for screened (solid) and unscreened (dashed) radiant burners. The vertical dashed lines denote the location of the screen (x = 1.0 to x = 1.1). ϕ = 0.9, q = 300 kW/m².

5.8.3 The Influence of the Screen on Flame Location

Part of the heat that is absorbed by the screen (via convection or radiation) is radiated directly to the load. The remainder propagates upstream to the burner or to the upstream surroundings. The radiation that is transferred upstream to the burner significantly changes burner operation by heating the porous medium. A portion of the radiant heat from the screen propagates upstream in the radiant burner and increases the temperature of the unburned gas. The

additional preheat increases the flame speed of the mixture, which allows the flame to stabilize deeper into the porous medium. Figure 5-14 shows the flame location for a wide range of firing rates in a surface-flame burner operating with equivalence ratio of $\phi = 0.9$. The flame location is defined to be the position between the locations where 25% and 75% of the total heat release has occurred. Other surface-flame burner researchers have defined flame location as the point of maximum CH_4 decomposition (Kulkarni, 1996), but we prefer to link flame location directly to heat release. The definition that we use here considers the asymmetry of the heat release profile.

At a low firing rate, the flame is relatively far from the burner surface—even though the flow velocity is low—because the flame is sensitive to heat loss. As the firing rate increases, the heat release increases, which allows more heat transfer to the porous medium. Some of the heat propagates upstream in the porous medium and preheats the gas, which increases the laminar flame speed, allowing the flame to move upstream into the burner. Eventually, though, the convective velocity overwhelms the flame, causing it to move away from the burner (Viskanta, 1995). This behavior has been described in numerical studies (Kulkarni, 1996), but has not yet been studied experimentally.

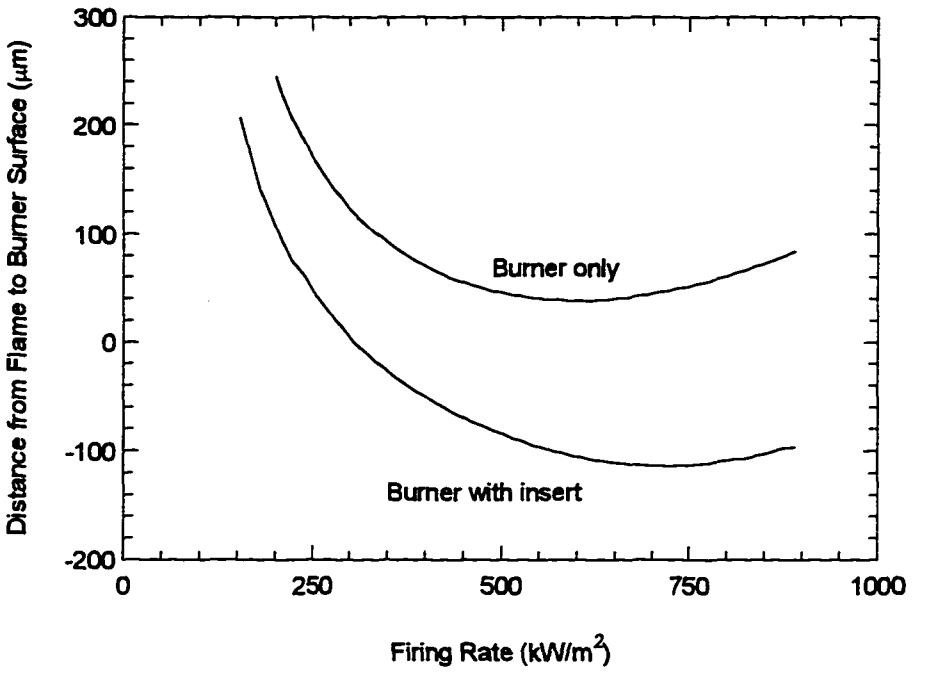

Figure 5-14: Flame location for a surface-flame burner operating at $\phi = 0.9$ with and without screen. $x_s = 1$ cm, $D = 1$ mm, $s = 3$ mm.

As seen in Figure 5-14, the radiant feedback to the burner from the screen results in deeper flame penetration into the porous medium. The same behavior was seen for $\phi = 0.8$. This increases efficiency and decreases NO_x emissions. Furthermore, radiant feedback could prevent partial flame lift-off at high firing rates by heating the burner surface. This possibility should be investigated experimentally.

5.9 EXTENSIONS OF THE MODEL

The radiation network method is an extremely flexible technique for analysis of radiation heat transfer. We envision that the model could be extended to

simulate more complex geometries, like those found in industrial drying operations. For example, a paper drying operation, such as the one shown in Figure 5-15 could be simulated as a multi-object network. The paper could be divided into zones. With the proper additions to the model, the drying rate of the paper could be calculated for various configurations and operating conditions of radiant burners.

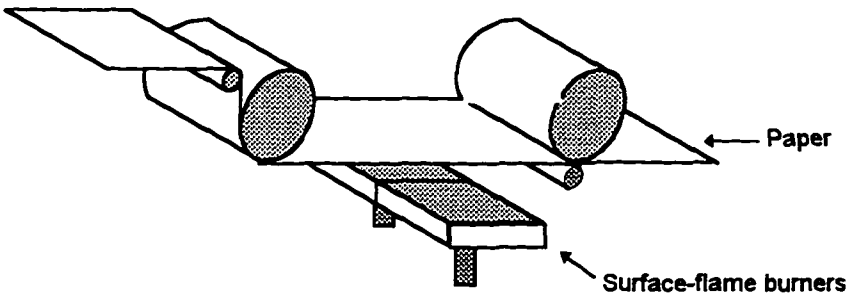

Figure 5-15: Paper drying with direct-fired radiant burners. The radiation from the burner partially dries the moving sheet of paper.

5.10 CONCLUSIONS

A one-dimensional model of a surface-flame burner with downstream screen has been used to analyze the effect of screen properties on radiant efficiency, NO_x emissions and CO emissions. Screens can improve the radiant efficiency of surface-flame burners by extracting heat from the exhaust gas. Efficiency is further improved by radiant feedback from the screen to the burner, which causes the flame to propagate deeper into the porous medium. This increases efficiency and decreases NO_x emissions. Furthermore, radiant feedback might

prevent partial flame lift-off at high firing rates. The thermal NO_x mechanism is essentially 'turned off' as the exhaust gas passes through the screen, a desirable behavior that allows surface-flame burners to be used at high firing rate without high emissions. The addition of the screen will not have adverse effects on CO formation at distances of 1 cm and greater. For highest efficiency and lowest NO_x emissions, the screen should be composed of tightly-spaced cylinders which are placed close to the burner.

5.11 REFERENCES

Andersen, F. (1992), "Heat Transport Model for Fibre Burners", *Progress in Energy and Combustion Science* 18, pp. 1-12.

Bowman, C.T., Hanson, R.K., Davidson, D.F., Gardiner, Jr., W.C., Lissianski, V., Smith, G.P., Golden, D.M., Frenklach, M., and Goldenberg, M. (1995), GRI-Mech 2.11, http://www.me.berkeley.edu/gri_mech/

Echigo, R. (1986), "High Temperature Heat Transfer Augmentation", in *High Temperature Heat Exchangers* (A.E. Sheidlin and N. Afghan, Ed.), Hemisphere Publishing Corporation (Washington, D.C.), pp. 230-259.

Echigo, R. and Yoshida, H. (1988), "High Temperature Heat and Mass Transfer in Porous Media", in *Experimental Heat Transfer, Fluid Mechanics, and Thermodynamics 1988* (R.K. Shah, E.N. Ganic, and K.T. Yang, Ed.), Elsevier Science Publishing Co., Inc. (Amsterdam), pp. 645-652.

Gnielinski, V., Zukauskas, A., and Skrinska, A. (1990), "Banks of Plain and Finned Tubes", in *Hemisphere Handbook of Heat Exchanger Design* (G.F. Hewitt, Ed.), Hemisphere Publishing Corporation (New York).

Golombok, M., Prothero, A., Shirvill, L.C., and Small, L.M. (1991), "Surface Combustion in Metal Fibre Burners", *Combustion Science and Technology* 77, pp. 203-223.

Holman, J.P. (1990), *Heat transfer*, 7th ed., McGraw-Hill (New York).

Incropera, F.P. and DeWitt, D.P. (1990), *Fundamentals of Heat and Mass Transfer*, 3rd ed., John Wiley & Sons (New York).

Kazakov, A. and Frenklach, M. (1994), *DRM-19*, http://www.me.berkeley.edu/drm/

Kennedy, L.A. and Ettefagh, J. (1991), "Passing Combustion Gases Through Multilayered Porous Surfaces to Enhance Radiative Heating", in *ASME/JSME Thermal Engineering Proceedings*, Vol. 5, p. 189-195.

Kulkarni, M. (1996), "Experimental and Numerical Analysis of Radiant Surface Burners", Ph.D. dissertation, Arizona State University.

Lutz, A.E. (1992) *Senkin: A Fortran Program for Predicting Homogeneous Gas Chemical Kinetics with Sensitivity Analysis*, Sandia National Laboratory, SAND87-8248.

Mantle, W.J. and Chang, W.S. (1991), "Effective Thermal Conductivity of Sintered Metal Fibers", *Journal of Thermophysics and Heat Transfer* 5 (4), pp. 545-549.

Miller, J. A. and Bowman, C. T. (1989), "Mechanism and Modeling of Nitrogen Chemistry in Combustion", *Progress in Energy and Combustion Science* 15, pp. 287-338.

Nguyen, Q.V., Edgar, B.L., Dibble, R.W., and Gulati, A. (1995), "Experimental and Numerical Comparison of Extractive and In Situ Laser Measurements of Non-Equilibrium Carbon Monoxide in Lean-Premixed Natural Gas Combustion", *Combustion and Flame* 100 (3), pp. 395-406.

Oppenheim, A.K. (1956), "Radiative Analysis by the Network Method", *Transactions of the ASME* 65, pp. 725-735.

Schweizer, S. and Sullivan, J. (1994), *CFCC Radiant Burner Assessment*, Alzeta Report No. 94-7607-193 (prepared for the U.S. Department of Energy), Santa Clara, CA.

Siegel, R. and Howell, J.R. (1992), *Thermal Radiation Heat Transfer*, 3rd ed., Hemisphere Publishing Corp. (Washington, D.C.).

Viskanta, R. (1995) "Interaction of Combustion and Heat Transfer in Porous Inert Media", International Symposium on Transport Phenomena in Combustion (ISTP-8), July, San Francisco, CA.

CHAPTER 6

Submerged-Flame Burners

6.1 INTRODUCTION

For the surface-flame burners of Chapters 3 and 4, the direct heat transfer from the flame to the porous medium occurs from the upstream side of the flame. The flame transfers enough heat to the porous medium to lower the flame velocity to the velocity of the incoming unburned gas. It was shown in Chapter 3 that the amount of heat transfer from the flame to the porous medium is nearly independent of the porous medium properties, but is a strong function of firing rate and stoichiometry.

By adding a second highly porous medium downstream of the first porous medium (the burner), the amount of heat transfer from the combustion gases to the porous medium can be increased. This was shown in Chapter 5, where the second porous medium (called a "screen") was 1 cm to 4 cm downstream of the first porous medium. When the separation distance between

the two porous media is zero, it is possible to stabilize the flame entirely within the porous medium, thus resulting in a "submerged-flame burner".

The second porous medium should have a low convective heat transfer coefficient, thus enabling the flame to be submerged entirely within the porous medium and allowing heat to be extracted from the products downstream of the flame. The increased contact area between the hot gas and porous medium leads to higher radiant efficiency, but a critical balance is created: radiant efficiency increases as more heat is extracted from the flame and post-flame gases, but if too much heat propagates upstream in the upstream layer, the flame will move upstream completely through the porous medium, an event called "flashback".

In this chapter, we study an industrial burner that is fabricated from a porous medium with two layers. Because of the structure of the porous ceramic, the complete name for the burner is "bilayer reticulated ceramic burner" (definition of reticulated: "resembling a net; *esp*: having veins, fibers or lines crossing" (Merriam-Webster, 1987)). The porous medium has a layer with large pores (the "downstream layer", also known as the "flame support layer") that extracts heat from the flame and post-flame gases and a layer with small pores that prevents the flame from moving upstream (the "upstream layer", also known as the "diffuser layer"). A schematic of the burner is shown in Figure 6-1. Properties of the ceramic porous medium were discussed in Section 2.7.2. In the remainder of this chapter, we describe the flame structure in the burner and

describe temperature measurements using thermocouples and OH laser-induced fluorescence (LIF). Model predictions are compared to temperature and species measurements. The influence of burner properties on radiant efficiency is studied numerically.

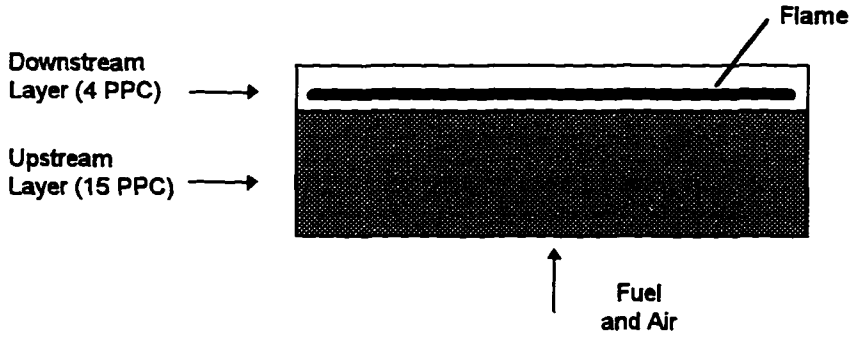

Figure 6-1: Submerged-flame burner (a.k.a. Bilayer reticulated ceramic burner). The upstream layer in the reticulated ceramic is 19-mm thick with 25 pores per centimeter (PPC) (≈ 65 pores per inch). The downstream layer is 3.2-mm thick with 4 PPC (≈ 10 pores per inch).

6.2 DEFINITIONS AND NOMENCLATURE

We will use the term *submerged-flame burner* to refer to the bilayer reticulated ceramic burner. The term submerged-flame burner is more general, but most of the results presented here can be applied to submerged-flame burners regardless of the material.

The portion of porous medium with small pores (25 PPC) will be called the *upstream layer;* the portion of porous medium with large pores (4 PPC) will be called the *downstream layer.*

6.3 FLAME STRUCTURE IN SUBMERGED-FLAME BURNERS

This section discusses flame structure in the submerged-flame burner through presentation of experimental measurements and numerical predictions of major species, minor species, chemical heat release, and nitric oxide. In the figures of flame structure that follow, the gas flows from left to right and the plot is divided into three regions by vertical dashed lines. Starting from the left, the first region (x < -3.2 mm) is a portion of the upstream layer, the second region (-3.2 < x < 0) is the downstream layer, and the third region is the gas-only region (x > 0).

Extensive measurements of temperature and chemical species in the downstream layer have been performed by researchers at Purdue University (Mital *et al.*, 1996). Using small thermocouples (diameter < 200 μm), they measured gas temperature profiles in the large pores of the downstream layer. Radiation, conduction and catalytic-heating corrections were made by repeatedly performing the measurements with thermocouples of different diameter, then extrapolating the bead diameter to zero. The researchers collected gas samples with a quartz microprobe and obtained species concentrations using gas chromatography. Note that Mital *et al.* (1995 and 1996) used the lower heating value of methane in their calculation of firing rate (50.14 MJ/kg-CH_4 vs. a higher heating value of 55.6 MJ/kg-CH_4).

Figure 6-6 shows a comparison of predicted gas temperature with measurements for a firing rate of 436 kW/m^2 and $\phi = 0.9$. The temperature of the gas rises sharply in the upstream layer, peaks inside the downstream layer and declines slightly before the exit. The decline occurs because of extensive heat loss by the porous medium through radiant emission. Since the downstream layer allows radiation to pass through it to the surroundings (i.e. optically thin), a significant fraction of the radiant energy emitted by the porous medium is not reabsorbed by the porous medium, thus leading to an overall loss in energy. As the porous medium loses energy, the gas convectively transfers heat to the porous medium. The model accurately captures this behavior.

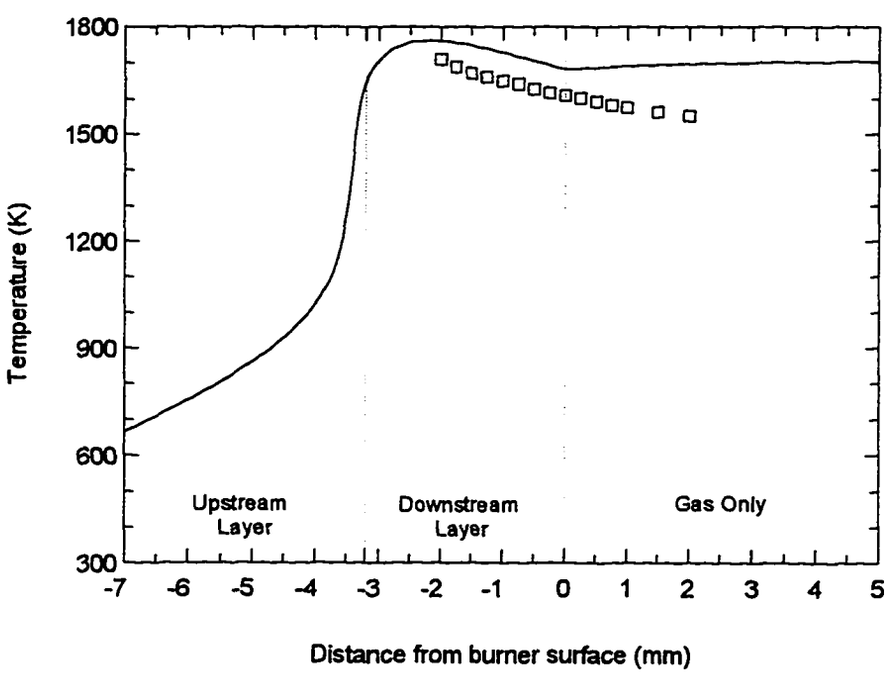

Figure 6-2: Gas temperature measurement (squares) and prediction (solid line) for a firing rate of 436 kW/m^2 and $\phi = 0.9$ for a submerged-flame burner. Only a portion of the 22.2-mm thick porous medium is shown. Data from Mital *et al.* (1996).

Figure 6-3 shows predictions and measurements of major species (CH_4, O_2, CO_2, CO) at a firing rate of 436 kW/m^2 and $\phi = 0.9$. Only the flame front is shown for clarity. Near the interface, the fuel decomposes and oxygen is consumed, eventually resulting in production of CO, CO_2 and H_2O. All of the sharp concentration gradients are within the porous medium. Considering the difficulty and uncertainty of the species measurements, the agreement between model and experiments is satisfactory. The exact position of the flame front is not matched, but the disturbance of the probe could lead to an apparent shift of the flame front by reducing methane consumption and increasing CO concentration. Furthermore, if the gas is not sampled isokinetically the apparent location flame front may be shifted.

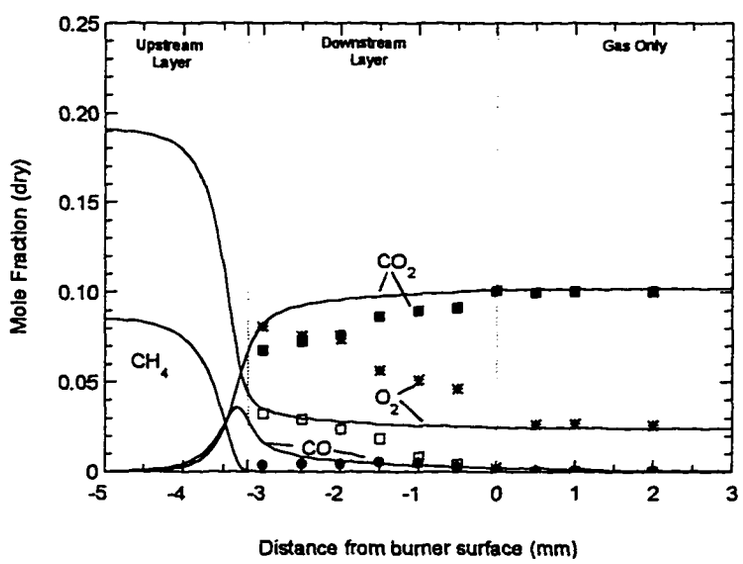

Figure 6-3: Major species measurements (points) and predictions (lines) for firing rate of 436 kW/m^2 and $\phi = 0.9$. CH_4 measurements are represented by open squares, CO by circles, O_2 by stars, and CO_2 by filled squares. Only a portion of the 22.2-mm thick porous medium is shown. Data from Mital *et al.* (1996).

The model significantly overpredicts the CO concentration, but the accuracy of probe measurements of CO is limited for these measurements because of the high temperature of the gas (approximately 1500-1800 K). Nguyen *et al.* (1995) have shown that measurement of CO concentration using extractive probe sampling is increasingly inaccurate above 1000 K.

The next set of figures show measurements and predictions for two additional firing rates: 349 kW/m^2 and 261 kW/m^2. Agreement is good, except for gas temperature at 261 kW/m^2. The temperature measurement for the 261 kW/m^2 firing rate appears dubious, though, because the measured temperature is higher than for firing rates of 349 and 436 kW/m^2. We expect that the peak temperature should decrease as the firing rate decreases.

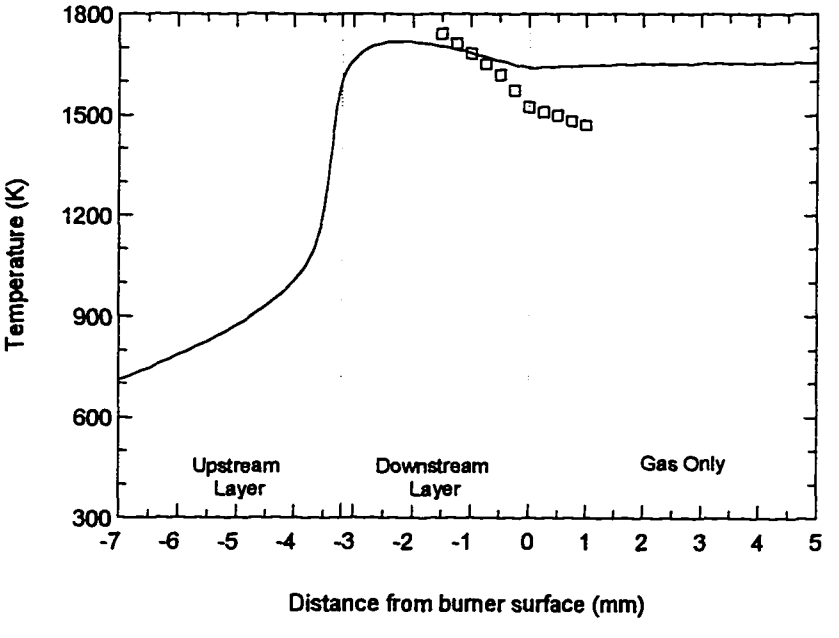

Figure 6-4: Gas temperature measurement (squares) and prediction (solid line) for firing rate of 349 kW/m^2 and $\phi = 0.9$ for a submerged-flame burner. Only a portion of the 22.2-mm thick porous medium is shown. Data from Mital et al. (1996).

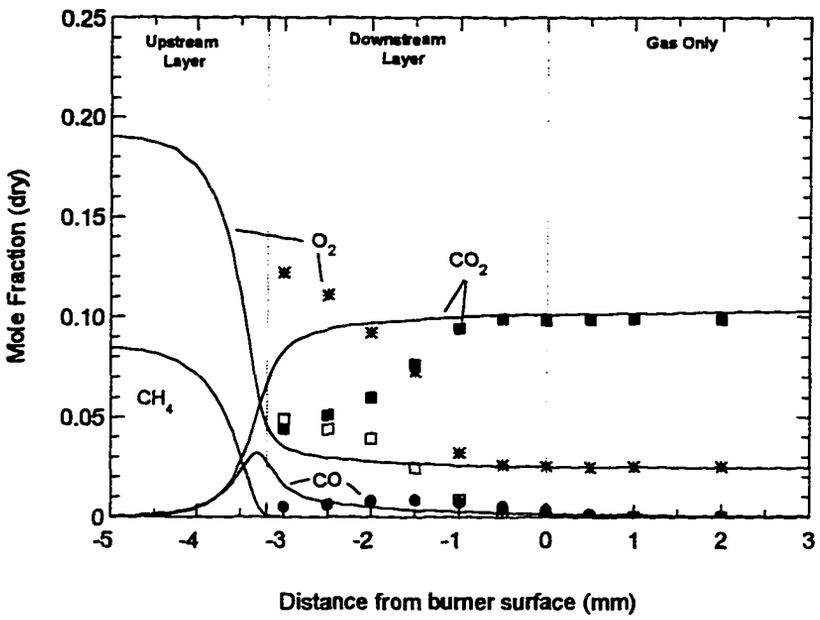

Figure 6-5: Major species measurements (points) and predictions (lines) for firing rate of 349 kW/m² and $\phi = 0.9$. CH_4 measurements are represented by open squares, CO by circles, O_2 by stars, and CO_2 by filled squares. Only a portion of the 22.2-mm thick porous medium is shown. Data from Mital *et al.* (1996).

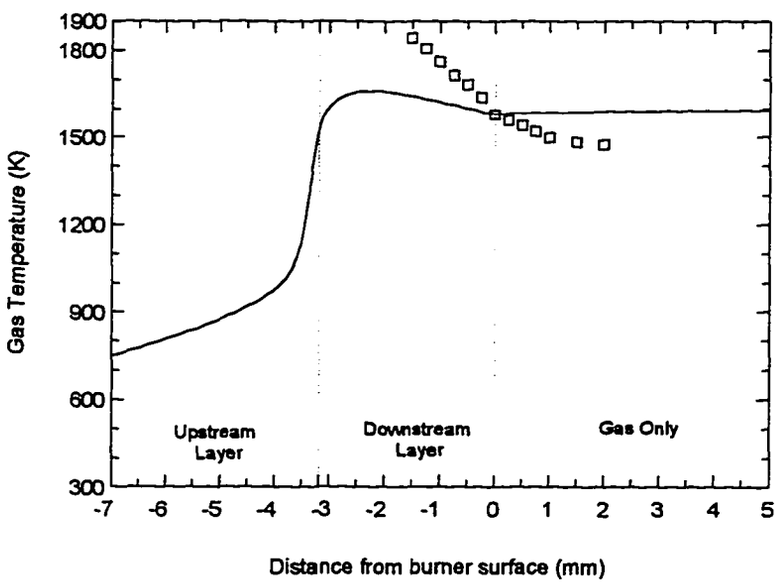

Figure 6-6: Comparisons of gas temperature measurement (squares) and prediction (solid line) for firing rate of 261 kW/m² and $\phi = 0.9$ for a submerged-flame burner. Only a portion of the 22.2-mm thick porous medium is shown. Data from Mital *et al.* (1996).

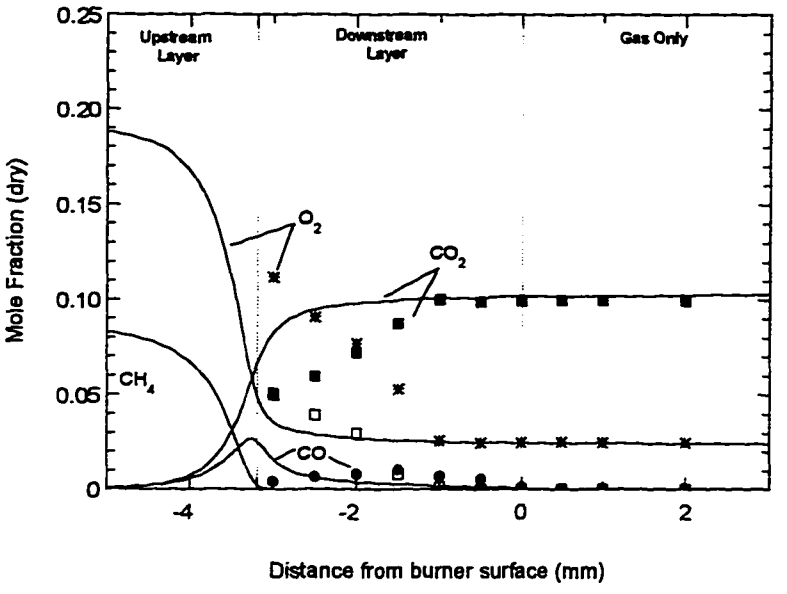

Figure 6-7: Major species measurements (points) and predictions (lines) for firing rate of 261 kW/m² and $\phi = 0.9$. CH_4 measurements are represented by open squares, CO by circles, O_2 by stars, and CO_2 by filled squares. Only a portion of the 22.2-mm thick porous medium is shown. Data from Mital *et al.* (1996).

The figures above show that the gradients of major species mole fraction are within the porous medium. The peak concentrations for most important radicals (OH, H, CH, etc.) also occur within the porous medium. However, radical concentrations may still be high enough at the exit to allow measurement (as seen for OH in Section 6.4). Predicted profiles for OH, O, and H can be found in Figure 6-8. NO formation will be examined in Section 6.6.

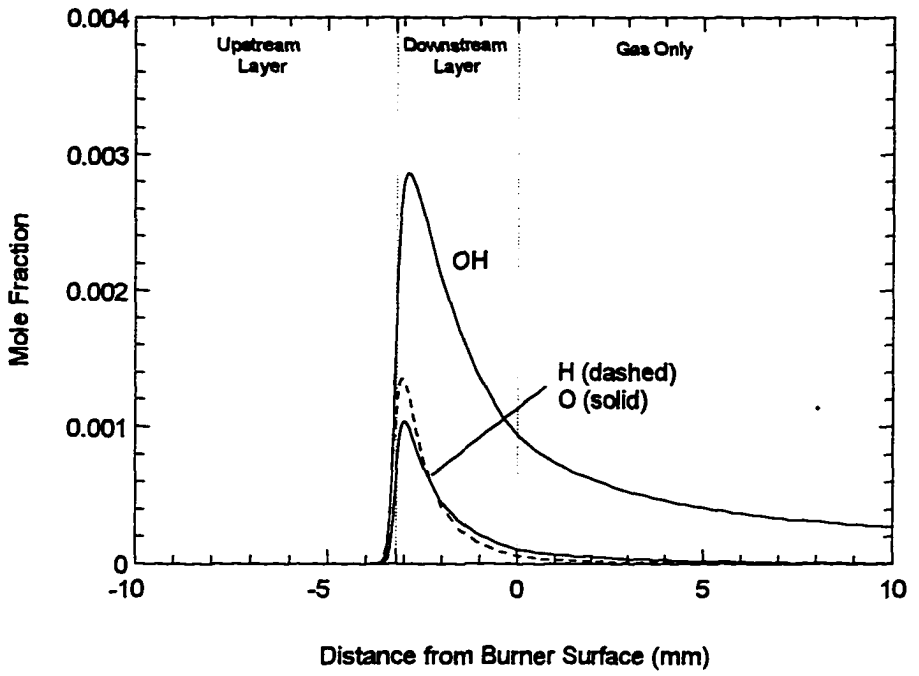

Figure 6-8: Major radical profiles at a firing rate of 315 kW/m², ϕ = 0.9. Only a portion of the 19-mm thick upstream layer is shown.

6.4 OH LIF MEASUREMENTS OF GAS TEMPERATURE

The gas temperature above the radiant burner is a valuable experimental cross-check to the model because radiant efficiency, NO_x emissions, and CO emissions all depend on the exit gas temperature. Measurement of gas temperature, though, is not a straightforward process. Thermocouples can provide erroneous results when subjected to high temperature and high radiant flux. Many optical thermometry techniques, such as visible-Raman or Rayleigh scattering, are rendered unusable by the radiant flux from the burner. OH laser induced fluorescence (LIF), however, is performed in the ultraviolet, a spectral region where little radiation is emitted from the burner. OH LIF has been shown to be

an effective technique for measuring gas temperature (Crosley and Jeffries, 1992). In this section, OH LIF temperature measurements and thermocouple measurements are described. The measurements were performed to examine the use of thermocouples at flame temperature in highly radiant environments and to provide non-intrusive temperature measurements to compare with model predictions.

6.4.1 Experimental Burner Design

The porous medium used in the experiment is a 140-mm square bilayer reticulated ceramic structure with a 19-mm thick 25 PPC upstream layer and a 3.2-mm thick 4 PPC downstream layer (Hi-Tech Ceramics, Alfred, NY), as described in Section 6.1 and shown in Figure 6-1. As Figure 6-9 illustrates, the burner housing consists of an aluminum box with an open top, rails to set the porous medium upon, and threaded holes in the side walls for thermocouple fittings. The housing is almost completely filled with glass beads to ensure an even flow.

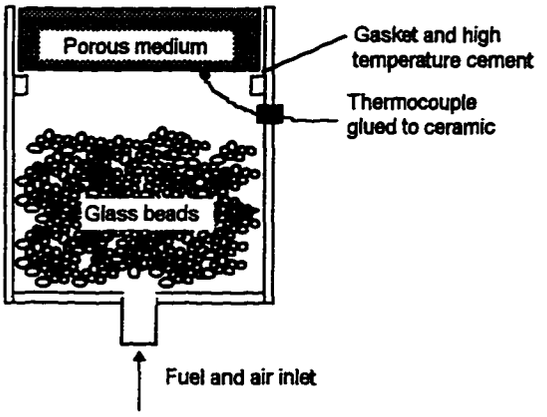

Figure 6-9: Experimental submerged-flame burner. The upstream layer in the porous medium is 19-mm thick with 25 PPC. The downstream layer is 3.2-mm thick with 4 PPC.

6.4.2 Thermocouple Measurements of Gas Temperature

A thermocouple measures the temperature of its junction; this is rarely the same temperature as the gas, especially at low flow rates and high temperatures. At high temperature, the thermocouple loses heat through radiation, causing the temperature of the bead to be lower than the temperature of the gas. A thermocouple above a highly radiating surface (such as a submerged-flame burner) has the additional complication of radiant flux *to* the bead, which will reduce the usual correction. Initially, we used wires that were housed in a straight two-hole ceramic sleeve as shown in Figure 6-10; we planned to measure with three different bead sizes and extrapolate to zero bead size to correct for losses. However, the thermocouple response depended strongly on the distance between the bead and the sleeve (the "gap" in Figure 6-10), that is, the amount of exposed wire, and we could not guarantee similarity. As the

distance increased, the temperature of the bead increased because hotter lead wires reduced conductive losses from the bead. For example, as we increased the distance between a 350 μm bead (Pt/Pt-10% Rh) and the ceramic sleeve from 0 to 1 cm the bead temperature increased by 150 K without reaching a plateau (the firing rate was 315 kW/m^2 and ϕ=0.9). The American Society for Testing and Materials thermocouple manual (1981) makes no mention of the importance of the gap. The gap between bead and ceramic was not consistent for each thermocouple, thus negating the similarity feature.

We abandoned the ceramic sleeve and instead used an uncoated type-K (Ni-Cu/Ni-Al) thermocouple with a butt-welded junction that was held in a Y-shaped support. The 460-μm diameter bead was nearly cylindrical, and several cm of wire was exposed. The thermocouple wire was parallel to the burner surface to minimize conductive losses.

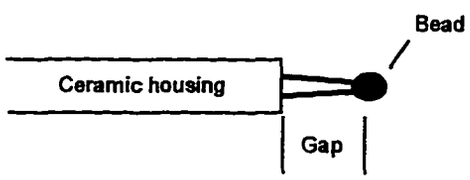

Figure 6-10: Close-up of thermocouple and housing.

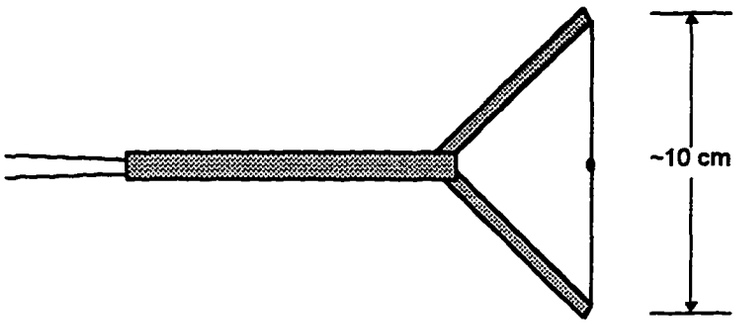

Figure 6-11: "Fork" or Y-shaped thermocouple support. The gas flow is perpendicular to the page.

We used an iterative scheme to solve an energy balance to correct for radiation and conduction losses, as in Ang *et al.* (1988). We used radiation measurements from Mital *et al.* (1995) to approximate the radiant flux from the burner. The radiation view factor for the bead is nearly 0.5 when the bead is close to the burner (Siegel and Howell, 1992). The gas properties were found with *Chemkin* subroutines (Kee *et al.*, 1984), assuming that the products are N_2, H_2O, O_2 and CO_2. The Nusselt number correlation for a smooth cylinder in cross-flow was given as $Nu = 0.8\ Re^{0.28}$ where Nu and Re are based on the cylinder diameter (Morgan, 1975). The emissivity of the Ni-Cr/Ni-Al bead is approximated from data for Ni-Cr and Ni-Al to be 0.6 (Holman, 1986).

6.4.3 OH-LIF Measurements

In addition to the thermocouple measurements, we used LIF of OH to measure the temperature above the surface. The OH molecule was excited by using the (0,0) band of the A-X transition. A Nd:YAG-pumped tunable dye laser

produced a laser beam that was focused to achieve a high resolution, but kept at sufficiently low pulse energy to avoid saturation. Using a spatial filter, the observed length along the beamline was 6 mm and the resolution perpendicular to the beam was 250 μm. Fluorescence was detected with a 1P28 photomultiplier and visible light transmission was suppressed with a UG11 glass filter, allowing detection of a wide spectral range in the region of interest. Gas temperature was determined by excitation scans that included up to 17 lines between $R_1(4)$ and $R_2(15)$ (Rensberger *et al.*, 1989).

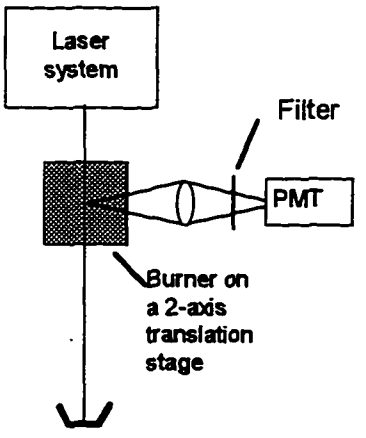

Figure 6-12: Schematic diagram of OH-LIF experiment.

6.4.4 Correction of OH-LIF Temperature Measurements

The evaluation of the LIF data requires a correction for effects of absorption of laser light and absorption of fluorescence. These corrections are based on measurements and on the calculations of Desgroux *et al.* (1995). The OH

concentration is required for this and was empirically determined by absorption measurements. The correction proposed by Desgroux *et al.* (1995) was scaled to fit our OH-concentration and dimensions. For these conditions, the overall correction for laser absorption and trapping decreases the temperature by 25 K for scans in the center of the burner according to theory in Desgroux *et al.* (1995) and assuming a flat flame. In Desgroux *et al.* (1995), the trapping correction is based on the assumption that no rotational relaxation of excited OH occurs. In our case, partial relaxation occurs and reduces the correction. Horizontal profiles showed variations on the order of 40% in the OH concentrations along the surface. The upper bound for the uncertainty resulting from partial relaxation and OH variation is approximately ±20 K. Radiant burner model calculations show a strong dependence of [OH] on the temperature (a 25% in [OH] change for a 50 K change at 5-mm height), so the observed variation of [OH] corresponds to small temperature variations. This is also indicated by thermocouple measurements. Dependence of quenching and emission rates on the rotational level of OH also requires a temperature correction, which is derived and extensively discussed in Rumminger, Heberle, Dibble and Crosley (1996). The rotational-level dependent temperature correction for the radiant burner results in a temperature increase of 20 K.

6.4.5 Temperature Measurements Compared with Modeling

Uncorrected thermocouple temperatures, made 5 mm above the burner surface in the center of the burner, were between 1180 K and 1270 K, depending on the horizontal location. The correction 5 mm above the burner, in the center, was 270 K. The temperature correction would have been 370 K if the radiation from the burner was not considered. Conductive loss accounts for about 10 K of the correction. The large radiative loss was caused by a combination of the bead size (460 μm), a high bead emissivity (0.6), a relatively low Reynolds number ($Re_d \approx 0.9$), and a relatively low Nusselt number ($Nu \approx 0.7$). Variations in the thermocouple correction can result from uncertainties in the convection coefficient, emissivity and radiation from the burner. Additionally, when the thermocouple is very close to the burner, the amount of radiation to the bead may increasingly depend on the local structure of the porous medium.

Temperatures were also determined using LIF at a height of 5 mm above the burner at various locations between the center of the burner and 40 mm off-center, moving toward the photomultiplier. LIF temperature corrections are based on an [OH] concentration of approximately $6 \cdot 10^{14}$ cm^{-3} that was derived from absorption measurements. The measured [OH] is slightly lower than the model prediction. The temperature 5 mm above the surface, corrected for absorption and rotational-level dependent effects, is 1504 K in the center, 1498 K

at 20 mm off-center, 1604 K at 30 mm, and 1567 K at 40 mm. The overall uncertainty of the LIF temperature measurements is ±60 K.

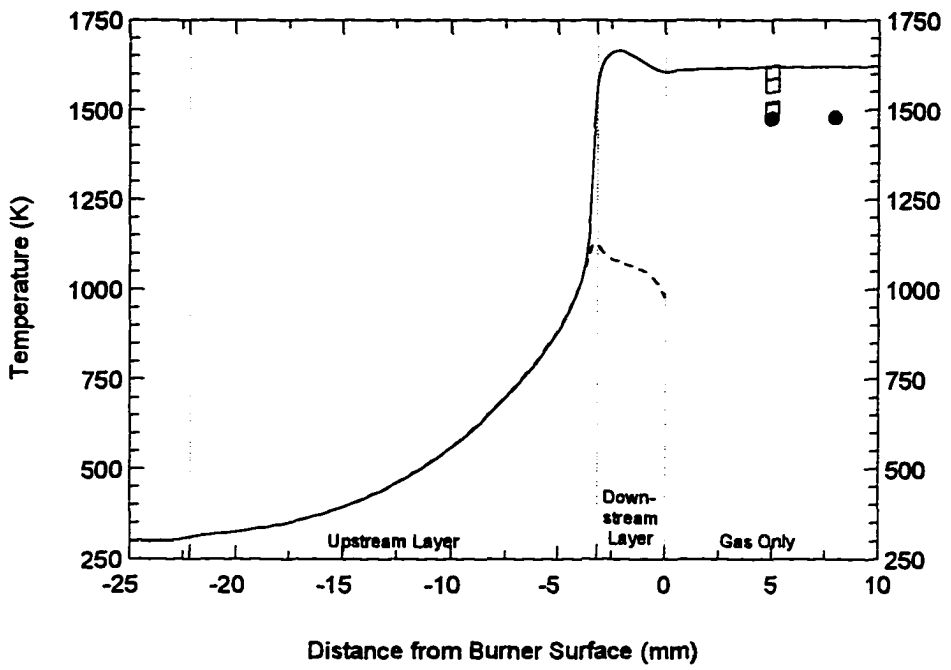

Figure 6-13: Predicted and measured gas temperatures at a firing rate of 315 kW/m2 and ϕ = 0.9. Solid line is predicted gas temperature; dashed line is predicted porous medium temperature; squares are optically measured temperatures; circles are the corrected thermocouple measurements. For comparison, the adiabatic flame temperature of a ϕ=0.9 CH_4-air flame is 2137 K.

Figure 6-13 shows temperature predictions and measurements for a firing rate of 315 kW/m^2 and ϕ=0.9. The figure shows that the flame is stabilized near the interface of the two layers and that significant gas preheating occurs before the reaction zone. LIF thermometry and corrected thermocouple measurements made 5-mm above the burner are shown as squares and a circle, respectively. The predicted temperature of the gas at 5 mm is 1620 K. For reference, an

adiabatic flame at the same equivalence ratio ($\phi = 0.9$) would have a temperature of over 2100 K. The temperatures determined with LIF are slightly higher than the measurements of the thermocouples. Possible reasons for the deviation are mentioned above.

6.4.6 Influence of Porous Medium Properties on Exit Gas Temperature

Computations were performed to determine the sensitivity of exit gas temperature to the thermal and heat transfer properties of the porous medium. For the upstream and downstream layer, each of the following porous medium properties was varied by ±30%: single scattering albedo (ω_1 and ω_2), extinction coefficient ($\sigma_{e,1}$ and $\sigma_{e,2}$), pore diameter (d_{p_1} and d_{p_2}), porosity (ε_1 and ε_2), and forward scattering fraction (f_1 and f_2).

As seen in Figure 6-14, the dominant parameter is the pore diameter of the downstream layer (d_{p_2}). In the model, the pore diameter is one of the parameters used to calculate the convective heat transfer coefficient. In an actual porous medium, though, the pore diameter influences the extinction coefficient and the effective thermal conductivity. The scattering albedo of the downstream or upstream layer has a significant effect near values of $\omega = 1.0$, that is, when *all* extinction of radiant energy is through scattering. A scattering albedo of 1.0 is probably an unattainable value for these materials. The influence of the remaining properties is quite small. The lines are intentionally unlabeled in

Figure 6-14 to emphasize the insignificance of these properties in determining the exit temperature. A slight misestimation of the heat transfer in the downstream layer has large effects on the gas temperature prediction.

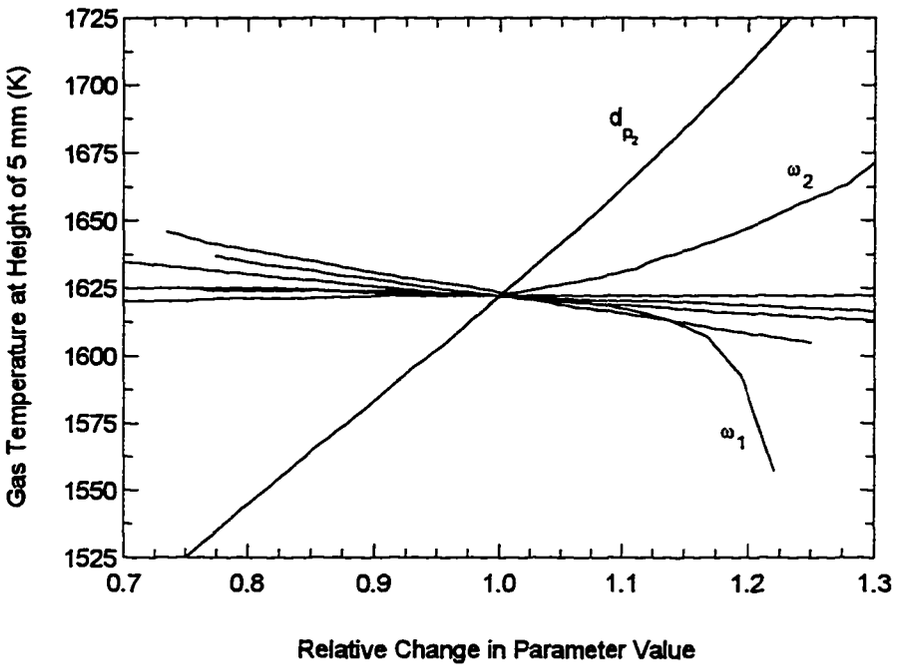

Figure 6-14: The influence of burner properties on exit gas temperature. The unlabeled lines correspond to results for variation of $\sigma_{e,1}$, $\sigma_{e,2}$, d_{p_1}, ε_1, and ε_2. q = 315 kW/m², ϕ = 0.9.

6.4.7 Surface Reactions in the Upstream Layer

Given the small pore size in the upstream layer (~0.1 mm), surface reactions remain a distinct possibility. One type of possible surface reactions is the recombination of radical on the surface of the porous medium. This recombination type is simulated by increasing the reaction rate of three-body reactions and assumes that the third body is the surface of the porous medium.

For a generic three-body reaction A + B + M → AB + M, the rate-of-progress variable for the i-th reaction q_i can be written as

$$q_i = \left(\sum_{k=1}^{K}(\alpha_{ki})[X_k]\right)\left(k_{f_i}\prod_{k=1}^{K}[X_k]^{\nu'_{ki}} - k_{r_i}\prod_{k=1}^{K}[X_k]^{\nu''_{ki}}\right) \qquad [6\text{-}1]$$

where α_{ki} is the third-body efficiency of the k-th species, k_{f_i} is the forward rate of the i-th reaction, X_k is the mole fraction of the k-th species, ν_{ki}' is the coefficient for the k-th species of the reactants in the i-th reaction , ν_{ki}'' is the coefficient for the k-th species of the products in the i-th reaction , and k_{r_i} is the reverse rate of the i-th reaction. This expression is the two body reaction, but is modified by the first term in parentheses to account for the third-body efficiency.

The values of α_{ki} were uniformly increased in the upstream porous layer to simulate increased importance for the three body reactions. As the third-body efficiencies in the upstream layer increased, the flame moved downstream, which resulted in an increased exit temperature. Thus, we conclude that surface reactions in the upstream layer through three-body recombination are not the cause of the gas temperature overprediction.

6.5 RADIANT EFFICIENCY IN SUBMERGED-FLAME BURNERS

The radiant efficiency of the submerged-flame burner in this chapter has been measured by Mital *et al.* (1995) for a variety of flow rates and stoichiometries. Figure 6-15 shows predictions and measurements for $\phi = 0.9$. The experimental

data include two burner configurations: a 14-cm square porous medium and a 7.5-cm diameter porous medium. The model does not predict the downturn in radiant efficiency that occurs at a firing rate below about 200 kW/m^2. This discrepancy is a most likely a result of heat losses to the burner housing and gas radiation, which are not included in the model. Heat losses to the burner housing and gas radiation become important at low firing rates because the flame is weak. Also, the convective heat transfer coefficient in the downstream layer becomes more important as the flame becomes weaker and prone to stabilizing outside of the porous medium (i.e. surface-flame mode). For most stable regimes, though, the model predicts the radiant efficiency quite accurately. Note that at $\phi = 0.9$ the radiant efficiency of the submerged-flame burner (about 30% at 300 kW/m^2 and about 25% at 600 kW/m^2) is far higher than the radiant efficiency for a surface-flame burner (about 20% at 300 kW/m^2 and about 10% at 600 kW/m^2).

The model is less successful when the equivalence ratio is varied, as shown in Figure 6-16. The deviation is largest at low equivalence ratios, where heat losses to the burner housing become important. Nevertheless, the model clearly predicts the trend and the maximum deviation is only about 25%.

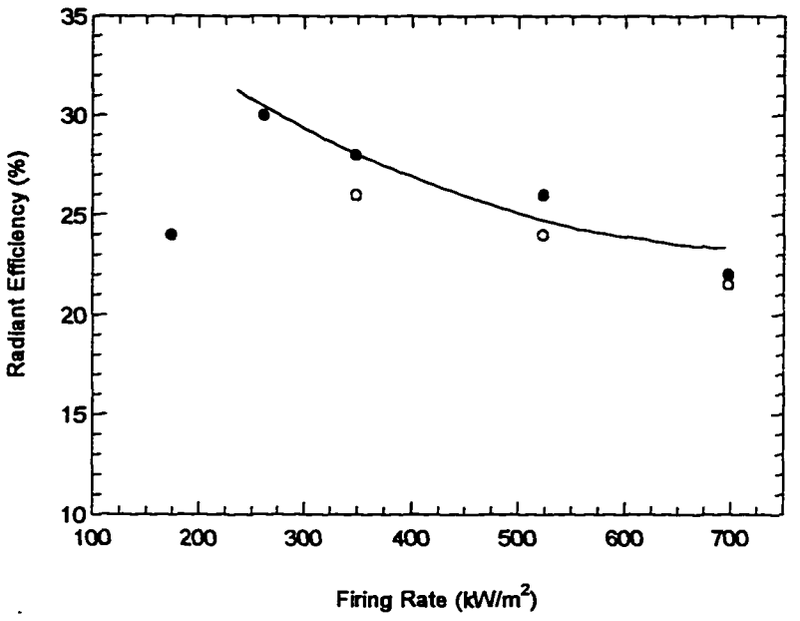

Figure 6-15: Radiant efficiency predictions and measurements for the submerged-flame burner. Solid circles are for a 14-cm square burner, open circles are for a 7.5-cm diameter circular porous medium. $\phi = 0.9$.

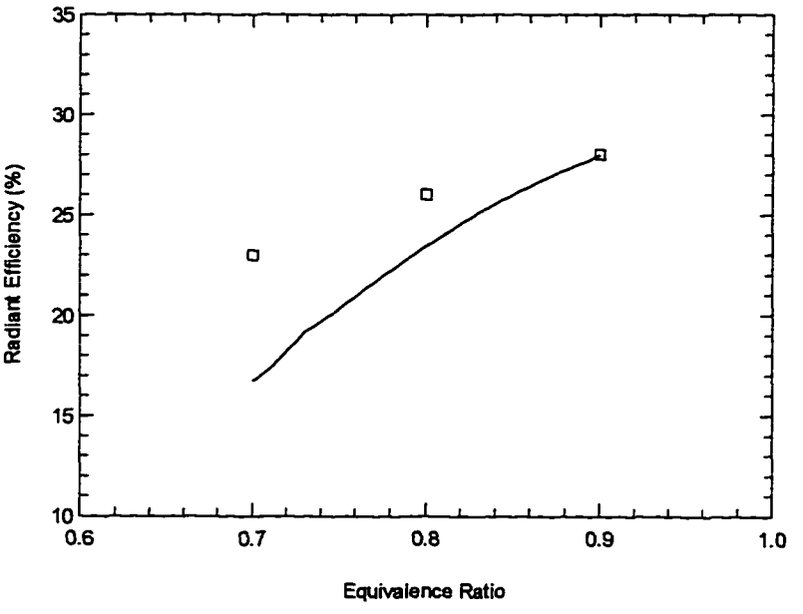

Figure 6-16: Radiant efficiency for the submerged-flame burner (with 14-cm square porous medium) as a function of equivalence ratio. The firing rate is 349 kW/m².

The same multiple parameter variation procedure as in Section 6.4.6 was performed to determine which burner properties have the largest influence on radiant efficiency. Figure 6-17 shows the results of the calculations: the pore diameter of the downstream layer (d_{p_2}) has the greatest influence. Thus, to improve radiant efficiency of the radiant burner, efforts should be focused on the convective heat transfer in the downstream layer. However, excess heat transfer in the downstream layer may lead to flashback, a phenomenon that is also controlled by the properties of the upstream layer. A simple study of flashback in submerged-flame burners was performed by Mital *et al.* (1995).

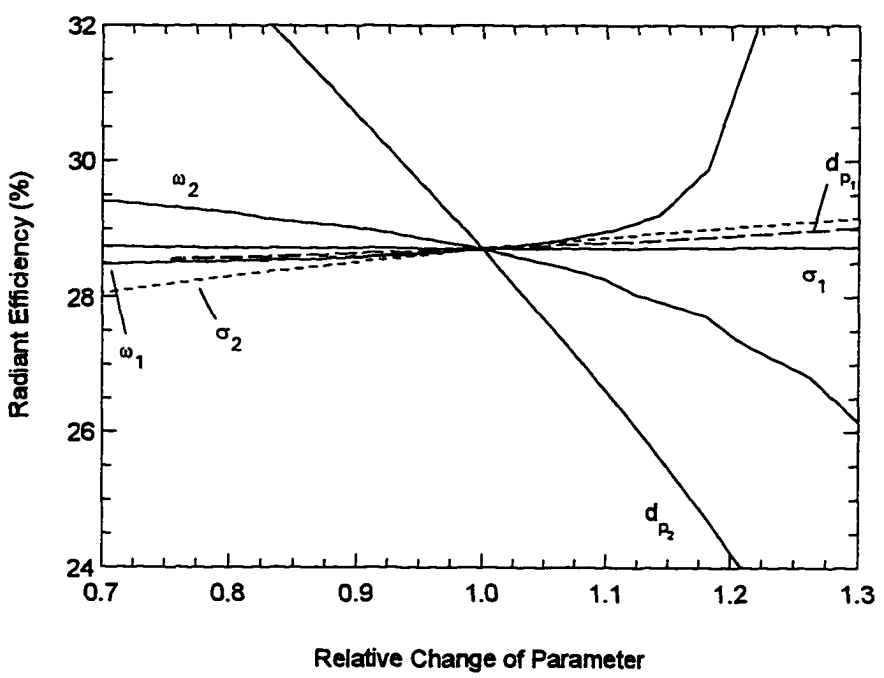

Figure 6-17: The influence of burner parameters on radiant efficiency at ϕ = 0.9 and q = 315 kW/m².

6.6 NO_X FORMATION IN SUBMERGED-FLAME BURNERS

An analysis of NO_x formation in submerged-flame burners is presented in this section. As in Chapter 4 for the surface-flame burner, nearly all of the NO_x is emitted as NO. The method of calculating the contribution from each NO formation mechanism is similar to that for surface-flame burners (see Section 4.3), in which the reaction rate of each NO pathway is integrated to calculate the NO contribution. The chemical mechanism in the simulation is GRI-Mech 2.11 (Bowman *et al.*, 1995). Five NO formation mechanisms are considered: 1.) the Fenimore pathway, 2.) the extended Zeldovich mechanism, 3.) the N_2O mechanism, 4.) the NNH mechanism, and 5.) the remaining reactions in the mechanism that produce NO. Three firing rates (200, 300 and 600 kW/m^2) at ϕ = 0.9 are examined.

The results for 200 kW/m^2 are similar to those for a surface-flame burner at the same firing rate and stoichiometry, as shown in Figure 6-18. Each NO formation mechanism contributes a roughly equal amount to the total. Nearly all of the NO is formed in the flame front.

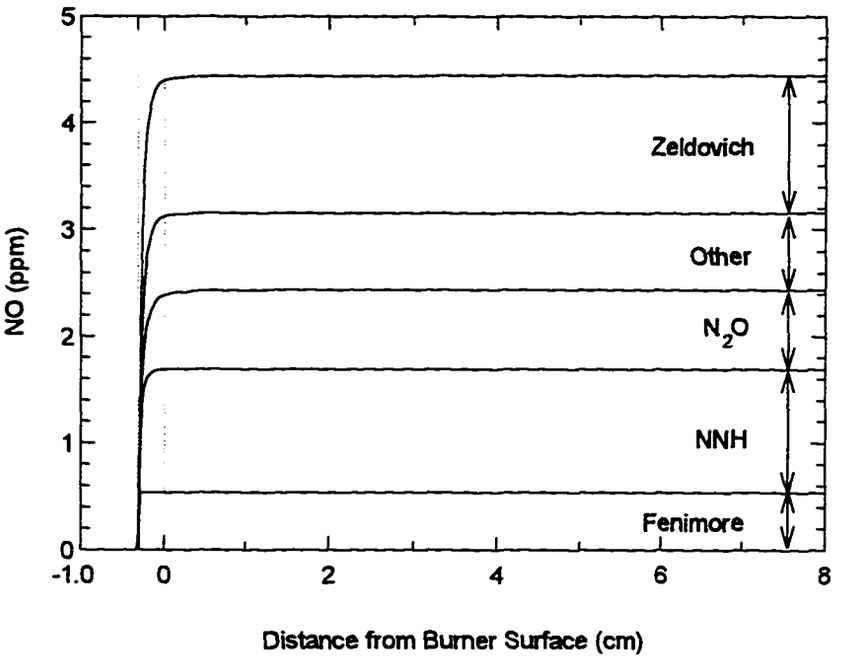

Figure 6-18: NO contributions from each mechanism and the combined NO concentration. The firing rate is 200 kW/m² and $\phi = 0.9$. The uppermost solid line is the total NO; the lower lines delineate the contribution from each mechanism. The peak gas temperature is 1604 K (inside the downstream layer at x = -0.23 cm) and the exit gas temperature is 1522 K.

At a firing rate of 300 kW/m², the NO formation is similar to that of the 200 kW/m² firing rate, as seen in Figure 6-19. This is in contrast to the results for surface-flame burners, which showed that the non-flame Zeldovich mechanism was moderately active at $q = 300$ kW/m² and $\phi = 0.9$.

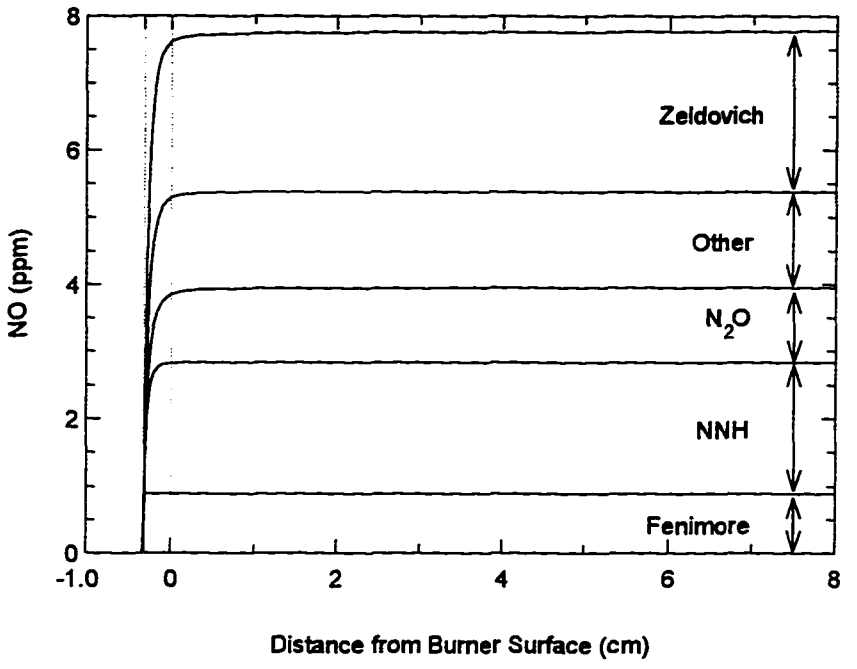

Figure 6-19: NO contributions from each mechanism and the combined NO concentration. The firing rate is 300 kW/m² and $\phi = 0.9$. The uppermost solid line is the total NO; the lower lines delineate the contribution from each mechanism. The peak gas temperature is 1690 K (inside the downstream layer at x = -0.22 cm) and the exit gas temperature is 1606 K.

Compared to the surface-flame burner of Chapter 3, the NO formation mechanism for the submerged-flame burner is strikingly different at 600 kW/m², as seen in Figure 6-20. The primary difference is that the gas temperature is significantly lower in the submerged-flame burner than in the surface-flame burner (1780 K vs. 1922 K) because of the larger heat transfer area between the combustion gases and the porous medium.

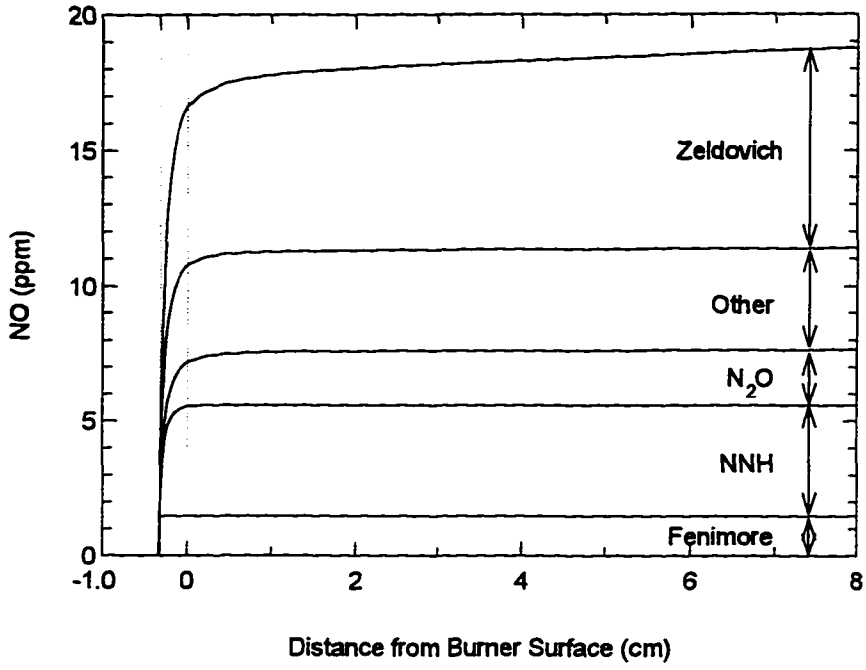

Figure 6-20: NO contributions from each mechanism and the combined NO concentration. The firing rate is 600 kW/m² and $\phi = 0.9$. The uppermost solid line is the total NO; the lower lines delineate the contribution from each mechanism. The peak gas temperature is 1820 K (inside the downstream layer at x = -0.21 cm) and the exit gas temperature is 1780 K.

6.7 CONCLUSIONS

Flame structure predictions and measurements for a submerged-flame burner at three firing rates show that almost all of the methane is consumed within the porous medium, the concentration peaks of radicals are inside the porous medium, and nearly all of the NO forms near the flame front. The model predicts the concentration of the major species and the gas temperature in the downstream layer reasonably well.

The corrected thermocouple measurements are slightly below the results achieved by LIF thermometry. Use of a thermocouple in a straight two-hole ceramic sleeve can lead to faulty measurements. The model prediction is slightly higher than the temperatures determined with both methods. The strongest factor for the gas temperature at the exit of the porous medium is the pore diameter of the downstream layer. Other properties of the porous medium have much smaller influence.

The model accurately predicts the radiant efficiency of the submerged-flame burner over a variety of firing rates and stoichiometries, except at firing rates below approximately 200 kW/m^2. The porous medium property with the strongest influence on radiant efficiency is the pore diameter of the downstream layer.

Each NO formation mechanism contributes significantly to the total NO production in the submerged-flame burner at the three firing rates studied (200, 300, and 600 kW/m^2 at $\phi = 0.9$).

6.8 REFERENCES

American Society for Testing and Materials (1981), *Manual on the Use of Thermocouples in Temperature Measurement*,3rd ed., sponsored by ASTM Committee E-20 on Temperature Measurement and Subcommittee E-20.04 on Thermocouples (Philadelphia).

Ang, J.A., Pagni, P.J., Mataga, T.J., Margle, J.M., and Lyons, V.J. (1988), "Temperature and Velocity Profiles in Sooting Free Convection Diffusion Flames", *AIAA Journal* 26, pp. 323-329.

Bowman, C.T., Hanson, R.K., Davidson, D.F., Gardiner, Jr., W.C., Lissianski, V., Smith, G.P., Golden, D.M., Frenklach, M. and Goldenberg, M. (1995), GRI-Mech 2.11, http://www.me.berkeley.edu/gri_mech/

Crosley, D.R. and Jeffries, J.B. (1992), in *Temperature: Its Measurement and Control in Science and Industry* (J.F. Schooley, Ed.), American Institute of Physics, New York, Vol. 6, p. 701.

Desgroux, P., Gasnot, L., Pauwels, J.F., Sochet, L.R. (1995), "Correction of LIF Temperature Measurements for Laser Absorption and Fluorescence Trapping in a Flame. Application to the Thermal Perturbation Study Induced by a Sampling Probe", *Applied Physics B* 61, pp. 401-407.

Echigo, R. (1985), "Radiative Heat Transfer Enhancement to a Water Tube by Combustion Gases in Porous Medium", *Proceedings: International Symposium on Heat Transfer*, Vol. 3, pp. 186-193.

Holman, J.P. (1990), *Heat transfer*, 7th ed., McGraw-Hill (New York).

Hsu, P.-F., Evans, W.D., and Howell, J.R. (1993), "Experimental and Numerical Study of Premixed Combustion within Nonhomogenous Porous Ceramics", *Combustion Science and Technology* 90, pp. 149-172.

Merriam-Webster Inc. (1987), *Webster's Ninth New Collegiate Dictionary*, Merriam-Webster, Inc. Publishers (Springfield, MA).

Mital, R., Gore, J.P., Viskanta, R., and Singh, S. (1995), "Global Radiation and Emission Characteristics of Reticulated Ceramic Radiant Burners", in *Proceedings of 1995 Joint Thermal Meeting on Combustion Fundamentals and Applications* (J.P. Gore, Ed.), Central and Western States and Mexican National sections of the Combustion Institute, pp. 32-37.

Mital, R., Gore, J.P., Viskanta, R., and Singh, S. (1996), "Structure of Submerged Flames in Reticulated Ceramic Radiant Burners", 1996 Technical Meeting of the Central States Section of the Combustion Institute, St. Louis.

Morgan, V.T. (1975), in *Advances in Heat Transfer* (T.F. Irvine and J.P. Hartnett, Ed.), Vol. 11, Academic Press (New York), p. 199.

Nguyen, Q.V., Edgar, B.L., Dibble, R.W., and Gulati, A. (1995), "Experimental and Numerical Comparison of Extractive and In Situ Laser Measurements of Non-Equilibrium Carbon Monoxide in Lean-Premixed Natural Gas Combustion", *Combustion and Flame* 100 (3), pp. 395-406.

Rensberger, K.J., Jeffries, J.B., Copeland, R.A., Kohse-Höinghaus, K., Wise, M.L., and Crosley, D.R. (1989), "Laser-Induced Fluorescence Determination of Temperatures in Low Pressure Flames", *Applied Optics* 28, pp. 3556-3566.

Rumminger, M.D., Heberle, N.H., Dibble, R.W. and Crosley, D.R. (1996), "Gas Temperature above a Porous Radiant Burner: Comparison of Measurements and Model Predictions", *Twenty-Sixth International Symposium on Combustion*, The Combustion Institute, Pittsburgh.

Siegel, R. and Howell, J.R. (1992), *Thermal Radiation Heat Transfer*, 3rd ed., Hemisphere Publishing Corp. (Washington, D.C.).

Weinberg, F.J. (1974), "The First Half-Million Years of Combustion Research and Today's Burning Problems", *Fifteenth Symposium (International) on Combustion*, The Combustion Institute, Pittsburgh, pp. 1-17.

CHAPTER 7

Summary and Conclusions

7.1 SUMMARY

This dissertation has examined three related types of porous direct-fired radiant burners: the surface-flame burner, the surface-flame burner with screen, and the submerged-flame burner. A one-dimensional model with multistep chemistry, a non-anchored flame, a radiatively participating porous medium, heat transfer between the gas and porous medium, conduction in the gas and conduction in the porous medium was developed and used to simulate radiant burner operation. Flame structure, radiant efficiency and pollutant formation were examined for each burner type.

The three burners in this dissertation can be viewed as an evolution. The first burner examined was the surface-flame burner, in which heat transfer between the combustion gases and porous medium occurs from the upstream edge of the flame. The next burner was the surface-flame burner with screen, which was similar to the surface-flame burner, but with additional heat transfer

from downstream of the flame (the combustion products) to the screen. The screen radiates part of the additional heat transfer to the load and part back to the surface-flame burner. Finally, the surface-burner and screen were brought together to form a submerged-flame burner.

7.2 CONCLUSIONS

7.2.1 Surface-flame Burners

Surface-flame burners have been simulated with a reduced methane mechanism that compares favorably with the full methane mechanism. A parametric study of radiant efficiency in surface-flame burners showed that the following changes lead to maximum radiant efficiency: high extinction coefficient, low albedo, low thermal conductivity, high porosity, and large thickness. Porous medium properties have limited influence on radiant efficiency because the amount of heat transferred from the flame to the porous medium is nearly constant for all porous medium properties. Radiant efficiency depends primarily on the stabilization characteristics of a premixed flame, which is a strong function of equivalence ratio and firing rate. Differences in radiant efficiency for porous media with different properties are the result of heat redirection inside the porous medium. A highly efficient burner will convert all of the heat transferred from the gas into forward propagating radiation.

NO_x emissions from surface-flame burners are relatively low. Our simulations of surface-flame burners show that Zeldovich NO is dominant only at high firing rates (above about 600 kW/m^2 at $\phi = 0.9$). At lower firing rates, nearly all of the NO_x is formed in the flame front, with each of the major NO_x mechanisms playing an important role.

Burner design has little impact on NO_x emissions for burners operating at low firing rate because changes in burner design do not cause significant temperature changes.

7.2.2 Surface-flame Burners with Screens

For a surface-flame burner with screen, the largest radiant efficiency gains are found for the highest firing rates and lowest equivalence ratios studied. Radiative feedback from the screen also causes the flame to propagate deeper into the porous medium. The temperature of the combustion products drops as they pass through the screen, significantly reducing the NO_x formation rate, especially at high firing rates where the Zeldovich NO_x mechanism is dominant. For screens that are 1 cm or farther from the burner surface, the CO burnout process is not interrupted. Highest radiant efficiency and lowest NO_x emissions are obtained when the screen is composed of tightly-spaced cylinders which are placed close to the burner.

7.2.3 Submerged-flame Burners

Flame structure predictions by a one-dimensional model of a submerged-flame burner agree favorably with measurements. Corrected thermocouple measurements are slightly below the results achieved by OH-LIF thermometry. The model prediction is slightly higher than the temperatures determined with each method. Computations show that the outlet gas temperature and radiant efficiency are most dependent on convective heat transfer between gas and solid in the downstream layer of the porous medium. At each firing rate studied (150, 300, and 600 kW/m^2), nearly all of the NO_x is formed in the flame front, with each of the major NO_x mechanisms playing an important role.

7.3 PROSPECTS FOR RADIANT EFFICIENCY IMPROVEMENT

Roughly speaking, surface-flame burners have a lower radiant efficiency by a factor of 1.5 to 2 than surface-flame burners with screens or submerged-flame burners. We have shown that the properties of the porous medium have limited effect on the radiant efficiency of a surface-flame burner. Changes in the properties of the porous medium of a surface-flame burner will not improve the radiant efficiency to that of a surface-flame burner with screen or submerged-flame burner. Thus, efforts to improve surface-flame burner performance should be limited to tuning the spectral emission of the burners and improving the stable operating range.

Improvements in radiant efficiency are likely for the surface-flame burner with screen and the submerged-flame burner. However, issues of material lifetime and flame stability are currently unresolved for all types of porous direct-fired radiant burners.

7.4 FUTURE CHALLENGES

7.4.1 Modeling

Numerous challenges await modelers of radiant burners. Inclusion of gas radiation, though not a critical element, will improve modeling of NO_x formation in surface-flame burners with high firing rates and surface-burners with screens.

The benefits of partially catalytic radiant burners appear to be significant and some modeling has been performed (Rumminger *et al.*, 1996). Much research remains to be done, especially in the area of detailed surface chemistry, mass transfer to the solid surfaces in the porous medium, and catalyst durability.

As mentioned in the previous section, improving the operating range of porous direct-fired radiant burners is an important area of research. For surface-flame burners, flame lift-off occurs at very low and very high firing rates. For submerged-flame burners, at low firing rates the flame moves out of the porous medium (the burner becomes a surface-flame burner), but at high firing rates flashback occurs. Modeling of these multi-dimensional and transient

phenomena could improve burner designs and result in a wider operating range for porous direct-fired radiant burners.

Emission of CO from radiant burners was not extensively discussed in this dissertation, primarily because CO emission reductions are not a pressing issue for radiant burners. Additionally, experimental analysis of CO formation is undergoing an evolution as new techniques for CO measurement are developed (Nguyen *et al.*, 1995). Future work on CO formation, especially in the downstream layer of submerged-flame burners and for surface-burners with screens would be useful.

The radiation network method of analyzing multiple objects above a surface-flame or submerged-flame burner that was presented in Chapter 5 holds great promise for simulation of industrial processes. The model allows a flexible definition of the burner and load.

7.4.2 Experiments

From the analysis in this dissertation, we conclude that the accurate knowledge of porous medium properties is not critical for prediction of the radiant efficiency of surface-flame burners . An accurate chemical kinetic mechanism, though, is critical for radiant efficiency prediction. For prediction of flame stability, surface temperature and quantitative NO_x emissions, the properties of the porous medium are important. For example, a surface-flame burner can

flash-back if the extinction coefficient or convective heat transfer coefficient is too low.

One of the unresolved issues related to surface-flame burners is partial flame lift-off, a situation when a portion of the flame lifts from the porous medium surface. It remains to be demonstrated whether unevenness in the gas flow or non-uniformity of the porous medium is the major cause of partial flame lift-off.

Porous medium properties for submerged-flame burners, in contrast, are extremely important for both radiant efficiency and flame stability. Additional measurements of the convective heat transfer properties and radiative properties of the downstream layers of porous media in submerged-flame burners could improve the accuracy of submerged-flame burner models.

Experimental measurements of heat transfer from the porous medium to the burner housing would be a valuable addition to the current collection of experimental data.

7.5 REFERENCES

Nguyen, Q.V., Edgar, B.L., Dibble, R.W., and Gulati, A. (1995), "Experimental and Numerical Comparison of Extractive and In Situ Laser Measurements of Non-Equilibrium Carbon Monoxide in Lean-Premixed Natural Gas Combustion", *Combustion and Flame* 100 (3), pp. 395-406.

Rumminger, M.D., Hamlin, R.D., and Dibble, R.W. (1996), "Numerical Analysis of a Catalytic Radiant Burner: The Effect on Radiant Efficiency and Operability", Third International Workshop on Catalytic Combustion, Amsterdam, to appear in *Catalysis Today*.

Complete List of References for Dissertation

American Society for Testing and Materials (1981), *Manual on the Use of Thermocouples in Temperature Measurement*, 3rd ed., sponsored by ASTM Committee E-20 on Temperature Measurement and Subcommittee E-20.04 on Thermocouples (Philadelphia).

Andersen, F. (1992), "Heat Transport Model for Fibre Burners", *Progress in Energy and Combustion Science* 18, pp. 1-12.

Ang, J.A., Pagni, P.J., Mataga, T.J., Margle, J.M., and Lyons, V.J. (1988), "Temperature and Velocity Profiles in Sooting Free Convection Diffusion Flames", *AIAA Journal* 26, pp. 323-329.

Anonymous (1991), "Infrared Paint Curing Heats Up", *Manufacturing Engineering* 106(1), p. 22.

Bartz, D.F., Moreno, F.E., and Duggan, P.A. (1992), "Ultra-low NO_x Ultra-High *VOC* Destruction with Adiabatic Radiant Combustors", in *Fossil Fuel Combustion* (Roberto Ruiz, Ed.), ASME PD-39, pp. 7-12.

Blevins, L.G., Sivathanu, Y.R., Shahien, M.A., and Gore, J.P. (1994), "A Study of Global Properties of Radiant Tube Flames", *Proceedings of the First ISHMT-ASME Heat and Mass Transfer Conference and Twelfth National Heat and Mass Transfer Conference*, Tata McGraw-Hill (New Delhi), January 5-7, Bombay, India.

Blevins, L.G. and Gore, J.P. (1996), "Radiative Efficiency of a Quartz Radiant Heating Tube", *Combustion Science and Technology* 112, pp. 369-374.

Bouma, P.H., Eggels, R.L.G.M., Somers, L.M.T., de Goey, L.P.H., Nieuwenhuizen, J.K., and van der Drift, A. (1995), "A Numerical and Experimental Study of the NO-Emission of Ceramic Foam Surface Burners", *Combustion Science and Technology* 108 (1-3), pp. 193-203.

Bouma, P.H., Somers, L.M.T., de Goey, L.P.H., and Nieuwenhuizen, J.K. (1994), "Modelling of Methane-Air Combustion on Ceramic Foam Surface Burners in the Radiation Mode", presented at the Eurotherm Seminar number 37 'Heat Transfer in Radiating and Combusting Systems-2', Saluggia, Italy, 5-7 October.

Bowman, C.T., Hanson, R.K., Davidson, D.F., Gardiner, Jr., W.C., Lissianski, V., Smith, G.P., Golden, D.M., Frenklach, M., and Goldenberg, M. (1995), GRI-Mech 2.11, http://www.me.berkeley.edu/gri_mech/

Bozzelli, J.W. and Dean, A.M. (1995), "O+NNH - A Possible New Route for NO_x Formation in Flames", *International Journal of Chemical Kinetics* 27, pp. 1097-1109.

Chen, Y.-K., Matthews, R.D., and Howell, J.R. (1987), "The Effect of Radiation on the Structure of Premixed Flame within a Highly Porous Inert Medium", in *Radiation, Phase Change Heat Transfer and Thermal Systems* (Y. Jaluria *et al.*, Ed.), ASME HTD-81, pp. 35-41.

Coltrin, M.E., Kee, R.J., Evans, G.H., Meeks, E., Rupley, F.M., and Grcar, J.F. (1991), A Fortran Program for Modeling One-Dimensional Rotating-Disk/Stagnation-Flow Chemical Vapor Deposition Reactors, Sandia National Laboratory, SAND91-8003.

Crosley, D.R. and Jeffries, J.B. (1992), in *Temperature: Its Measurement and Control in Science and Industry* (J.F. Schooley, Ed.), American Institute of Physics, New York, Vol. 6, p. 701.

Desgroux, P., Gasnot, L., Pauwels, J.F., and Sochet, L.R. (1995), "Correction of LIF Temperature Measurements for Laser Absorption and Fluorescence Trapping in a Flame. Application to the Thermal Perturbation Study Induced by a Sampling Probe", *Applied Physics B* 61, pp. 401-407.

Echigo, R. (1982), "Effective Energy Conversion Method Between Gas Enthalpy and Thermal Radiation and Application to Industrial Furnaces", in *Proceedings of the 7th International Heat Transfer Conference*, Hemisphere Publishing Corp. (Washington, D.C.), Vol. VI, p. 361.

Echigo, R. (1985), "Radiative Heat Transfer Enhancement to a Water Tube by Combustion Gases in Porous Medium", *Proceedings: International Symposium on Heat Transfer*, Vol. 3, pp. 186-193.

Echigo, R. (1986), "High Temperature Heat Transfer Augmentation", in *High Temperature Heat Exchangers* (A.E. Sheidlin and N. Afghan, Ed.), Hemisphere Publishing Corporation (Washington, D.C.), pp. 230-259.

Echigo, R. and Yoshida, H. (1988), "High Temperature Heat and Mass Transfer in Porous Media", in *Experimental Heat Transfer, Fluid Mechanics, and Thermodynamics 1988* (R.K. Shah, E.N. Ganic, and K.T. Yang, Ed.), Elsevier Science Publishing Co., Inc. (Amsterdam), pp. 645-652.

Escobedo, F. and Viljoen, H.J. (1994), "Modeling of Porous Radiant Burners with Large Extinction Coefficients", *Canadian Journal of Chemical Engineering* 72(5), pp. 805-814.

Fenimore, C.P. (1970), "Formation of Nitric Oxide in Premixed Hydrocarbon Flames", *Thirteenth Symposium (International) on Combustion*, The Combustion Institute, Pittsburgh, pp. 373-380.

Flagan, R.C. and Seinfeld, J.H. (1988), *Fundamentals of Air Pollution Engineering*, Prentice-Hall, Inc. (Englewood Cliffs, NJ).

Frenklach, M. (1991), "Reduction of Chemical Reaction Models," in *Numerical Approaches to Combustion Modeling* (E. S. Oran and J. P. Boris, Ed.), Progress in Astronautics and Aeronautics, Vol. 135, American Institute of Aeronautics and Astronautics, Washington, D.C., pp. 129-154.

Fristrom, R.M. (1995), *Flame Structure and Processes*, Oxford University Press (New York).

Gnielinski, V., Zukauskas, A., and Skrinska, A. (1990), "Banks of Plain and Finned Tubes", in *Hemisphere Handbook of Heat Exchanger Design* (G.F. Hewitt, Ed.), Hemisphere Publishing Corporation (New York).

Golombok, M., Prothero, A., Shirvill, L.C., and Small, L.M. (1991), "Surface Combustion in Metal Fibre Burners", *Combustion Science and Technology* 77, pp. 203-223.

Goovaerts, J., Ratnani, K., and Hendry, B. (1991), "Infrared Applications in Pulp Drying", *Pulp and Paper Canada* 92(11), pp. 24-27.

Grcar, J.F. (1992), The Twopnt Program for Boundary Value Problems, Sandia National Laboratory, SAND91-8230.

Hall, M.J. and Hiatt, J.P.(1994), "Exit Flows from Highly Porous Media," *Physics of Fluids* 6(2), pp. 469-479.

Harder, R.F., Viskanta, R., and Ramadhyani, S. (1987), "Gas-Fired Radiant Tubes: A Review of the Literature", Gas Research Institute Report, GRI-87/0343.

Hendricks, T.J. and Howell, J.R. (1994a), "Absorption/Scattering Coefficients and Scattering Phase Functions in Reticulated Porous Ceramics", in *Radiative Heat Transfer: Current Research*(Y. Bayazitoglu *et al.*, Ed.), HTD-276, pp. 105-113, *AIAA/ASME Heat Transfer Conference*, Colorado Springs, June.

Holman, J.P. (1990), *Heat transfer*, 7th ed., McGraw-Hill (New York).

Howell, J.R., Hall, M.J. and Ellzey, J.L. (1995), "Combustion within Porous Inert Media", in *Heat Transfer in Porous Media and Two-Phase Flow*, (Y. Bayazitoglu and U.B. Sathuvalli, Ed.), ASME HTD-302, pp. 1-28.

Hsu, P.-F. and Matthews, R.D. (1993), "The Necessity of Using Detailed Kinetics in Models for Premixed Combustion in Porous Media", *Combustion and Flame*, 93 (4), pp. 457-466.

Hsu, P.-F., Evans, W.D., and Howell, J.R. (1993), "Experimental and Numerical Study of Premixed Combustion within Nonhomogenous Porous Ceramics", *Combustion Science and Technology* 90, pp. 149-172.

Hsu, P.F. and Howell, J.R. (1993), "Measurements of Thermal Conductivity and Optical Properties of Porous Partially Stabilized Zirconia, *Experimental Heat Transfer* 5, pp. 293-313.

Incropera, F.P. and DeWitt, D.P. (1990), *Fundamentals of Heat and Mass Transfer*, 3rd ed., John Wiley & Sons (New York).

Kanury, A. M. (1988), *Introduction to Combustion Phenomena*, 5th ed., Gordon and Breach (New York).

Kaplan, M. and Hall M.J. (1995), "The Combustion of Liquid Fuels within a Porous Media Radiant Burner", *Experimental Thermal and Fluid Science* 11(1), pp. 13-20.

Kazakov, A. and Frenklach, M. (1994), *DRM-19*, http://www.me.berkeley.edu/drm/

Kee, R.J., Dixon-Lewis, G., Warnatz, J., Coltrin, M.E., and Miller, J.A. (1986), A Fortran Computer Package for the Evaluation of Gas-Phase, Multicomponent Transport Properties, Sandia National Laboratory, SAND86-8246.

Kee, R.J., Grcar, J.F., Smooke, M.D., and Miller, J.A. (1985), A Fortran Program for Modeling Steady Laminar One-Dimensional Premixed Flames, Sandia National Laboratory, SAND85-8240.

Kee, R.J., Rupley, F.M. and Miller, J.A. (1989), CHEMKIN-II: A Fortran Chemical Kinetics Package for the Analysis of Gas Phase Chemical Kinetics, Sandia National Laboratory, SAND89-8009B.

Kendall, R.M., DesJardin, S.T., Sullivan, J.D. (1992), *Basic Research on Radiant Burners*, Gas Research Institute Report number 92-7027-171.

Kennedy, L.A. and Ettefagh, J. (1991), "Passing Combustion Gases Through Multilayered Porous Surfaces to Enhance Radiative Heating", in *ASME/JSME Thermal Engineering Proceedings*, Vol. 5, p. 189-195.

Khanna, V., Goel, R., and Ellzey, J.L. (1994), "Measurements of Emissions and Radiation for Methane Combustion within a Porous Medium Burner", *Combustion Science and Technology* 99, pp. 133-142.

Kuang, H.D., Thibault, J., Chen, R., Grandjean, B.P.A. (1995), "Pilot Scale Investigation of IR Drying of Paper", *Tappi Journal* 78(7), pp. 129-137.

Kulkarni, M. (1996), "Experimental and Numerical Analysis of Radiant Surface Burners", Ph.D. dissertation, Arizona State University.

Kulkarni, M.R. and Peck, R.E. (1993), "Modeling Radiant Surface Burner Performance", 1993 Fall Meeting of the Western States Section of the Combustion Institute, Menlo Park, California, Paper WSCI 93-106.

Lavigne, D. (1990), "A High Efficiency Gas-Fired Infrared Dryer", *Appita Journal* 43 (4), pp. 258-259.

Lee, L. (1994), "Gas Infrared Drying: Update on Technology", *Pulp and Paper Canada* 95 (12), pp. 102-104.

Levinsky, H.B. (1989), "A Computational Study of the Behavior of Radiant Burners", International Gas Research Conference, Tokyo.

Lutz, A.E. (1992) *Senkin: A Fortran Program for Predicting Homogeneous Gas Chemical Kinetics with Sensitivity Analysis*, Sandia National Laboratory, SAND87-8248.

Lyons, J.W. (1985), *Fire*, Scientific American Library, W.H. Freeman and Company (New York).

Malte, P.C. and Pratt, D.T. (1974), "The Role of Energy-Releasing Kinetics in NO_x Formation: Fuel-Lean, Jet-Stirred CO-Air Combustion", *Combustion Science and Technology* 9, pp. 221.

Mantle, W.J. and Chang, W.S. (1991), "Effective Thermal Conductivity of Sintered Metal Fibers", *Journal of Thermophysics and Heat Transfer* 5 (4), pp. 545-549.

Mattsson, P., Pelkonen, J., Riikonen, A., and Oy, N. (1990), "Infrared Drying of Coated Paper", *Paperi ja Puu – Paper and Timber* 72, pp. 347-349.

Meng, W.H., McCordic, C., Gore, J.P., and Herold, K.E. (1991), "A Study of Effects of Porous Ceramic Inserts on Heat Transfer and Combustion in a Fired Heat Exchanger", in *ASME/JSME Thermal Engineering Proceedings*, Vol. 5, pp. 181-188.

Merriam-Webster Inc. (1987), *Webster's Ninth New Collegiate Dictionary*, Merriam-Webster, Inc. Publishers (Springfield, MA).

Miller, J. A. and Bowman, C. T. (1989), "Mechanism and Modeling of Nitrogen Chemistry in Combustion", *Progress in Energy and Combustion Science* 15, pp. 287-338.

Mital, R. and Gore, J.P. (1995), personal communication.

Mital, R., Gore, J.P., and Viskanta, R. (1995), "Measurements of Extinction Coefficient and Single Scattering Albedo of Reticulated Porous Ceramic at High Temperatures", AIAA Paper number 95-2036.

Mital, R., Gore, J.P., Viskanta, R., and Singh, S. (1995), "Global Radiation and Emission Characteristics of Reticulated Ceramic Radiant Burners", in *Proceedings of 1995 Joint Thermal Meeting on Combustion Fundamentals and Applications* (J.P. Gore, Ed.), Central and Western States and Mexican National sections of the Combustion Institute, pp. 32-37.

Mital, R., Gore, J.P., Viskanta, R., and Singh, S. (1996), "Structure of Submerged Flames in Reticulated Ceramic Radiant Burners", 1996 Technical Meeting of the Central States Section of the Combustion Institute, St. Louis.

Morgan, V.T. (1975), in *Advances in Heat Transfer* (T.F. Irvine and J.P. Hartnett, Ed.), Vol. 11, Academic Press (New York), p. 199.

Nguyen, Q.V., Edgar, B.L., Dibble, R.W., and Gulati, A. (1995), "Experimental and Numerical Comparison of Extractive and In Situ Laser Measurements of Non-Equilibrium Carbon Monoxide in Lean-Premixed Natural Gas Combustion", *Combustion and Flame* 100 (3), pp. 395-406.

Oppenheim, A.K. (1956), "Radiative Analysis by the Network Method", *Transactions of the ASME* 65, pp. 725-735.

Ramamurthy, H., Ramadhyani, S., and Viskanta, R. (1995) "A Thermal System Model for a Radiant-Tube Continuous Reheating Furnace", *Journal of Materials Engineering and Performance* 4 (5), pp. 519-531.

Rensberger, K.J., Jeffries, J.B., Copeland, R.A., Kohse-Höinghaus, K., Wise, M.L., and Crosley, D.R. (1989), *Applied Optics*, 28:3556-3566.

Rumminger, M.D., Hamlin, R.D., and Dibble, R.W. (1996), "Numerical Analysis of a Catalytic Radiant Burner: The Effect on Radiant Efficiency and Operability", Third International Workshop on Catalytic Combustion, Amsterdam, to appear in *Catalysis Today*.

Rumminger, M.D., Heberle, N.H., Dibble, R.W. and Crosley, D.R. (1996), "Gas Temperature above a Porous Radiant Burner: Comparison of Measurements and Model Predictions", *Twenty-Sixth International Symposium on Combustion*, The Combustion Institute, Pittsburgh.

Sakai, N. and Hanzawa, T. (1994), "Applications and Advances in Far-Infrared Heating in Japan", *Trends in Food Science and Technology* 5(11), pp. 357-362.

Sathe, S.B., Peck, R.E., and Tong, T.W. (1990), "A Numerical Analysis of Heat Transfer and Combustion in Porous Radiant Burners," *International Journal of Heat and Mass Transfer* 33, pp. 1331-1338.

Schlegel, A., Buser, S., Benz, P., Bockhorn, H., and Mauss, F. (1994), *Twenty-fifth Symposium (International) on Combustion*, The Combustion Institute, Pittsburgh, pp. 1019-1026.

Schweizer, S. and Sullivan, J. (1994), *CFCC Radiant Burner Assessment*, Alzeta Report No. 94-7607-193 (prepared for the U.S. Department of Energy), Santa Clara, CA.

Siegel, R. and Howell, J.R. (1992), *Thermal Radiation Heat Transfer*, 3rd ed., Hemisphere Publishing Corp. (Washington, D.C.).

Singh, S.N. (1996), Personal communication, January.

Singh, S., Ziolkowski, M., Sultzbaugh, J., and Viskanta, R. (1992), "Mathematical Model of a Ceramic Burner Radiant Heater", in *Fossil Fuel Combustion* (Roberto Ruiz, Ed.), ASME PD-33, pp. 111-116.

Sullivan, J.D., and Kendall, R.M. (1992), "Thermal Performance and NO_x emissions from Porous Surface Radiant Burners," International Gas Research Conference, Orlando, Florida.

Tidball, R.K., Donaldson, R.J. and Gotterba, J.A. (1989), *Radiant Burner Technology Base - Burner Research and Development*, Final Report, Alzeta Report No. 89/723-724/148, March.

Tong, T.W. and Li, W. (1995), "Enhancement of Thermal Emission from Porous Radiant Burners", *Journal of Quantitative Spectroscopy and Radiative Transfer* 53, pp. 235-248.

Tseng, C.-J. and Howell, J.R. (1996), "Combustion of Liquid Fuels in a Porous Radiant Burner", *Combustion Science and Technology* 112, pp. 141-163.

Turns, S.R. and Myhr, F.H. (1991), "Oxides of Nitrogen Emissions from Turbulent Jet Flames - 1. Fuel Effects and Flame Radiation", *Combustion and Flame* 87(3-4), pp. 319-335.

van der Drift, A., Beckers, G.J.J., Smit, K., Beesteheerde, J. (1994), "An Experimental and Numerical Study of Porous Radiant Burners", presented at the Eurotherm Seminar number 37 'Heat Transfer in Radiating and Combusting Systems-2', Saluggia, Italy, 5-7 October.

van Maaren, A., Thung, D.S., and De Goey L.P.H. (1994), "Measurement of Flame Temperature and Adiabatic Burning Velocity of Methane/Air Mixtures", *Combustion Science and Technology* 96 (4-6), pp. 327-344.

Viskanta, R. (1966), "Radiation Transfer and Interaction of Convection with Radiation Heat Transfer," in *Advances in Heat Transfer* (T.E. Irvine, Jr. and J.P. Hartnett, Ed.), Vol. 3, Academic Press (New York), pp. 176-252.

Viskanta, R. (1995) "Interaction of Combustion and Heat Transfer in Porous Inert Media", International Symposium on Transport Phenomena in Combustion (ISTP-8), July, San Francisco, CA.

Viskanta, R. (1995), "Convective Heat Transfer in Consolidated Porous Materials: A Perspective", presented at the Symposium on Thermal Science and Engineering in honor of Chancellor Chang-Lin Tien, November, Berkeley, CA.

Wang, H. and Frenklach, M. (1991), "Detailed Reduction of Reaction Mechanisms for Flame Modeling", *Combustion and Flame* 87, pp. 365-370.

Warnatz, J. (1992), "Resolution of Gas Phase and Surface Combustion into Elementary Reactions", *Twenty-Fourth Symposium (International) on Combustion*, The Combustion Institute, Pittsburgh.

Weinberg, F.J. (1974), "The First Half-Million Years of Combustion Research and Today's Burning Problems", *Fifteenth Symposium (International) on Combustion*, The Combustion Institute, Pittsburgh, pp. 1-17.

Williams, A., Woolley, R., and Lawes, M. (1992), "The Formation of NO_x in Surface Burners", *Combustion and Flame* 89, pp. 157-166.

Wolfrum, J. (1972), "Bildung von Stickstoffoxiden bei der Verbrennung", *Chemie Ingenieur Technik* 44, p. 656.

Yagi, S., Kunii, D. and Wakao, N. (1960), "Studies of Axial Effective Thermal Conductivities in Packed Beds", *AIChE Journal* 6, pp. 543-546.

Younis, L.B. and Viskanta, R. (1993), "Experimental Determination of the Volumetric Heat Transfer Coefficient between Stream of Air and Ceramic Foam", *International Journal of Heat and Mass Transfer* 36 (6), pp. 1425-1434.

Zeldovich, Y.B. (1946), "The Oxidation of Nitrogen in Combustion Explosions", *Acta Physiocochemica USSR* 21, p. 577.

APPENDIX

Chemical Mechanisms for Methane Combustion

REDUCED MECHANISM

DRM19

Developed by A. Kazakov and M. Frenklach (1994)

Mechanism available from
http://www.me.berkeley.edu/gri_mech/redmech.html/

21 species, 84 reactions

```
ELEMENTS     O  H  C  N  AR
SPECIES
H2       H        O        O2       OH       H2O      HO2
CH2      CH2(S)   CH3      CH4      CO       CO2      HCO
CH2O     CH3O     C2H4     C2H5     C2H6
N2       AR
END
```

	REACTIONS CONSIDERED			(k = A T**b exp(-E/RT)) A	b	E
1.	O+H+M<=>OH+M			5.00E+17	-1.0	0.0
	H2	Enhanced by	2.000E+00			
	H2O	Enhanced by	6.000E+00			
	CH4	Enhanced by	2.000E+00			
	CO	Enhanced by	1.500E+00			
	CO2	Enhanced by	2.000E+00			
	C2H6	Enhanced by	3.000E+00			
	AR	Enhanced by	7.000E-01			
2.	O+H2<=>H+OH			5.00E+04	2.7	6290.0
3.	O+HO2<=>OH+O2			2.00E+13	0.0	0.0
4.	O+CH2<=>H+HCO			8.00E+13	0.0	0.0
5.	O+CH2(S)<=>H+HCO			1.50E+13	0.0	0.0
6.	O+CH3<=>H+CH2O			8.43E+13	0.0	0.0

```
 7. O+CH4<=>OH+CH3                                    1.02E+09    1.5      8600.0
 8. O+CO+M<=>CO2+M                                    6.02E+14    0.0      3000.0
       H2                Enhanced by    2.000E+00
       O2                Enhanced by    6.000E+00
       H2O               Enhanced by    6.000E+00
       CH4               Enhanced by    2.000E+00
       CO                Enhanced by    1.500E+00
       CO2               Enhanced by    3.500E+00
       C2H6              Enhanced by    3.000E+00
       AR                Enhanced by    5.000E-01
 9. O+HCO<=>OH+CO                                     3.00E+13    0.0         0.0
10. O+HCO<=>H+CO2                                     3.00E+13    0.0         0.0
11. O+CH2O<=>OH+HCO                                   3.90E+13    0.0      3540.0
12. O+C2H4<=>CH3+HCO                                  1.92E+07    1.8       220.0
13. O+C2H5<=>CH3+CH2O                                 1.32E+14    0.0         0.0
14. O+C2H6<=>OH+C2H5                                  8.98E+07    1.9      5690.0
15. O2+CO<=>O+CO2                                     2.50E+12    0.0     47800.0
16. O2+CH2O<=>HO2+HCO                                 1.00E+14    0.0     40000.0
17. H+O2+M<=>HO2+M                                    2.80E+18   -0.9         0.0
       O2                Enhanced by    0.000E+00
       H2O               Enhanced by    0.000E+00
       CO                Enhanced by    7.500E-01
       CO2               Enhanced by    1.500E+00
       C2H6              Enhanced by    1.500E+00
       N2                Enhanced by    0.000E+00
       AR                Enhanced by    0.000E+00
18. H+2O2<=>HO2+O2                                    3.00E+20   -1.7         0.0
19. H+O2+H2O<=>HO2+H2O                                9.38E+18   -0.8         0.0
20. H+O2+N2<=>HO2+N2                                  3.75E+20   -1.7         0.0
21. H+O2+AR<=>HO2+AR                                  7.00E+17   -0.8         0.0
22. H+O2<=>O+OH                                       8.30E+13    0.0     14413.0
23. 2H+M<=>H2+M                                       1.00E+18   -1.0         0.0
       H2                Enhanced by    0.000E+00
       H2O               Enhanced by    0.000E+00
       CH4               Enhanced by    2.000E+00
       CO2               Enhanced by    0.000E+00
       C2H6              Enhanced by    3.000E+00
       AR                Enhanced by    6.300E-01
24. 2H+H2<=>2H2                                       9.00E+16   -0.6         0.0
25. 2H+H2O<=>H2+H2O                                   6.00E+19   -1.3         0.0
26. 2H+CO2<=>H2+CO2                                   5.50E+20   -2.0         0.0
27. H+OH+M<=>H2O+M                                    2.20E+22   -2.0         0.0
       H2                Enhanced by    7.300E-01
       H2O               Enhanced by    3.650E+00
       CH4               Enhanced by    2.000E+00
       C2H6              Enhanced by    3.000E+00
       AR                Enhanced by    3.800E-01
28. H+HO2<=>O2+H2                                     2.80E+13    0.0      1068.0
29. H+HO2<=>2OH                                       1.34E+14    0.0       635.0
30. H+CH2(+M)<=>CH3(+M)                               2.50E+16   -0.8         0.0
    Low pressure limit:  0.32000E+28 -0.31400E+01  0.12300E+04
    TROE centering:      0.68000E+00  0.78000E+02  0.19950E+04  0.55900E+04
       H2                Enhanced by    2.000E+00
       H2O               Enhanced by    6.000E+00
       CH4               Enhanced by    2.000E+00
       CO                Enhanced by    1.500E+00
```

```
      CO2                Enhanced by    2.000E+00
      C2H6               Enhanced by    3.000E+00
      AR                 Enhanced by    7.000E-01
31. H+CH3(+M)<=>CH4(+M)                              1.27E+16   -0.6       383.0
    Low pressure limit:  0.24770E+34 -0.47600E+01  0.24400E+04
    TROE centering:      0.78300E+00  0.74000E+02  0.29410E+04  0.69640E+04
      H2                 Enhanced by    2.000E+00
      H2O                Enhanced by    6.000E+00
      CH4                Enhanced by    2.000E+00
      CO                 Enhanced by    1.500E+00
      CO2                Enhanced by    2.000E+00
      C2H6               Enhanced by    3.000E+00
      AR                 Enhanced by    7.000E-01
32. H+CH4<=>CH3+H2                                   6.60E+08    1.6     10840.0
33. H+HCO(+M)<=>CH2O(+M)                             1.09E+12    0.5      -260.0
    Low pressure limit:  0.13500E+25 -0.25700E+01  0.14250E+04
    TROE centering:      0.78240E+00  0.27100E+03  0.27550E+04  0.65700E+04
      H2                 Enhanced by    2.000E+00
      H2O                Enhanced by    6.000E+00
      CH4                Enhanced by    2.000E+00
      CO                 Enhanced by    1.500E+00
      CO2                Enhanced by    2.000E+00
      C2H6               Enhanced by    3.000E+00
      AR                 Enhanced by    7.000E-01
34. H+HCO<=>H2+CO                                    7.34E+13    0.0         0.0
35. H+CH2O(+M)<=>CH3O(+M)                            5.40E+11    0.5      2600.0
    Low pressure limit:  0.22000E+31 -0.48000E+01  0.55600E+04
    TROE centering:      0.75800E+00  0.94000E+02  0.15550E+04  0.42000E+04
      H2                 Enhanced by    2.000E+00
      H2O                Enhanced by    6.000E+00
      CH4                Enhanced by    2.000E+00
      CO                 Enhanced by    1.500E+00
      CO2                Enhanced by    2.000E+00
      C2H6               Enhanced by    3.000E+00
36. H+CH2O<=>HCO+H2                                  2.30E+10    1.1      3275.0
37. H+CH3O<=>OH+CH3                                  3.20E+13    0.0         0.0
38. H+C2H4(+M)<=>C2H5(+M)                            1.08E+12    0.5      1820.0
    Low pressure limit:  0.12000E+43 -0.76200E+01  0.69700E+04
    TROE centering:      0.97530E+00  0.21000E+03  0.98400E+03  0.43740E+04
      H2                 Enhanced by    2.000E+00
      H2O                Enhanced by    6.000E+00
      CH4                Enhanced by    2.000E+00
      CO                 Enhanced by    1.500E+00
      CO2                Enhanced by    2.000E+00
      C2H6               Enhanced by    3.000E+00
      AR                 Enhanced by    7.000E-01
39. H+C2H5(+M)<=>C2H6(+M)                            5.21E+17   -1.0      1580.0
    Low pressure limit:  0.19900E+42 -0.70800E+01  0.66850E+04
    TROE centering:      0.84220E+00  0.12500E+03  0.22190E+04  0.68820E+04
      H2                 Enhanced by    2.000E+00
      H2O                Enhanced by    6.000E+00
      CH4                Enhanced by    2.000E+00
      CO                 Enhanced by    1.500E+00
      CO2                Enhanced by    2.000E+00
      C2H6               Enhanced by    3.000E+00
      AR                 Enhanced by    7.000E-01
```

```
 40. H+C2H6<=>C2H5+H2                                  1.15E+08    1.9      7530.0
 41. H2+CO(+M)<=>CH2O(+M)                              4.30E+07    1.5     79600.0
     Low pressure limit:  0.50700E+28 -0.34200E+01  0.84350E+05
     TROE centering:      0.93200E+00  0.19700E+03  0.15400E+04  0.10300E+05
        H2                Enhanced by    2.000E+00
        H2O               Enhanced by    6.000E+00
        CH4               Enhanced by    2.000E+00
        CO                Enhanced by    1.500E+00
        CO2               Enhanced by    2.000E+00
        C2H6              Enhanced by    3.000E+00
        AR                Enhanced by    7.000E-01
 42. OH+H2<=>H+H2O                                     2.16E+08    1.5      3430.0
 43. 2OH<=>O+H2O                                       3.57E+04    2.4     -2110.0
 44. OH+HO2<=>O2+H2O                                   2.90E+13    0.0      -500.0
 45. OH+CH2<=>H+CH2O                                   2.00E+13    0.0         0.0
 46. OH+CH2(S)<=>H+CH2O                                3.00E+13    0.0         0.0
 47. OH+CH3<=>CH2+H2O                                  5.60E+07    1.6      5420.0
 48. OH+CH3<=>CH2(S)+H2O                               2.50E+13    0.0         0.0
 49. OH+CH4<=>CH3+H2O                                  1.00E+08    1.6      3120.0
 50. OH+CO<=>H+CO2                                     4.76E+07    1.2        70.0
 51. OH+HCO<=>H2O+CO                                   5.00E+13    0.0         0.0
 52. OH+CH2O<=>HCO+H2O                                 3.43E+09    1.2      -447.0
 53. OH+C2H6<=>C2H5+H2O                                3.54E+06    2.1       870.0
 54. HO2+CH2<=>OH+CH2O                                 2.00E+13    0.0         0.0
 55. HO2+CH3<=>O2+CH4                                  1.00E+12    0.0         0.0
 56. HO2+CH3<=>OH+CH3O                                 2.00E+13    0.0         0.0
 57. HO2+CO<=>OH+CO2                                   1.50E+14    0.0     23600.0
 58. CH2+O2<=>OH+HCO                                   1.32E+13    0.0      1500.0
 59. CH2+H2<=>H+CH3                                    5.00E+05    2.0      7230.0
 60. CH2+CH3<=>H+C2H4                                  4.00E+13    0.0         0.0
 61. CH2+CH4<=>2CH3                                    2.46E+06    2.0      8270.0
 62. CH2(S)+N2<=>CH2+N2                                1.50E+13    0.0       600.0
 63. CH2(S)+AR<=>CH2+AR                                9.00E+12    0.0       600.0
 64. CH2(S)+O2<=>H+OH+CO                               2.80E+13    0.0         0.0
 65. CH2(S)+O2<=>CO+H2O                                1.20E+13    0.0         0.0
 66. CH2(S)+H2<=>CH3+H                                 7.00E+13    0.0         0.0
 67. CH2(S)+H2O<=>CH2+H2O                              3.00E+13    0.0         0.0
 68. CH2(S)+CH3<=>H+C2H4                               1.20E+13    0.0      -570.0
 69. CH2(S)+CH4<=>2CH3                                 1.60E+13    0.0      -570.0
 70. CH2(S)+CO<=>CH2+CO                                9.00E+12    0.0         0.0
 71. CH2(S)+CO2<=>CH2+CO2                              7.00E+12    0.0         0.0
 72. CH2(S)+CO2<=>CO+CH2O                              1.40E+13    0.0         0.0
 73. CH3+O2<=>O+CH3O                                   2.68E+13    0.0     28800.0
 74. CH3+O2<=>OH+CH2O                                  3.60E+10    0.0      8940.0
 75. 2CH3(+M)<=>C2H6(+M)                               2.12E+16   -1.0       620.0
     Low pressure limit:  0.17700E+51 -0.96700E+01  0.62200E+04
     TROE centering:      0.53250E+00  0.15100E+03  0.10380E+04  0.49700E+04
        H2                Enhanced by    2.000E+00
        H2O               Enhanced by    6.000E+00
        CH4               Enhanced by    2.000E+00
        CO                Enhanced by    1.500E+00
        CO2               Enhanced by    2.000E+00
        C2H6              Enhanced by    3.000E+00
        AR                Enhanced by    7.000E-01
 76. 2CH3<=>H+C2H5                                     4.99E+12    0.1     10600.0
 77. CH3+HCO<=>CH4+CO                                  2.65E+13    0.0         0.0
```

78. CH3+CH2O<=>HCO+CH4			3.32E+03	2.8	5860.0
79. CH3+C2H6<=>C2H5+CH4			6.14E+06	1.7	10450.0
80. HCO+H2O<=>H+CO+H2O			2.24E+18	-1.0	17000.0
81. HCO+M<=>H+CO+M			1.87E+17	-1.0	17000.0
H2	Enhanced by	2.000E+00			
H2O	Enhanced by	0.000E+00			
CH4	Enhanced by	2.000E+00			
CO	Enhanced by	1.500E+00			
CO2	Enhanced by	2.000E+00			
C2H6	Enhanced by	3.000E+00			
82. HCO+O2<=>HO2+CO			7.60E+12	0.0	400.0
83. CH3O+O2<=>HO2+CH2O			4.28E-13	7.6	-3530.0
84. C2H5+O2<=>HO2+C2H4			8.40E+11	0.0	3875.0

NOTE: A units mole-cm-sec-K, E units cal/mole

DETAILED MECHANISM WITH NITROGEN CHEMISTRY

GRI-Mech 2.11

Developed by Bowman, C.T., Hanson, R.K., Davidson, D.F., Gardiner, Jr., W.C., Lissianski, V., Smith, G.P., Golden, D.M., Frenklach, M. and Goldenberg, M. (1995)

Mechanism available from http://www.me.berkeley.edu/gri_mech/

49 species, 279 reactions

```
ELEMENTS   O  H  C  N  AR
SPECIES
H2       H        O        O2       OH       H2O      HO2      H2O2
C        CH       CH2      CH2(S)   CH3      CH4      CO       CO2
HCO      CH2O     CH2OH    CH3O     CH3OH    C2H      C2H2     C2H3
C2H4     C2H5     C2H6     HCCO     CH2CO    HCCOH    N        NH
NH2      NH3      NNH      NO       NO2      N2O      HNO      CN
HCN      H2CN     HCNN     HCNO     HOCN     HNCO     NCO      N2
AR
```

	REACTIONS CONSIDERED			(k = A T**b exp(-E/RT)) A	b	E
1.	2O+M<=>O2+M			1.20E+17	-1.0	0.0
	H2	Enhanced by	2.400E+00			
	H2O	Enhanced by	1.540E+01			
	CH4	Enhanced by	2.000E+00			
	CO	Enhanced by	1.750E+00			
	CO2	Enhanced by	3.600E+00			
	C2H6	Enhanced by	3.000E+00			
	AR	Enhanced by	8.300E-01			
2.	O+H+M<=>OH+M			5.00E+17	-1.0	0.0
	H2	Enhanced by	2.000E+00			
	H2O	Enhanced by	6.000E+00			
	CH4	Enhanced by	2.000E+00			
	CO	Enhanced by	1.500E+00			
	CO2	Enhanced by	2.000E+00			
	C2H6	Enhanced by	3.000E+00			
	AR	Enhanced by	7.000E-01			
3.	O+H2<=>H+OH			5.00E+04	2.7	6290.0
4.	O+HO2<=>OH+O2			2.00E+13	0.0	0.0
5.	O+H2O2<=>OH+HO2			9.63E+06	2.0	4000.0
6.	O+CH<=>H+CO			5.70E+13	0.0	0.0
7.	O+CH2<=>H+HCO			8.00E+13	0.0	0.0
8.	O+CH2(S)<=>H2+CO			1.50E+13	0.0	0.0
9.	O+CH2(S)<=>H+HCO			1.50E+13	0.0	0.0
10.	O+CH3<=>H+CH2O			8.43E+13	0.0	0.0
11.	O+CH4<=>OH+CH3			1.02E+09	1.5	8600.0
12.	O+CO+M<=>CO2+M			6.02E+14	0.0	3000.0

	H2	Enhanced by	2.000E+00			
	O2	Enhanced by	6.000E+00			
	H2O	Enhanced by	6.000E+00			
	CH4	Enhanced by	2.000E+00			
	CO	Enhanced by	1.500E+00			
	CO2	Enhanced by	3.500E+00			
	C2H6	Enhanced by	3.000E+00			
	AR	Enhanced by	5.000E-01			
13.	O+HCO<=>OH+CO			3.00E+13	0.0	0.0
14.	O+HCO<=>H+CO2			3.00E+13	0.0	0.0
15.	O+CH2O<=>OH+HCO			3.90E+13	0.0	3540.0
16.	O+CH2OH<=>OH+CH2O			1.00E+13	0.0	0.0
17.	O+CH3O<=>OH+CH2O			1.00E+13	0.0	0.0
18.	O+CH3OH<=>OH+CH2OH			3.88E+05	2.5	3100.0
19.	O+CH3OH<=>OH+CH3O			1.30E+05	2.5	5000.0
20.	O+C2H<=>CH+CO			5.00E+13	0.0	0.0
21.	O+C2H2<=>H+HCCO			1.02E+07	2.0	1900.0
22.	O+C2H2<=>OH+C2H			4.60E+19	-1.4	28950.0
23.	O+C2H2<=>CO+CH2			1.02E+07	2.0	1900.0
24.	O+C2H3<=>H+CH2CO			3.00E+13	0.0	0.0
25.	O+C2H4<=>CH3+HCO			1.92E+07	1.8	220.0
26.	O+C2H5<=>CH3+CH2O			1.32E+14	0.0	0.0
27.	O+C2H6<=>OH+C2H5			8.98E+07	1.9	5690.0
28.	O+HCCO<=>H+2CO			1.00E+14	0.0	0.0
29.	O+CH2CO<=>OH+HCCO			1.00E+13	0.0	8000.0
30.	O+CH2CO<=>CH2+CO2			1.75E+12	0.0	1350.0
31.	O2+CO<=>O+CO2			2.50E+12	0.0	47800.0
32.	O2+CH2O<=>HO2+HCO			1.00E+14	0.0	40000.0
33.	H+O2+M<=>HO2+M			2.80E+18	-0.9	0.0
	O2	Enhanced by	0.000E+00			
	H2O	Enhanced by	0.000E+00			
	CO	Enhanced by	7.500E-01			
	CO2	Enhanced by	1.500E+00			
	C2H6	Enhanced by	1.500E+00			
	N2	Enhanced by	0.000E+00			
	AR	Enhanced by	0.000E+00			
34.	H+2O2<=>HO2+O2			3.00E+20	-1.7	0.0
35.	H+O2+H2O<=>HO2+H2O			9.38E+18	-0.8	0.0
36.	H+O2+N2<=>HO2+N2			3.75E+20	-1.7	0.0
37.	H+O2+AR<=>HO2+AR			7.00E+17	-0.8	0.0
38.	H+O2<=>O+OH			8.30E+13	0.0	14413.0
39.	2H+M<=>H2+M			1.00E+18	-1.0	0.0
	H2	Enhanced by	0.000E+00			
	H2O	Enhanced by	0.000E+00			
	CH4	Enhanced by	2.000E+00			
	CO2	Enhanced by	0.000E+00			
	C2H6	Enhanced by	3.000E+00			
	AR	Enhanced by	6.300E-01			
40.	2H+H2<=>2H2			9.00E+16	-0.6	0.0
41.	2H+H2O<=>H2+H2O			6.00E+19	-1.3	0.0
42.	2H+CO2<=>H2+CO2			5.50E+20	-2.0	0.0
43.	H+OH+M<=>H2O+M			2.20E+22	-2.0	0.0
	H2	Enhanced by	7.300E-01			
	H2O	Enhanced by	3.650E+00			
	CH4	Enhanced by	2.000E+00			
	C2H6	Enhanced by	3.000E+00			

```
      AR                Enhanced by    3.800E-01
44. H+HO2<=>O+H2O                                  3.97E+12    0.0       671.0
45. H+HO2<=>O2+H2                                  2.80E+13    0.0      1068.0
46. H+HO2<=>2OH                                    1.34E+14    0.0       635.0
47. H+H2O2<=>HO2+H2                                1.21E+07    2.0      5200.0
48. H+H2O2<=>OH+H2O                                1.00E+13    0.0      3600.0
49. H+CH<=>C+H2                                    1.10E+14    0.0         0.0
50. H+CH2(+M)<=>CH3(+M)                            2.50E+16   -0.8         0.0
    Low pressure limit:  0.32000E+28 -0.31400E+01  0.12300E+04
    TROE centering:      0.68000E+00  0.78000E+02  0.19950E+04  0.55900E+04
      H2                Enhanced by    2.000E+00
      H2O               Enhanced by    6.000E+00
      CH4               Enhanced by    2.000E+00
      CO                Enhanced by    1.500E+00
      CO2               Enhanced by    2.000E+00
      C2H6              Enhanced by    3.000E+00
      AR                Enhanced by    7.000E-01
51. H+CH2(S)<=>CH+H2                               3.00E+13    0.0         0.0
52. H+CH3(+M)<=>CH4(+M)                            1.27E+16   -0.6       383.0
    Low pressure limit:  0.24770E+34 -0.47600E+01  0.24400E+04
    TROE centering:      0.78300E+00  0.74000E+02  0.29410E+04  0.69640E+04
      H2                Enhanced by    2.000E+00
      H2O               Enhanced by    6.000E+00
      CH4               Enhanced by    2.000E+00
      CO                Enhanced by    1.500E+00
      CO2               Enhanced by    2.000E+00
      C2H6              Enhanced by    3.000E+00
      AR                Enhanced by    7.000E-01
53. H+CH4<=>CH3+H2                                 6.60E+08    1.6     10840.0
54. H+HCO(+M)<=>CH2O(+M)                           1.09E+12    0.5      -260.0
    Low pressure limit:  0.13500E+25 -0.25700E+01  0.14250E+04
    TROE centering:      0.78240E+00  0.27100E+03  0.27550E+04  0.65700E+04
      H2                Enhanced by    2.000E+00
      H2O               Enhanced by    6.000E+00
      CH4               Enhanced by    2.000E+00
      CO                Enhanced by    1.500E+00
      CO2               Enhanced by    2.000E+00
      C2H6              Enhanced by    3.000E+00
      AR                Enhanced by    7.000E-01
55. H+HCO<=>H2+CO                                  7.34E+13    0.0         0.0
56. H+CH2O(+M)<=>CH2OH(+M)                         5.40E+11    0.5      3600.0
    Low pressure limit:  0.12700E+33 -0.48200E+01  0.65300E+04
    TROE centering:      0.71870E+00  0.10300E+03  0.12910E+04  0.41600E+04
      H2                Enhanced by    2.000E+00
      H2O               Enhanced by    6.000E+00
      CH4               Enhanced by    2.000E+00
      CO                Enhanced by    1.500E+00
      CO2               Enhanced by    2.000E+00
      C2H6              Enhanced by    3.000E+00
57. H+CH2O(+M)<=>CH3O(+M)                          5.40E+11    0.5      2600.0
    Low pressure limit:  0.22000E+31 -0.48000E+01  0.55600E+04
    TROE centering:      0.75800E+00  0.94000E+02  0.15550E+04  0.42000E+04
      H2                Enhanced by    2.000E+00
      H2O               Enhanced by    6.000E+00
      CH4               Enhanced by    2.000E+00
      CO                Enhanced by    1.500E+00
```

```
      CO2              Enhanced by    2.000E+00
      C2H6             Enhanced by    3.000E+00
58. H+CH2O<=>HCO+H2                                 2.30E+10    1.1      3275.0
59. H+CH2OH(+M)<=>CH3OH(+M)                         1.80E+13    0.0         0.0
    Low pressure limit:  0.30000E+32 -0.48000E+01  0.33000E+04
    TROE centering:      0.76790E+00  0.33800E+03  0.18120E+04  0.50810E+04
      H2               Enhanced by    2.000E+00
      H2O              Enhanced by    6.000E+00
      CH4              Enhanced by    2.000E+00
      CO               Enhanced by    1.500E+00
      CO2              Enhanced by    2.000E+00
      C2H6             Enhanced by    3.000E+00
60. H+CH2OH<=>H2+CH2O                               2.00E+13    0.0         0.0
61. H+CH2OH<=>OH+CH3                                1.20E+13    0.0         0.0
62. H+CH2OH<=>CH2(S)+H2O                            6.00E+12    0.0         0.0
63. H+CH3O(+M)<=>CH3OH(+M)                          5.00E+13    0.0         0.0
    Low pressure limit:  0.86000E+29 -0.40000E+01  0.30250E+04
    TROE centering:      0.89020E+00  0.14400E+03  0.28380E+04  0.45569E+05
      H2               Enhanced by    2.000E+00
      H2O              Enhanced by    6.000E+00
      CH4              Enhanced by    2.000E+00
      CO               Enhanced by    1.500E+00
      CO2              Enhanced by    2.000E+00
      C2H6             Enhanced by    3.000E+00
64. H+CH3O<=>H+CH2OH                                3.40E+06    1.6         0.0
65. H+CH3O<=>H2+CH2O                                2.00E+13    0.0         0.0
66. H+CH3O<=>OH+CH3                                 3.20E+13    0.0         0.0
67. H+CH3O<=>CH2(S)+H2O                             1.60E+13    0.0         0.0
68. H+CH3OH<=>CH2OH+H2                              1.70E+07    2.1      4870.0
69. H+CH3OH<=>CH3O+H2                               4.20E+06    2.1      4870.0
70. H+C2H(+M)<=>C2H2(+M)                            1.00E+17   -1.0         0.0
    Low pressure limit:  0.37500E+34 -0.48000E+01  0.19000E+04
    TROE centering:      0.64640E+00  0.13200E+03  0.13150E+04  0.55660E+04
      H2               Enhanced by    2.000E+00
      H2O              Enhanced by    6.000E+00
      CH4              Enhanced by    2.000E+00
      CO               Enhanced by    1.500E+00
      CO2              Enhanced by    2.000E+00
      C2H6             Enhanced by    3.000E+00
      AR               Enhanced by    7.000E-01
71. H+C2H2(+M)<=>C2H3(+M)                           5.60E+12    0.0      2400.0
    Low pressure limit:  0.38000E+41 -0.72700E+01  0.72200E+04
    TROE centering:      0.75070E+00  0.98500E+02  0.13020E+04  0.41670E+04
      H2               Enhanced by    2.000E+00
      H2O              Enhanced by    6.000E+00
      CH4              Enhanced by    2.000E+00
      CO               Enhanced by    1.500E+00
      CO2              Enhanced by    2.000E+00
      C2H6             Enhanced by    3.000E+00
      AR               Enhanced by    7.000E-01
72. H+C2H3(+M)<=>C2H4(+M)                           6.08E+12    0.3       280.0
    Low pressure limit:  0.14000E+31 -0.38600E+01  0.33200E+04
    TROE centering:      0.78200E+00  0.20750E+03  0.26630E+04  0.60950E+04
      H2               Enhanced by    2.000E+00
      H2O              Enhanced by    6.000E+00
      CH4              Enhanced by    2.000E+00
```

```
        CO                Enhanced by    1.500E+00
        CO2               Enhanced by    2.000E+00
        C2H6              Enhanced by    3.000E+00
        AR                Enhanced by    7.000E-01
 73. H+C2H3<=>H2+C2H2                                 3.00E+13    0.0         0.0
 74. H+C2H4(+M)<=>C2H5(+M)                            1.08E+12    0.5      1820.0
     Low pressure limit:  0.12000E+43 -0.76200E+01  0.69700E+04
     TROE centering:      0.97530E+00  0.21000E+03  0.98400E+03  0.43740E+04
        H2                Enhanced by    2.000E+00
        H2O               Enhanced by    6.000E+00
        CH4               Enhanced by    2.000E+00
        CO                Enhanced by    1.500E+00
        CO2               Enhanced by    2.000E+00
        C2H6              Enhanced by    3.000E+00
        AR                Enhanced by    7.000E-01
 75. H+C2H4<=>C2H3+H2                                 1.33E+06    2.5     12240.0
 76. H+C2H5(+M)<=>C2H6(+M)                            5.21E+17   -1.0      1580.0
     Low pressure limit:  0.19900E+42 -0.70800E+01  0.66850E+04
     TROE centering:      0.84220E+00  0.12500E+03  0.22190E+04  0.68820E+04
        H2                Enhanced by    2.000E+00
        H2O               Enhanced by    6.000E+00
        CH4               Enhanced by    2.000E+00
        CO                Enhanced by    1.500E+00
        CO2               Enhanced by    2.000E+00
        C2H6              Enhanced by    3.000E+00
        AR                Enhanced by    7.000E-01
 77. H+C2H5<=>H2+C2H4                                 2.00E+12    0.0         0.0
 78. H+C2H6<=>C2H5+H2                                 1.15E+08    1.9      7530.0
 79. H+HCCO<=>CH2(S)+CO                               1.00E+14    0.0         0.0
 80. H+CH2CO<=>HCCO+H2                                5.00E+13    0.0      8000.0
 81. H+CH2CO<=>CH3+CO                                 1.13E+13    0.0      3428.0
 82. H+HCCOH<=>H+CH2CO                                1.00E+13    0.0         0.0
 83. H2+CO(+M)<=>CH2O(+M)                             4.30E+07    1.5     79600.0
     Low pressure limit:  0.50700E+28 -0.34200E+01  0.84350E+05
     TROE centering:      0.93200E+00  0.19700E+03  0.15400E+04  0.10300E+05
        H2                Enhanced by    2.000E+00
        H2O               Enhanced by    6.000E+00
        CH4               Enhanced by    2.000E+00
        CO                Enhanced by    1.500E+00
        CO2               Enhanced by    2.000E+00
        C2H6              Enhanced by    3.000E+00
        AR                Enhanced by    7.000E-01
 84. OH+H2<=>H+H2O                                    2.16E+08    1.5      3430.0
 85. 2OH(+M)<=>H2O2(+M)                               7.40E+13   -0.4         0.0
     Low pressure limit:  0.23000E+19 -0.90000E+00 -0.17000E+04
     TROE centering:      0.73460E+00  0.94000E+02  0.17560E+04  0.51820E+04
        H2                Enhanced by    2.000E+00
        H2O               Enhanced by    6.000E+00
        CH4               Enhanced by    2.000E+00
        CO                Enhanced by    1.500E+00
        CO2               Enhanced by    2.000E+00
        C2H6              Enhanced by    3.000E+00
        AR                Enhanced by    7.000E-01
 86. 2OH<=>O+H2O                                      3.57E+04    2.4     -2110.0
 87. OH+HO2<=>O2+H2O                                  2.90E+13    0.0      -500.0
 88. OH+H2O2<=>HO2+H2O                                1.75E+12    0.0       320.0
```

```
     Declared duplicate reaction...
 89. OH+H2O2<=>HO2+H2O                                 5.80E+14    0.0      9560.0
     Declared duplicate reaction...
 90. OH+C<=>H+CO                                       5.00E+13    0.0         0.0
 91. OH+CH<=>H+HCO                                     3.00E+13    0.0         0.0
 92. OH+CH2<=>H+CH2O                                   2.00E+13    0.0         0.0
 93. OH+CH2<=>CH+H2O                                   1.13E+07    2.0      3000.0
 94. OH+CH2(S)<=>H+CH2O                                3.00E+13    0.0         0.0
 95. OH+CH3(+M)<=>CH3OH(+M)                            6.30E+13    0.0         0.0
     Low pressure limit:  0.27000E+39 -0.63000E+01  0.31000E+04
     TROE centering:      0.21050E+00  0.83500E+02  0.53980E+04  0.83700E+04
        H2               Enhanced by    2.000E+00
        H2O              Enhanced by    6.000E+00
        CH4              Enhanced by    2.000E+00
        CO               Enhanced by    1.500E+00
        CO2              Enhanced by    2.000E+00
        C2H6             Enhanced by    3.000E+00
 96. OH+CH3<=>CH2+H2O                                  5.60E+07    1.6      5420.0
 97. OH+CH3<=>CH2(S)+H2O                               2.50E+13    0.0         0.0
 98. OH+CH4<=>CH3+H2O                                  1.00E+08    1.6      3120.0
 99. OH+CO<=>H+CO2                                     4.76E+07    1.2        70.0
100. OH+HCO<=>H2O+CO                                   5.00E+13    0.0         0.0
101. OH+CH2O<=>HCO+H2O                                 3.43E+09    1.2      -447.0
102. OH+CH2OH<=>H2O+CH2O                               5.00E+12    0.0         0.0
103. OH+CH3O<=>H2O+CH2O                                5.00E+12    0.0         0.0
104. OH+CH3OH<=>CH2OH+H2O                              1.44E+06    2.0      -840.0
105. OH+CH3OH<=>CH3O+H2O                               6.30E+06    2.0      1500.0
106. OH+C2H<=>H+HCCO                                   2.00E+13    0.0         0.0
107. OH+C2H2<=>H+CH2CO                                 2.18E-04    4.5     -1000.0
108. OH+C2H2<=>H+HCCOH                                 5.04E+05    2.3     13500.0
109. OH+C2H2<=>C2H+H2O                                 3.37E+07    2.0     14000.0
110. OH+C2H2<=>CH3+CO                                  4.83E-04    4.0     -2000.0
111. OH+C2H3<=>H2O+C2H2                                5.00E+12    0.0         0.0
112. OH+C2H4<=>C2H3+H2O                                3.60E+06    2.0      2500.0
113. OH+C2H6<=>C2H5+H2O                                3.54E+06    2.1       870.0
114. OH+CH2CO<=>HCCO+H2O                               7.50E+12    0.0      2000.0
115. 2HO2<=>O2+H2O2                                    1.30E+11    0.0     -1630.0
     Declared duplicate reaction...
116. 2HO2<=>O2+H2O2                                    4.20E+14    0.0     12000.0
     Declared duplicate reaction...
117. HO2+CH2<=>OH+CH2O                                 2.00E+13    0.0         0.0
118. HO2+CH3<=>O2+CH4                                  1.00E+12    0.0         0.0
119. HO2+CH3<=>OH+CH3O                                 2.00E+13    0.0         0.0
120. HO2+CO<=>OH+CO2                                   1.50E+14    0.0     23600.0
121. HO2+CH2O<=>HCO+H2O2                               1.00E+12    0.0      8000.0
122. C+O2<=>O+CO                                       5.80E+13    0.0       576.0
123. C+CH2<=>H+C2H                                     5.00E+13    0.0         0.0
124. C+CH3<=>H+C2H2                                    5.00E+13    0.0         0.0
125. CH+O2<=>O+HCO                                     3.30E+13    0.0         0.0
126. CH+H2<=>H+CH2                                     1.11E+08    1.8      1670.0
127. CH+H2O<=>H+CH2O                                   1.71E+13    0.0      -755.0
128. CH+CH2<=>H+C2H2                                   4.00E+13    0.0         0.0
129. CH+CH3<=>H+C2H3                                   3.00E+13    0.0         0.0
130. CH+CH4<=>H+C2H4                                   6.00E+13    0.0         0.0
131. CH+CO(+M)<=>HCCO(+M)                              5.00E+13    0.0         0.0
     Low pressure limit:  0.26900E+29 -0.37400E+01  0.19360E+04
```

```
      TROE centering:      0.57570E+00  0.23700E+03  0.16520E+04  0.50690E+04
         H2               Enhanced by    2.000E+00
         H2O              Enhanced by    6.000E+00
         CH4              Enhanced by    2.000E+00
         CO               Enhanced by    1.500E+00
         CO2              Enhanced by    2.000E+00
         C2H6             Enhanced by    3.000E+00
         AR               Enhanced by    7.000E-01
 132. CH+CO2<=>HCO+CO                                3.40E+12    0.0       690.0
 133. CH+CH2O<=>H+CH2CO                              9.46E+13    0.0      -515.0
 134. CH+HCCO<=>CO+C2H2                              5.00E+13    0.0         0.0
 135. CH2+O2<=>OH+HCO                                1.32E+13    0.0      1500.0
 136. CH2+H2<=>H+CH3                                 5.00E+05    2.0      7230.0
 137. 2CH2<=>H2+C2H2                                 3.20E+13    0.0         0.0
 138. CH2+CH3<=>H+C2H4                               4.00E+13    0.0         0.0
 139. CH2+CH4<=>2CH3                                 2.46E+06    2.0      8270.0
 140. CH2+CO(+M)<=>CH2CO(+M)                         8.10E+11    0.5      4510.0
      Low pressure limit:  0.26900E+34 -0.51100E+01  0.70950E+04
      TROE centering:      0.59070E+00  0.27500E+03  0.12260E+04  0.51850E+04
         H2               Enhanced by    2.000E+00
         H2O              Enhanced by    6.000E+00
         CH4              Enhanced by    2.000E+00
         CO               Enhanced by    1.500E+00
         CO2              Enhanced by    2.000E+00
         C2H6             Enhanced by    3.000E+00
         AR               Enhanced by    7.000E-01
 141. CH2+HCCO<=>C2H3+CO                             3.00E+13    0.0         0.0
 142. CH2(S)+N2<=>CH2+N2                             1.50E+13    0.0       600.0
 143. CH2(S)+AR<=>CH2+AR                             9.00E+12    0.0       600.0
 144. CH2(S)+O2<=>H+OH+CO                            2.80E+13    0.0         0.0
 145. CH2(S)+O2<=>CO+H2O                             1.20E+13    0.0         0.0
 146. CH2(S)+H2<=>CH3+H                              7.00E+13    0.0         0.0
 147. CH2(S)+H2O(+M)<=>CH3OH(+M)                     2.00E+13    0.0         0.0
      Low pressure limit:  0.27000E+39 -0.63000E+01  0.31000E+04
      TROE centering:      0.15070E+00  0.13400E+03  0.23830E+04  0.72650E+04
         H2               Enhanced by    2.000E+00
         H2O              Enhanced by    6.000E+00
         CH4              Enhanced by    2.000E+00
         CO               Enhanced by    1.500E+00
         CO2              Enhanced by    2.000E+00
         C2H6             Enhanced by    3.000E+00
 148. CH2(S)+H2O<=>CH2+H2O                           3.00E+13    0.0         0.0
 149. CH2(S)+CH3<=>H+C2H4                            1.20E+13    0.0      -570.0
 150. CH2(S)+CH4<=>2CH3                              1.60E+13    0.0      -570.0
 151. CH2(S)+CO<=>CH2+CO                             9.00E+12    0.0         0.0
 152. CH2(S)+CO2<=>CH2+CO2                           7.00E+12    0.0         0.0
 153. CH2(S)+CO2<=>CO+CH2O                           1.40E+13    0.0         0.0
 154. CH2(S)+C2H6<=>CH3+C2H5                         4.00E+13    0.0      -550.0
 155. CH3+O2<=>O+CH3O                                2.68E+13    0.0     28800.0
 156. CH3+O2<=>OH+CH2O                               3.60E+10    0.0      8940.0
 157. CH3+H2O2<=>HO2+CH4                             2.45E+04    2.5      5180.0
 158. 2CH3(+M)<=>C2H6(+M)                            2.12E+16   -1.0       620.0
      Low pressure limit:  0.17700E+51 -0.96700E+01  0.62200E+04
      TROE centering:      0.53250E+00  0.15100E+03  0.10380E+04  0.49700E+04
         H2               Enhanced by    2.000E+00
         H2O              Enhanced by    6.000E+00
```

```
        CH4                Enhanced by    2.000E+00
        CO                 Enhanced by    1.500E+00
        CO2                Enhanced by    2.000E+00
        C2H6               Enhanced by    3.000E+00
        AR                 Enhanced by    7.000E-01
159. 2CH3<=>H+C2H5                                    4.99E+12    0.1    10600.0
160. CH3+HCO<=>CH4+CO                                 2.65E+13    0.0        0.0
161. CH3+CH2O<=>HCO+CH4                               3.32E+03    2.8     5860.0
162. CH3+CH3OH<=>CH2OH+CH4                            3.00E+07    1.5     9940.0
163. CH3+CH3OH<=>CH3O+CH4                             1.00E+07    1.5     9940.0
164. CH3+C2H4<=>C2H3+CH4                              2.27E+05    2.0     9200.0
165. CH3+C2H6<=>C2H5+CH4                              6.14E+06    1.7    10450.0
166. HCO+H2O<=>H+CO+H2O                               2.24E+18   -1.0    17000.0
167. HCO+M<=>H+CO+M                                   1.87E+17   -1.0    17000.0
        H2                 Enhanced by    2.000E+00
        H2O                Enhanced by    0.000E+00
        CH4                Enhanced by    2.000E+00
        CO                 Enhanced by    1.500E+00
        CO2                Enhanced by    2.000E+00
        C2H6               Enhanced by    3.000E+00
168. HCO+O2<=>HO2+CO                                  7.60E+12    0.0      400.0
169. CH2OH+O2<=>HO2+CH2O                              1.80E+13    0.0      900.0
170. CH3O+O2<=>HO2+CH2O                               4.28E-13    7.6    -3530.0
171. C2H+O2<=>HCO+CO                                  5.00E+13    0.0     1500.0
172. C2H+H2<=>H+C2H2                                  4.07E+05    2.4      200.0
173. C2H3+O2<=>HCO+CH2O                               3.98E+12    0.0     -240.0
174. C2H4(+M)<=>H2+C2H2(+M)                           8.00E+12    0.4    88770.0
     Low pressure limit:  0.70000E+51 -0.93100E+01  0.99860E+05
     TROE centering:      0.73450E+00  0.18000E+03  0.10350E+04  0.54170E+04
        H2                 Enhanced by    2.000E+00
        H2O                Enhanced by    6.000E+00
        CH4                Enhanced by    2.000E+00
        CO                 Enhanced by    1.500E+00
        CO2                Enhanced by    2.000E+00
        C2H6               Enhanced by    3.000E+00
        AR                 Enhanced by    7.000E-01
175. C2H5+O2<=>HO2+C2H4                               8.40E+11    0.0     3875.0
176. HCCO+O2<=>OH+2CO                                 1.60E+12    0.0      854.0
177. 2HCCO<=>2CO+C2H2                                 1.00E+13    0.0        0.0
178. N+NO<=>N2+O                                      3.50E+13    0.0      330.0
179. N+O2<=>NO+O                                      2.65E+12    0.0     6400.0
180. N+OH<=>NO+H                                      7.33E+13    0.0     1120.0
181. N2O+O<=>N2+O2                                    1.40E+12    0.0    10810.0
182. N2O+O<=>2NO                                      2.90E+13    0.0    23150.0
183. N2O+H<=>N2+OH                                    4.40E+14    0.0    18880.0
184. N2O+OH<=>N2+HO2                                  2.00E+12    0.0    21060.0
185. N2O(+M)<=>N2+O(+M)                               1.30E+11    0.0    59620.0
     Low pressure limit:  0.62000E+15  0.00000E+00  0.56100E+05
        H2                 Enhanced by    2.000E+00
        H2O                Enhanced by    6.000E+00
        CH4                Enhanced by    2.000E+00
        CO                 Enhanced by    1.500E+00
        CO2                Enhanced by    2.000E+00
        C2H6               Enhanced by    3.000E+00
        AR                 Enhanced by    7.000E-01
186. HO2+NO<=>NO2+OH                                  2.11E+12    0.0     -480.0
```

187.	NO+O+M<=>NO2+M			1.06E+20	-1.4	0.0
	H2	Enhanced by	2.000E+00			
	H2O	Enhanced by	6.000E+00			
	CH4	Enhanced by	2.000E+00			
	CO	Enhanced by	1.500E+00			
	CO2	Enhanced by	2.000E+00			
	C2H6	Enhanced by	3.000E+00			
	AR	Enhanced by	7.000E-01			
188.	NO2+O<=>NO+O2			3.90E+12	0.0	-240.0
189.	NO2+H<=>NO+OH			1.32E+14	0.0	360.0
190.	NH+O<=>NO+H			5.00E+13	0.0	0.0
191.	NH+H<=>N+H2			3.20E+13	0.0	330.0
192.	NH+OH<=>HNO+H			2.00E+13	0.0	0.0
193.	NH+OH<=>N+H2O			2.00E+09	1.2	0.0
194.	NH+O2<=>HNO+O			4.61E+05	2.0	6500.0
195.	NH+O2<=>NO+OH			1.28E+06	1.5	100.0
196.	NH+N<=>N2+H			1.50E+13	0.0	0.0
197.	NH+H2O<=>HNO+H2			2.00E+13	0.0	13850.0
198.	NH+NO<=>N2+OH			2.16E+13	-0.2	0.0
199.	NH+NO<=>N2O+H			4.16E+14	-0.5	0.0
200.	NH2+O<=>OH+NH			7.00E+12	0.0	0.0
201.	NH2+O<=>H+HNO			4.60E+13	0.0	0.0
202.	NH2+H<=>NH+H2			4.00E+13	0.0	3650.0
203.	NH2+OH<=>NH+H2O			9.00E+07	1.5	-460.0
204.	NNH<=>N2+H			3.30E+08	0.0	0.0
205.	NNH+M<=>N2+H+M			1.30E+14	-0.1	4980.0
	H2	Enhanced by	2.000E+00			
	H2O	Enhanced by	6.000E+00			
	CH4	Enhanced by	2.000E+00			
	CO	Enhanced by	1.500E+00			
	CO2	Enhanced by	2.000E+00			
	C2H6	Enhanced by	3.000E+00			
	AR	Enhanced by	7.000E-01			
206.	NNH+O2<=>HO2+N2			5.00E+12	0.0	0.0
207.	NNH+O<=>OH+N2			2.50E+13	0.0	0.0
208.	NNH+O<=>NH+NO			7.00E+13	0.0	0.0
209.	NNH+H<=>H2+N2			5.00E+13	0.0	0.0
210.	NNH+OH<=>H2O+N2			2.00E+13	0.0	0.0
211.	NNH+CH3<=>CH4+N2			2.50E+13	0.0	0.0
212.	H+NO+M<=>HNO+M			8.95E+19	-1.3	740.0
	H2	Enhanced by	2.000E+00			
	H2O	Enhanced by	6.000E+00			
	CH4	Enhanced by	2.000E+00			
	CO	Enhanced by	1.500E+00			
	CO2	Enhanced by	2.000E+00			
	C2H6	Enhanced by	3.000E+00			
	AR	Enhanced by	7.000E-01			
213.	HNO+O<=>NO+OH			2.50E+13	0.0	0.0
214.	HNO+H<=>H2+NO			4.50E+11	0.7	660.0
215.	HNO+OH<=>NO+H2O			1.30E+07	1.9	-950.0
216.	HNO+O2<=>HO2+NO			1.00E+13	0.0	13000.0
217.	CN+O<=>CO+N			7.70E+13	0.0	0.0
218.	CN+OH<=>NCO+H			4.00E+13	0.0	0.0
219.	CN+H2O<=>HCN+OH			8.00E+12	0.0	7460.0
220.	CN+O2<=>NCO+O			6.14E+12	0.0	-440.0
221.	CN+H2<=>HCN+H			2.10E+13	0.0	4710.0

222.	NCO+O<=>NO+CO			2.35E+13	0.0	0.0
223.	NCO+H<=>NH+CO			5.40E+13	0.0	0.0
224.	NCO+OH<=>NO+H+CO			2.50E+12	0.0	0.0
225.	NCO+N<=>N2+CO			2.00E+13	0.0	0.0
226.	NCO+O2<=>NO+CO2			2.00E+12	0.0	20000.0
227.	NCO+M<=>N+CO+M			8.80E+16	-0.5	48000.0
	H2	Enhanced by	2.000E+00			
	H2O	Enhanced by	6.000E+00			
	CH4	Enhanced by	2.000E+00			
	CO	Enhanced by	1.500E+00			
	CO2	Enhanced by	2.000E+00			
	C2H6	Enhanced by	3.000E+00			
	AR	Enhanced by	7.000E-01			
228.	NCO+NO<=>N2O+CO			2.85E+17	-1.5	740.0
229.	NCO+NO<=>N2+CO2			5.70E+18	-2.0	800.0
230.	HCN+M<=>H+CN+M			1.04E+29	-3.3	126600.0
	H2	Enhanced by	2.000E+00			
	H2O	Enhanced by	6.000E+00			
	CH4	Enhanced by	2.000E+00			
	CO	Enhanced by	1.500E+00			
	CO2	Enhanced by	2.000E+00			
	C2H6	Enhanced by	3.000E+00			
	AR	Enhanced by	7.000E-01			
231.	HCN+O<=>NCO+H			1.11E+04	2.6	4980.0
232.	HCN+O<=>NH+CO			2.77E+03	2.6	4980.0
233.	HCN+O<=>CN+OH			2.13E+09	1.6	26600.0
234.	HCN+OH<=>HOCN+H			1.10E+06	2.0	13370.0
235.	HCN+OH<=>HNCO+H			4.40E+03	2.3	6400.0
236.	HCN+OH<=>NH2+CO			1.60E+02	2.6	9000.0
237.	H+HCN+M<=>H2CN+M			1.40E+26	-3.4	1900.0
	H2	Enhanced by	2.000E+00			
	H2O	Enhanced by	6.000E+00			
	CH4	Enhanced by	2.000E+00			
	CO	Enhanced by	1.500E+00			
	CO2	Enhanced by	2.000E+00			
	C2H6	Enhanced by	3.000E+00			
	AR	Enhanced by	7.000E-01			
238.	H2CN+N<=>N2+CH2			6.00E+13	0.0	400.0
239.	C+N2<=>CN+N			6.30E+13	0.0	46020.0
240.	CH+N2<=>HCN+N			2.86E+08	1.1	20400.0
241.	CH+N2(+M)<=>HCNN(+M)			3.10E+12	0.1	0.0
	Low pressure limit:	0.13000E+26	-0.31600E+01	0.74000E+03		
	TROE centering:	0.66700E+00	0.23500E+03	0.21170E+04	0.45360E+04	
	H2	Enhanced by	2.000E+00			
	H2O	Enhanced by	6.000E+00			
	CH4	Enhanced by	2.000E+00			
	CO	Enhanced by	1.500E+00			
	CO2	Enhanced by	2.000E+00			
	C2H6	Enhanced by	3.000E+00			
	AR	Enhanced by	7.000E-01			
242.	CH2+N2<=>HCN+NH			1.00E+13	0.0	74000.0
243.	CH2(S)+N2<=>NH+HCN			1.00E+11	0.0	65000.0
244.	C+NO<=>CN+O			1.90E+13	0.0	0.0
245.	C+NO<=>CO+N			2.90E+13	0.0	0.0
246.	CH+NO<=>HCN+O			5.00E+13	0.0	0.0
247.	CH+NO<=>H+NCO			2.00E+13	0.0	0.0

248.	CH+NO<=>N+HCO			3.00E+13	0.0	0.0
249.	CH2+NO<=>H+HNCO			3.10E+17	-1.4	1270.0
250.	CH2+NO<=>OH+HCN			2.90E+14	-0.7	760.0
251.	CH2+NO<=>H+HCNO			3.80E+13	-0.4	580.0
252.	CH2(S)+NO<=>H+HNCO			3.10E+17	-1.4	1270.0
253.	CH2(S)+NO<=>OH+HCN			2.90E+14	-0.7	760.0
254.	CH2(S)+NO<=>H+HCNO			3.80E+13	-0.4	580.0
255.	CH3+NO<=>HCN+H2O			9.60E+13	0.0	28800.0
256.	CH3+NO<=>H2CN+OH			1.00E+12	0.0	21750.0
257.	HCNN+O<=>CO+H+N2			2.20E+13	0.0	0.0
258.	HCNN+O<=>HCN+NO			2.00E+12	0.0	0.0
259.	HCNN+O2<=>O+HCO+N2			1.20E+13	0.0	0.0
260.	HCNN+OH<=>H+HCO+N2			1.20E+13	0.0	0.0
261.	HCNN+H<=>CH2+N2			1.00E+14	0.0	0.0
262.	HNCO+O<=>NH+CO2			9.80E+07	1.4	8500.0
263.	HNCO+O<=>HNO+CO			1.50E+08	1.6	44000.0
264.	HNCO+O<=>NCO+OH			2.20E+06	2.1	11400.0
265.	HNCO+H<=>NH2+CO			2.25E+07	1.7	3800.0
266.	HNCO+H<=>H2+NCO			1.05E+05	2.5	13300.0
267.	HNCO+OH<=>NCO+H2O			4.65E+12	0.0	6850.0
268.	HNCO+OH<=>NH2+CO2			1.55E+12	0.0	6850.0
269.	HNCO+M<=>NH+CO+M			1.18E+16	0.0	84720.0
	H2	Enhanced by	2.000E+00			
	H2O	Enhanced by	6.000E+00			
	CH4	Enhanced by	2.000E+00			
	CO	Enhanced by	1.500E+00			
	CO2	Enhanced by	2.000E+00			
	C2H6	Enhanced by	3.000E+00			
	AR	Enhanced by	7.000E-01			
270.	HCNO+H<=>H+HNCO			2.10E+15	-0.7	2850.0
271.	HCNO+H<=>OH+HCN			2.70E+11	0.2	2120.0
272.	HCNO+H<=>NH2+CO			1.70E+14	-0.8	2890.0
273.	HOCN+H<=>H+HNCO			2.00E+07	2.0	2000.0
274.	HCCO+NO<=>HCNO+CO			2.35E+13	0.0	0.0
275.	CH3+N<=>H2CN+H			6.10E+14	-0.3	290.0
276.	CH3+N<=>HCN+H2			3.70E+12	0.1	-90.0
277.	NH3+H<=>NH2+H2			5.40E+05	2.4	-9915.0
278.	NH3+OH<=>NH2+H2O			5.00E+07	1.6	-955.0
279.	NH3+O<=>NH2+OH			9.40E+06	1.9	6460.0

NOTE: A units mole-cm-sec-K, E units cal/mole

This is the last page of the dissertation